MODE LOCKING IN THE RING LASER GYROSCOPE:

REDUCED THRESHOLD FOR TWO CAVITY MODES

A thesis submitted for the degree of Doctor of Philosophy

by

Mira Naftaly

Department of Physics, Brunel University

September 1990

Brunel University, Uxbridge
Department of Physics

Mira Naftaly

MODE LOCKING IN THE RING LASER GYROSCOPE:
REDUCED THRESHOLD FOR TWO CAVITY MODES

1989

ABSTRACT

A ring laser gyroscope is a device which employs a ring laser to measure rotation. A ring laser supports two beams propagating in opposite directions around the ring resonator. When the gyroscope is rotated, the frequencies of the two beams split by an amount proportional to the rate of rotation: the device works by measuring this frequency splitting.

The main problem of ring laser gyroscope design is the frequency synchronisation - lock-in - of the two beams at low rates of rotation. Lock-in arises from weak mutual coupling caused by backscattering at the mirrors and results in a dead band around zero.

One of the possible solutions to this problem is a two-mode ring laser in which two modes oscillate simultaneously and interact to reduce the dead band. The present work reviews the theory of lock-in and offers a theoretical basis for this approach, as well as providing experimental evidence to support it.

i

ACKNOWLEDGEMENTS

This thesis was produced on an Apple® Macintosh™ Plus 1Mb word processor with a Rodime™ 20Mb hard disk, using the following software: Claris™ MacWrite 5.0 for text; Expressionist™ for mathematical expressions; Passage™ D.4 for graphs and figures; MacDraft™ 1.2a for diagrams.

CONTENTS

LIST OF FIGURES

Chapter 1

INTRODUCTION

1. INTRODUCTION

Sagnac interferometer was first proposed as a possible optical inertial rotation sensor in 1913. At that time Sagnac effect was on threshold of experimental resolution and the interferometer could in no way compete with mechanical gyroscopes. With invention of lasers, however, it became clear that in an active resonator the effect could be easily and accurately measured, and that therefore a ring laser could become a novel type of gyroscope.

An early detailed study of the device was carried out by Aronowitz[4]; more recently, Chow *et al.*[9] reviewed the general field of inertial rotation sensors, both active and passive; lately, the state-of-the-art devices together with current theoretical understanding were comprehensively discussed by Wilkinson[31].

A ring laser gyroscope employs a ring laser to measure rotation. The laser universally used in gyroscopes is the 0.6328μm He-Ne laser; the most common resonator geometry is the three-mirror equilateral-triangle ring. A ring resonator supports two modes propagating in opposite directions. When the resonator is rotated the two modes acquire a relative frequency shift which is linearly proportional to the rate of rotation. The device works by heterodyning the two output beams and measuring their frequency difference.

The main problem of ring laser gyroscope design is the frequency synchronisation - "lock-in" - of the two modes at low rates of rotation. Lock-in arises from weak mutual coupling caused by backscattering at the mirrors, and results in a dead band around zero and a strongly nonlinear signal near threshold.

To overcome this problem, a biasing technique of back-and-forth rotation - "dithering" - has been adopted in many commercial systems, with great success:

2

rates of rotation down to 10^{-3}deg/hr have been mesured. Nonetheless, there are drawbacks: apart from the obvious one of necessitating mechanical oscillation of the gyroscope, the technique suffers from random noise induced by irregular bias and loss of information as the system passes through the dead band.

Several other methods of biasing have been explored as well. The most popular among these has been the four-mirror non-planar resonator with a Faraday mirror which gives rise to four modes widely separate in frequency[28]. This technique suffers from complexity and nonlinearities due to the many optical components in the system.

A completely different approach was adopted by Sanders *et al.*[21], Scully *et al.*[23] and Anderson *et al.*[2,3] This is based on adjusting the laser so as to induce two modes to oscillate simultaneously (i.e., two longitudinal modes or a longitudinal and a transverse one): the two modes, which must be approximately equal in intensity, then interact to reduce the lock-in threshold. The present work explores this technique in more detail.

Chapter 2 of the work is devoted to theoretical considerations: Ch.2.1 provides a brief description of the Sagnac interferometer; Ch.2.2 discusses Sagnac effect in ring lasers; Ch.2.3 reviews the relevant aspects of the 0.6328μm He-Ne laser; Ch.2.4, based on Lamb's theory, derives the lock-in equation for a one-mode ring laser; Ch.2.5 extends this to a two-mode case. Of the experimental chapters, Chapter 3 describes the system, and Chapter 4 presents the results, including a brief discussion of their significance.

It has been the aim of this work to investigate whether an optically biased no-moving-parts ring laser gyroscope was a practical possibility. The results seem to indicate that it is.

Do key ?

Chapter 2

THEORY

2.1 THE SAGNAC INTERFEROMETER

The Sagnac interferometer as an inertial rotation sensor is comprehensively discussed by Post[20]. Its geometry is such that an entering beam is split into two components which then travel around a closed-path loop in opposite directions. If the device is rotated, the two beams on being recombined acquire a relative phase shift proportional to the rate of rotation. Thus a Sagnac interferometer performs as a gyroscope.

The effect can be simply explained as follows[20]. Consider an idealised circular interferometer shown in Fig.2.1-1 where the two beams enter and are recombined at the same point.

beam in/out
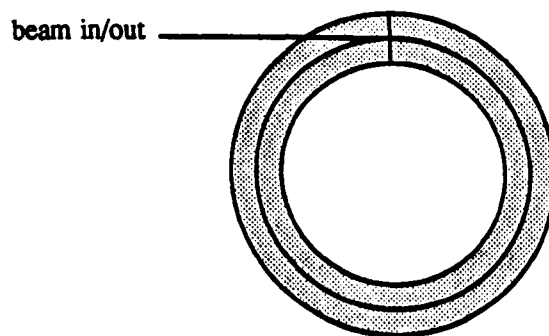
Fig.2.1-1 An idealised Sagnac interferometer.

For a stationary interferometer of radius R the round-trip pathlength and trip time of both beams are :

$$L = 2\pi R$$
$$\tau = \frac{L}{c} = \frac{2\pi R}{c}$$

(2.1.1-1)

If the interferometer is rotating at the rate Ω these become, for the clockwise beam,

$$L_{CW} = 2\pi R + \Omega \tau_{CW} R$$
$$\tau_{CW} = \tau + \Omega\ \tau_{CW} \frac{R}{c} \cong \tau + \Omega \tau \frac{R}{c} \qquad (2.1.1\text{-}2)$$

and for the counter-clockwise beam,

$$L_{CCW} = 2\pi R + \Omega \tau_{CCW} R$$
$$\tau_{CCW} = \tau + \Omega\ \tau_{CCW} \frac{R}{c} \cong \tau - \Omega \tau \frac{R}{c} \qquad (2.1.1\text{-}3)$$

The two round-trip times differ by

$$\Delta\tau = \tau_{CW} - \tau_{CCW} \cong 2\Omega\tau \frac{R}{c} = 4\pi\Omega\left(\frac{R}{c}\right)^2 \qquad (2.1.1\text{-}4)$$

This translates into a relative phase shift

$$\Delta\phi = 2\pi\ \Delta\tau\ \frac{c}{\lambda} = 2\left(\frac{2\pi R}{c}\right)^2 \frac{c}{\lambda}\ \Omega = \frac{8\pi A\Omega}{c\lambda} \qquad (2.1.1\text{-}5)$$

which is proportional to the rate of rotation. The proportionality coefficient is very small: for an interferometer of reasonable size ($A \approx 1m^2$) using visible light, $4A/c\lambda \approx 0.03$. For a very fast rotation rate of 1rpm (as gyroscopes go), the fringe shift is only 0.003. This limitation places low rotation rates below detection threshold.

However, the magnitude of Sagnac effect is dramatically improved by using a ring laser, rather than an interferometer.

2.2 SAGNAC EFFECT IN RING LASERS

2.2.1 Elementary derivation of Sagnac effect in

ring lasers

In a ring laser, Sagnac effect can be simply demonstrated qualitatively by "viewing" the electromagnetic wave inside the ring resonator. The two counter-propagating beams form a standing wave pattern:
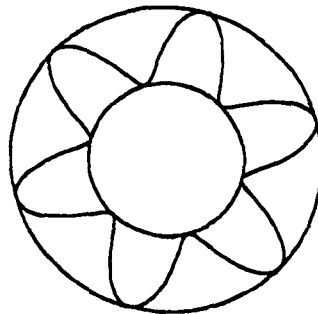
Fig.2.2-1 An idealised representation of a standing wave in a ring resonator.

When the resonator is rotating, a stationary observer sees successive peaks and troughs passing by in the form of fringes. Since the fringe spacing is uniform, the rate at which they do so is clearly proportional to the rate of rotation.

For a more quantitative result, we express Eq.2.2.1-5 in terms of frequency:

$$\Delta v = \frac{\Delta \phi \, c}{2\pi L} = \frac{4\pi R^2}{\lambda L} = \frac{4A\Omega}{\lambda L} \qquad (2.2.1\text{-}1)$$

7

As with the phase shift, the frequency difference between the two counter-propagating beams, Δv, is proportional to the rate of rotation. The proportionality factor $4A/\lambda L$ - called the scale factor, or S-factor, of a ring laser gyroscope - is now much larger, of the order of 10^5counts/rad, and gives rise to an easily measurable frequency. In an ideal gyroscope the scale factor remains constant at all times and in all circumstances.

2.2.2 Sagnac effect in an ring laser of arbitrary shape and rotation axis

A slightly more sophisticated approach allows to calculate Sagnac effect for a ring laser of arbitrary shape and rotation axis[16] (Fig.2.2-2).
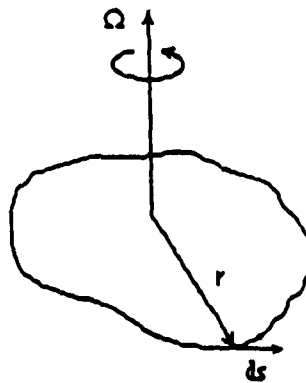
Fig.2.2-2 A ring resonator of arbitrary shape and rotation axis.

For additional accuracy, we will use the effective perimeter of a resonator, that is its round-trip optical pathlength, which can be found from:

$$P = \oint n(s)\, ds \qquad (2.2.2\text{-}1)$$

where $n(s)$ is the varying index of refraction.

Rotation causes the perimeter, as seen by the beam, to change by δP:

$$\delta P = \frac{1}{c}\int_0^{\cdot} v_P\, dP = \frac{1}{c}\oint v\cdot dP \qquad (2.2.2-2)$$

where $v(dP,t)$ is the velocity of the path element dP and v_p is its component along dP. By Stokes' theorem,

$$\oint v\cdot dP = \oint (\nabla\times v)\cdot dA \qquad (2.2.2-3)$$

where dA is an element of the area enclosed by the ring resonator. For a purely rotational field,

$$\nabla\times v = 2\Omega \qquad (2.2.2-4)$$

which upon substitution into Eq.2.2.2-2 gives

$$\delta P = \frac{2\, A\cdot\Omega}{c} \qquad (2.2.2-5)$$

The pathlength difference between the two counter-propagating beams is double this amount, that is

$$\Delta P = 2\delta P = \frac{4\, A\cdot\Omega}{c} \qquad (2.2.2-6)$$

Since the resonance condition requires that a resonator be spanned by an integral number of wavelengths, the pathlength difference translates into frequency difference through the relation

$$\frac{\Delta P}{P} = \frac{\Delta v}{v} \qquad (2.2.2-7)$$

The frequency difference is therefore

$$\Delta v = \frac{4\, A\cdot\Omega}{\lambda P} \qquad (2.2.2-8)$$

For a planar resonator lying in the plane perpendicular to its axis of rotation, this reduces to

$$\Delta v = \frac{4A\Omega}{\lambda P} \qquad (2.2.2-9)$$

This last expression differs from the previous Eq.2.2.1-1 only in that the perimeter P is in this case the effective optical length of the resonator rather than a simple geometric quantity.

2.2.3 Influence of moving medium on Sagnac effect

In the preceding section we assumed that any refractive medium in the beam path was static. The derivation below analyses the influence on the laser gyroscope of moving medium within its resonator[20].

We begin by writing out the rigorous expression for the phase of a beam on completion of a single round trip in a rotating resonator of arbitrary shape containing co-moving medium in the beam path (see Fig.2.2-2 for coordinates):

$$\phi = \frac{1}{2\pi} \oint \mathbf{k} \cdot d\mathbf{s} - \frac{1}{2\pi} \int_0^\tau \omega \, dt \qquad (2.2.3-1)$$

The first integral counts the number of wavelengths in the loop; the second measures the angle that the beam must traverse to complete the circuit. The phase shift induced by rotation is the variation of ϕ in Eq.2.2.3-1:

$$\delta\phi = \frac{1}{2\pi} \left[\oint \delta\mathbf{k} \cdot d\mathbf{s} + (\mathbf{k} \cdot \delta\mathbf{s})_2 - (\mathbf{k} \cdot \delta\mathbf{s})_1 \right] - \frac{1}{2\pi} \left[\int_0^\tau \delta\omega \, dt + \omega \, \delta\tau \right] \qquad (2.2.3-2)$$

where $(\mathbf{k} \cdot \delta\mathbf{s})_1$ and $(\mathbf{k} \cdot \delta\mathbf{s})_2$ are the values of $(\mathbf{k} \cdot \delta\mathbf{s})$ at the beginning and the end of one round trip. We can evaluate the difference:

$$(k \cdot \delta s)_2 - (k \cdot \delta s)_1 = \int_0^\cdot k \cdot v \, dt = \oint k \cdot v \, \frac{ds}{u} \qquad (2.2.3\text{-}3)$$

where $ds^2 = ds \cdot ds$ and $u = c/n$. Since k and ds are co-directional, $k = k(ds/ds)$ and Eq.2.2.3-3 can be rewritten as

$$(k \cdot \delta s)_2 - (k \cdot \delta s)_1 = \oint \frac{k}{u} \, v \cdot ds \qquad (2.2.3\text{-}4)$$

Now we turn our attention to the first term in Eq.2.2.3-2. Although lasing medium is nonlinear, for the sake of simplicity we use a linear medium approximation $\omega = ku$ to obtain

$$\frac{\delta k}{k} = \frac{\delta \omega}{\omega} - \frac{\delta u}{u} \qquad (2.2.3\text{-}5)$$

Here δu is the change in propagation velocity of light in the moving medium as seen by the stationary observer. This change must be proportional to the component of medium velocity along the direction of light propagation $(v \cdot ds)$. We assume therefore that δu has the form

$$\delta u = \alpha v \cdot \hat{ds} \qquad (2.2.3\text{-}6)$$

where the proportionality factor α is a coefficient of drag similar to the Fresnel-Fizeau drag coefficient for translational motion: $\alpha = 1 - n^{-2}$. The first term in Eq.2.2.3-2 then becomes

$$\oint \delta k \cdot ds = \oint \frac{\delta \omega}{\omega} \, k \cdot ds - \oint \alpha \left(v \cdot \frac{ds}{ds} \right) \left(\frac{k}{u} \cdot ds \right) = \int_0^\cdot \delta \omega \, dt \cdot - \oint \alpha \frac{k}{u} v \cdot ds \qquad (2.2.3\text{-}7)$$

where again we have used $ds/u = dt$ and the fact that k and ds are co-directional. Substituting Eq.2.2.3-4 and Eq.2.2.3-7 into Eq.2.2.3-2 gives the phase shift:

11

$$\delta\phi = \frac{1}{2\pi} \oint \frac{k}{u} (1-\alpha) \, v \cdot ds - \frac{1}{2\pi} \omega \, \delta\tau \qquad (2.2.3\text{-}8)$$

To evaluate the integral we use Stokes' theorem (as previously in Sec.2.2.2):

$$\oint \frac{k}{u} (1-\alpha) \, v \cdot ds = \frac{\omega}{c^2} \oint n^2 (1-\alpha) \, v \cdot ds = \frac{\omega}{c^2} \oint [\nabla \times n^2 (1-\alpha) \, v] \cdot dA$$

$$= \frac{2\omega}{c^2} \oint n^2 (1-\alpha) \, \Omega \cdot dA + \oint \{[\nabla n^2 (1-\alpha)] \times v\} \cdot dA \qquad (2.2.3\text{-}9)$$

where we also have made use of $k/u = \omega n^2/c^2$ and $\nabla \times v = 2\Omega$. The second integrand is a triple vector product $[\nabla n^2 (1-\alpha)] \times v \cdot dA$ in which the three vectors are co-planar. The product is therefore zero: the integral vanishes. The first integral can be approximated by replacing $n^2(1-\alpha)$ by its average. The resulting expression for the phase shift is then

$$\delta\phi = \frac{1}{2\pi} \frac{2\omega}{c^2} \overline{n^2 (1-\alpha)} \, A \cdot \Omega - \frac{1}{2\pi} \omega \, \delta\tau \qquad (2.2.3\text{-}10)$$

The resonance condition requires that the round-trip phase shift be zero, $\delta\phi=0$; in consequence,

$$\delta\tau = \frac{2}{c^2} \overline{n^2 (1-\alpha)} \, A \cdot \Omega \qquad (2.2.3\text{-}11)$$

Also, $\omega\tau = 2\pi m$ or $\nu\tau = m$ (where m is the number of wavelengths spanning the resonator), and so

$$\frac{\delta\omega}{\omega} = \frac{\delta\nu}{\nu} = -\frac{\delta\tau}{\tau} \qquad (2.2.3\text{-}12)$$

where the round-trip time τ is found from

$$\tau = \oint \frac{ds}{u} = \frac{1}{c} \oint n \, ds = \frac{P}{c} \qquad (2.2.3\text{-}13)$$

The frequency difference - the "beat" - between the two beams is double the frequency shift, $\Delta v = 2\delta v$, and is thus given by

$$\Delta v = \frac{4\,A\cdot\Omega}{\lambda P}\ \overline{n^2(1-\alpha)} \qquad (2.2.3\text{-}14)$$

The first factor in the expression Eq.2.2.3-14 is the familiar Sagnac formula (compare Eq.2.2.2-8); the second represents the contribution of refractive medium in the beam path. In the case being considered, that of rotating ring laser with co-moving medium, one would not expect to see motion-dependent refractive effects: and indeed, substituting the assumed form of α into Eq.2.2.3-14 does in fact reduce it to Eq.2.2.2-8.

Let us now consider two other cases: that of rotating ring laser with stationary medium; and that of stationary ring laser with moving medium.

For stationary medium $\alpha=0$; hence for a rotating laser with stationary medium Eq.2.2.3.8 becomes

$$\delta\phi = \frac{1}{2\pi}\oint \frac{k}{u}\,v\cdot ds\ -\ \frac{1}{2\pi}\,\omega\,\delta\tau \qquad (2.2.3\text{-}15)$$

Following the previous argument this leads to

$$\Delta v = \frac{4\,A\cdot\Omega}{\lambda P}\ \overline{n^2} \qquad (2.2.3\text{-}16)$$

Note that the effect of the medium in this case is to multiply the S-factor by a constant. Since the refractive index is a function of frequency, the S-factor will also be a function of frequency. However, gyroscopes are made with their beam path totally enclosed; therefore in practice this does not constitute a problem.

In the case of stationary ring laser and moving medium, $(k\cdot\delta s)_2-(k\cdot\delta s)_1=0$. As a result, Eq.2.2.3.8 is replaced by

$$\delta\phi \;=\; -\frac{1}{2\pi}\oint \frac{k}{u}\,\alpha\, v\!\cdot\! ds \;-\; \frac{1}{2\pi}\,\omega\,\delta\tau \qquad (2.2.3\text{-}17)$$

leading to

$$\Delta v \;=\; \frac{2\,A\!\cdot\!(\nabla\times v)}{\lambda P}\,\overline{n^{2}\alpha} \qquad (2.2.3\text{-}18)$$

where v is the velocity of the medium. Here the effect of the medium is to add a constant component to the S-factor - a null-shift - which can be significant.

Indeed, the effect can be utilised to bias the gyroscope. For this purpose a rapidly vibrating Brewster window is inserted into the resonator. Assuming the window thickness to be ~1% of the resonator length, the refractive index of glass ~1.5, the gyroscope scale factor ~10^{5}counts/rad and the vibration velocity ~1m/s: the resulting alternating bias frequency will be ~10kHz.

2.2.4 Sagnac effect in general relativity

Since a rotating gyroscope is a non-inertial system, a rigorous derivation of Sagnac effect ought to be carried out within the framework of general relativity[9].

The wave equation for the electric field in a ring laser in the presence of gravitation is given by

$$\frac{1}{c^{2}}\frac{\partial^{2}E}{\partial t^{2}} \;-\; \nabla^{2}E \;=\; -\frac{2}{c}\,(h\!\cdot\!\nabla)\frac{\partial E}{\partial t} \qquad (2.2.4\text{-}1)$$

This is derived in the usual way from the Maxwell equations together with the material equations

$$D \;=\; E - c(B\times h)$$

and

$$B \;=\; H + (E\times h)/c$$

14

where h is the gravitational field. In the derivation terms of order h^2 and all derivatives of h have been neglected. We use Eq.2.2.4-1 to calculate Sagnac effect. We will assume a planar gyroscope of arbitrary shape and effective perimeter P (see Fig.2.2-2 on p.8). The electric field is of the form

$$E = E_0 \exp\left[i\left((\omega + \delta\omega)t + \int_L k(r')\cdot dr' + \phi(r)\right)\right] \qquad (2.2.4\text{-}2)$$

where the frequency shift $\delta\omega$ is due to rotation. To keep the electric field constant along the path of the light beam (for the sake of simplicity) we assume that the beam is polarised perpendicularly to the plane of the gyroscope (the s-mode of Sec.2.3.2 below). Substituting the field (Eq.2.2.4-2) into the wave equation (Eq.2.2.4-1) while remembering that E_0 is constant gives

$$\frac{1}{c^2}(\omega + \delta\omega)^2 - (k + \nabla\phi)^2 = -2\frac{\omega}{c}\, h\cdot k \qquad (2.2.4\text{-}3)$$

where higher order terms have been neglected. We can simplify the right-hand side by neglecting second-order terms in $\delta\omega$ and $\nabla\phi$ and remembering that $k = \omega/c$:

$$\text{LHS} \cong 2\frac{\omega}{c^2}(\delta\omega - c\,\hat{k}\cdot\nabla\phi)$$

Eq.2.2.4.-3 then becomes

$$\delta\omega - c\,\hat{k}\cdot\nabla\phi = -\omega\left(h\cdot\hat{k}\right) \qquad (2.2.4\text{-}4)$$

leading to a solution in terms of round-trip phase shift:

$$\phi = \frac{\delta\omega}{c}\oint dr\cdot\hat{k}(r) + \frac{\omega}{c}\oint dr\cdot h(r) = \frac{\delta\omega\, P}{c} + \frac{\omega}{c}\oint dr\cdot h(r) \qquad (2.2.4\text{-}5)$$

It follows from the resonance condition (the round-trip phase shift must be zero) that

$$\delta\omega = -\frac{\omega}{P}\oint dr\cdot h(r) \qquad (2.2.4\text{-}6)$$

This is the angular frequency shift of the electromagnetic wave travelling around a ring resonator in a gravitational field. After doubling and applying Stokes' theorem (while neglecting derivatives of h) it translates into the more convenient form:

$$\Delta v \;=\; -\,\frac{2v}{P}\int_{A} dA\cdot(\nabla\times h) \;\equiv\; -\,\frac{2c}{\lambda P}\,(\nabla\times h)\cdot A \qquad (2.2.4\text{-}7)$$

The metric vector h in a rotating frame is found by assuming $g_{0i}=h_{0i}$ and transforming ds^2 to a rotating frame:

$$ds^2 \;=\; g_{00}\!\left(dx^0\right)^2 + g_{\alpha}\,dx^0 dx^i + g_{ij}\,dx^i dx^j \qquad (2.2.4\text{-}8)$$

$$= \left[1 - \frac{\Omega^2\!\left(x'^2 + y'^2\right)}{c^2}\right]c^2 dt'^2 - \left(dx'^2 + dy'^2 + dz'^2\right) + 2\Omega\,\frac{y'}{c}\,c\,dt'\,dx' + 2\Omega\,\frac{x'}{c}\,c\,dt'\,dy'$$

This implies

$$h_{01} = (\Omega/c)y' \qquad h_{02} = (\Omega/c)x' \qquad h_{03} = 0 \qquad (2.2.4\text{-}9)$$

and therefore

$$(\nabla\times h)\cdot\hat{z} \;=\; -\,\frac{2\Omega}{c} \qquad (2.2.4\text{-}10)$$

Substituting this into Eq.2.2.4-7 finally gives the Sagnac frequency shift:

$$\Delta v \;=\; \frac{4A\Omega}{\lambda P} \qquad (2.2.4\text{-}11)$$

which is the familiar expression arrived at in Sec.2.2.2.

Since the metric used in deriving the components of the field in Eq.2.2.4-8 is that of flat space, the final expression (Eq.2.2.4-10) describes Sagnac effect in a uniform gravitational field: a gyroscope operating on Earth will deviate slightly from the formula due to the gravitational field of the rotating Earth. The actual output frequency - assuming rotation parallel to the Earth axis - will be[9]

$$\Delta v_E \;=\; S\,[\,\Omega + \Omega_E + \alpha T_\alpha + \beta T_\beta + \gamma T_\gamma\,] \qquad (2.2.4\text{-}12)$$

where S and Ω are the scale factor and rotation rate of the gyroscope and Ω_E is the Earth rotation rate. The terms αT_α, βT_β and γT_γ arise respectively from the "preferred frame effect" (the presence or absence of a preferred rest frame in the Universe - zero in the Einstein theory but finite in some other cosmologies), space curvature effect (space curvature caused by the mass of the Earth) and Lense-Thirring effect (the "dragging" of the gyroscope by the rotation of the Earth). The coefficients α, β and γ possess different values in various theories of metric gravity. Although at present the discrepancy is below detection threshold (the largest is $\Delta v_E/\Omega \approx 10^{-7}\alpha$, where $|\alpha|<0.02$), in principle an accurate measurement of Δv can discriminate between those theories.

2.2.5 Scale factor errors

As we have seen in Sec.2.2.2, the frequency of the output signal of an ideal ring laser gyroscope is proportional to the rate of rotation, the proportionality coefficient, the scale factor, being a constant of the system. In reality, however, this is not the case: the observed scale factor is subject to various distortions and deviations from linearity; these fall broadly into four categories.

The dominant one - both in terms of magnitude and the practical problem it represents - is the frequency locking (synchronisation) of the counter-propagating beams which occurs at low rates of rotation and creates a low cut-off threshold at around 10^3deg/hr. This effect, commonly known as 'mode lock-in', will be discussed in full in Ch.2.4.

Another type of error is the null-shift which, as its name suggests, amounts

to adding a rotation-independent component to the output frequency:

$$f_{out} = S\Omega + f_{null}$$

The main source of this effect is the Langmuir flow of gas in the discharge. This occurs in DC-excited plasmas and stems from the fact that the dielectric walls of the discharge tube collect negative charge[4]. As a result, positive ions moving towards the cathode are attracted to the walls, while electrons moving towards the anode are repelled to the centre. To maintain the overall momentum balance, neutral atoms which are responsible for gain are compelled to move towards the anode along the walls and towards the cathode along the centre (Fig.2.2-3):
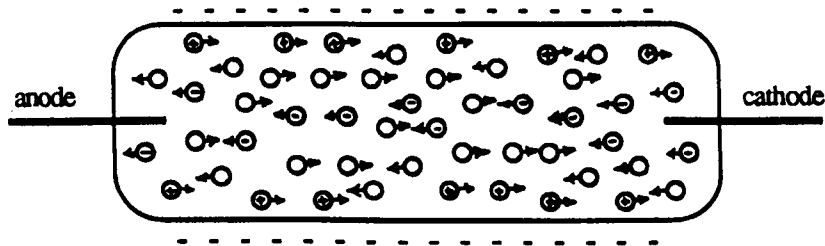
Fig.2.2-3   Langmuir flow of charges and neutral atoms in a DC dischage.

In consequence, the radiation in a resonator, travelling mainly along the centre of the discharge, interacts with a moving gain medium. The motion Doppler-shifts the transition frequency, so that dispersion effects become dependent on the beam direction. This results in differential mode pulling and hence a null-shift (see below) which is approximately linear with the discharge current. The Langmuir-induced null-shift has been variously measured to be between 6.6(deg/hr)/mA[6] and 480(deg/hr)/mA[19]. Since Langmuir flow is in some respects a convection-like effect, it depends to a great extent on the tube geometry and aspect ratio.

The usual method of circumventing the problem is to use a double-arm discharge[31], powered by equal currents flowing in opposite senses; the two components of the null-shift then cancel each other.

For different reasons, null-shift also arises whenever the resonator is anisotropic with respect to radiation travelling in the two directions; it is then due to differential mode pulling and/or pushing[31] (see Sec.2.3.1 below). Both effects depend on the effective gain, so any phenomenon resulting in non-reciprocal losses or gain will automatically lead to differential mode pulling/pushing and hence to null-shift.

Mode pulling is also responsible for the third type of scale-factor error, the rotation-dependent variation. Linear mode pulling (see Sec.2.3.1) reduces mode separation, and thus signal frequency, by a constant factor; the nonlinear component adds to this a rotation-dependent variation (since mode separation is proportional to rotation). However, nonlinear mode pulling effects in a He-Ne laser operating at $0.6328\mu m$ are of the order 10^{-7} (that is, mode spacing changes by a factor of $(1 - 10^{-7})$).

The fourth type of error arises from pathlength variation, due mainly to thermal expansion, and leads to scale factor variation in direct proportion. In a solid-block Zerodur gyroscope the pathlength can change by approximately one wavelength per $40°C$. Nevertheless, pathlength variation can be easily offset by installing a pathlength control circuit.

2.3 THE HE-NE RING LASER

2.3.1 Transition characteristics and lineshape

A ring laser used as a gyroscope must oscillate on two frequencies simultaneously; as a consequence, it is necessary that the gain profile be predominantly inhomogeneously broadened. Solid state lasers, having homogeneously broadened lines, are therefore unsuitable for the purpose. Furthermore, since the gyroscope scale factor is inversely proportional to the wavelength, it is desirable that the wavelength be as short as possible. These two considerations, together with the simplicity of design and small dimensions, combined to establish the $0.633\mu m$ He-Ne laser as the one universally used in ring laser gyroscopes.

Fig.2.3-1 shows the transition diagram of the He-Ne laser[32]. Ne atoms are excited by collisions with He atoms to the $3s^2$ level, from where they decay radiatively to the $2p^4$ level giving rise to the $0.6328\mu m$ laser transition; the lower $1S$ level is depopulated through diffusion to walls. The exponential gain achieved is of the order of $0.1m^{-1}$. The infrared transitions must be suppressed, as their gain is proportionally higher*.

---

* Gain, for an atom which can undergo several possible transitions, is linear in wavelength[7]. Thus gain of the $3.39\mu m$ transition is ≈5.4 times higher than that of the $0.6328\mu m$ transition.
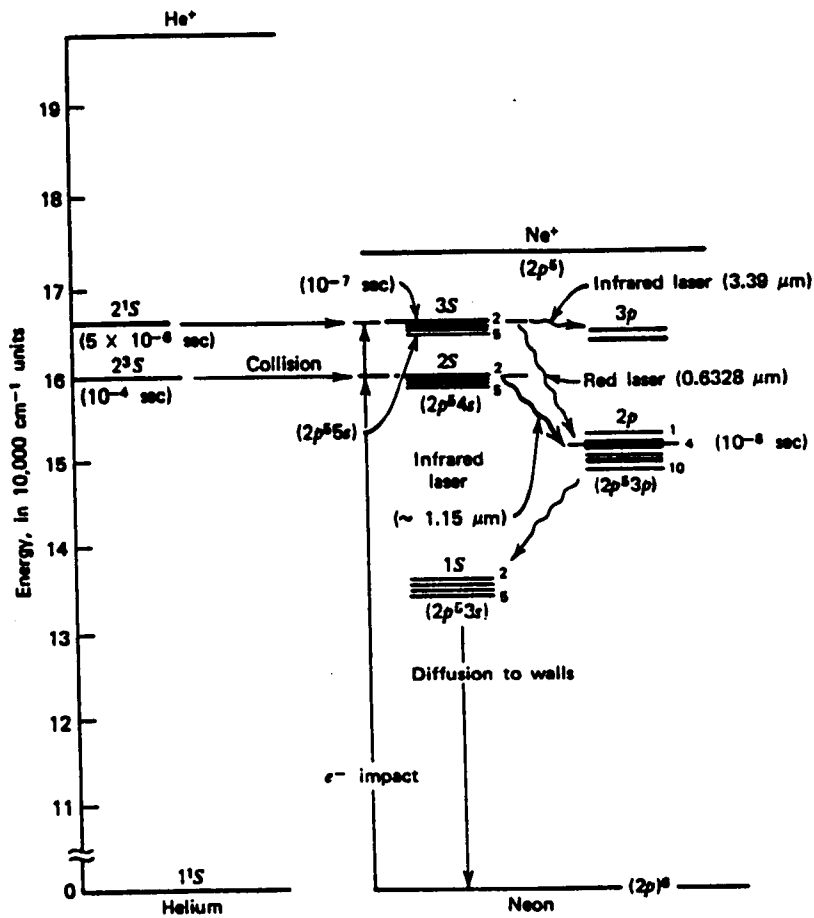
Fig.2.3-1 Transition diagram of the He-Ne laser.

The natural linewidth can be estimated from the lifetime of the 3S level: $\Delta v_N = \pi^{-1} 10^7 \approx 3MHz$ (FWHM). However, homogeneous width is greatly increased by collision broadening which is linear in pressure (this is because, qualitatively, pressure is a measure of collision rate). The full Lorentz linewidth (homogeneous) for the total gas pressure of 1Torr has been measured to be[25] $\Delta v_L = 160MHz$ (FWHM). (In high-gain lasers there is the added effect of power broadening, but in the He-Ne this is negligible.)

The Doppler linewidth (inhomogeneous) can be calculated from[32]

$$\Delta v_D = 2 v_0 \sqrt{\frac{2kT \ln 2}{Mc^2}} \qquad (2.3.1\text{-}1)$$

21

which gives the width of ≈1400MHz (FWHM).

Consequently, in a He-Ne laser $\Delta v_L/\Delta v_D \approx 0.1$ at 1Torr and ≈0.5 at 4.5Torr - the inhomogeneos component predominates as required.

The full width of the gain curve is given by the convolution of the Gaussian and Lorenztian functions, which turns out to be the real part of the complex error function $w(z) = \exp(-z^2)\mathrm{erfc}(-iz)$:

$$\mathrm{Re}\ w(x+iy) = \frac{1}{\pi} \int_{-\infty}^{\infty} \frac{y\, e^{-t^2}\, dt}{(x-t)^2 + y^2}$$

$$x = \frac{v - v_0}{\Delta v_D} \qquad y = \frac{v_L}{v_D}$$

(2.3.1-1)

The integral has no analytic solution, but has been extensively tabulated (e.g. Ref.1). The tables show that for $y=0.1$ (≈1Torr) the gain curve is widened by ≈10%: the total width is $\Delta v_T \approx 1500$MHz; for $y=0.5$ (≈4.5Torr) the correction is ≈30%: $\Delta v_T \approx 1800$MHz.

Inhomogeneously broadened lasers are subject to the phenomenon of "hole burning". The Gaussian profile of the gain curve derives from the Maxwellian distribution of atom velocities in gas. As the laser oscillates on one of the resonator frequencies, the upper level atoms with energies corresponding to that frequency become depleted, with the consequence that gain at that point is reduced (see Fig.2.3-2a) and a "hole" appears. The gain profile seen by a "probe" beam of frequency v' in the presence of an already oscillating frequency v is then[32]

$$\gamma(v') = \gamma_0 \left[\frac{\left(\frac{\Delta v_L}{2}\right)^2 + (v - v')^2}{\left(\frac{\Delta v_L}{2}\right)^2 + (v - v')^2 + C\left(\frac{\Delta v_L}{2}\right)} \right]$$

(2.3.1-3)

22

a   b
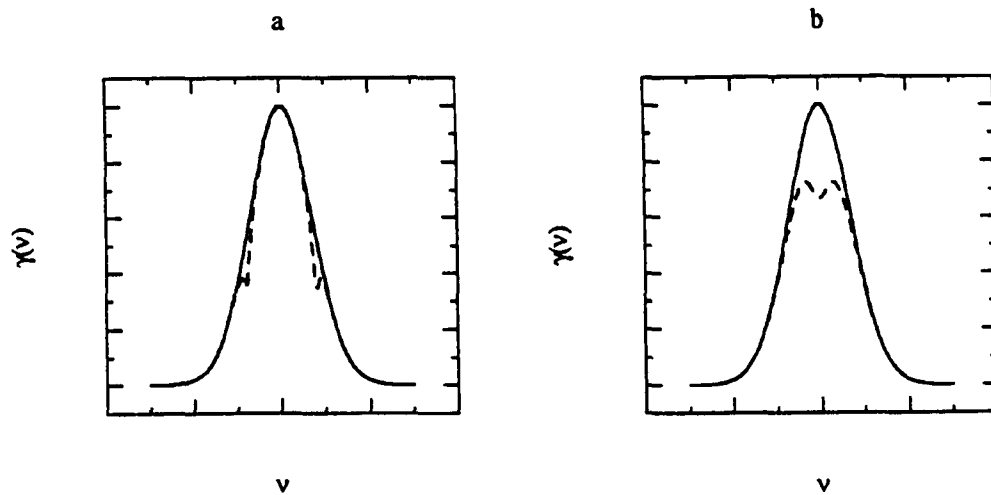
Fig.2.3-2 Gain profile of an inhomogeneously broadened line:

a) oscillating away from line centre; b) oscillating at line centre.

where γ_0 is the Gaussian profile and C a constant which depends on the parameters of the medium. Δv_L is the homogeneous width of the hole, approximately equal to the Lorentz width; the depth of the hole is $(1+2C/\Delta v_L)^{-1}$. The second hole is due to the fact that radiation travelling in the reverse direction interacts with a different set of atoms, those with velocities of negative sign, and therefore situated symmetrically on the opposite slope of the gain curve. When the laser is operated at the line centre, the two holes merge and become a "Lamb dip" (Fig.2.3-2b).

In a ring laser, hole burning leads to mode competition at the centre of the gain curve[4], that is in the region $v_0-\Delta v_L/2 < v < v_0+\Delta v_L/2$, with one of the counter-propagating modes losing intensity or even disappearing altogether. This occurs because the frequency difference between the two modes - the gyroscope frequency - is typically less than 50kHz and therefore much smaller than the hole width; as a result, at the line centre both modes interact essentially with the same group of atoms, and so must compete for gain in a 'winner takes all' situation similar to that prevailing in homogeneously broadened gain media.

Here the crucial difference between a linear and a ring laser lies in the fact that in the linear laser the selfsame mode travels in both directions and so cannot compete against itself, while in the ring laser the two couter-propagating modes are independent and thus can compete with each other to the extent that one becomes extinguished altogether.

Mode competition clearly interferes with the operation of the device; for this reason ring laser gyroscopes are filled with an equal mixture of two isotopes[31] of Ne: Ne^{20} and Ne^{22} (the natural abundance is respectively 91% and 9%). The line centres of the two isotopes are separated by 875MHz, the combined linewidth is therefore ~2400MHz at 1Torr and ~2700MHz at 4.5 Torr.

In a two-isotope medium, the maximum of the combined gain curve lies (approximately equidistant) between the maxima of the two individual isotope lines (see Fig.2.3-3a). Thus, if one mode is burning a hole at the centre of the combined curve, the other will burn two holes down at the sides, separated by the frequency spacing of the isotopes[31] (see Fig.2.3-3b). This can be simply understood by regarding the two gain curves individually and then adding the effects arithmetically. Quantitatively, this is equivalent to inserting two terms on the right side of Eq.2.3.1-2, one for each isotope.

Although the two-isotope gain curve possesses two "Lamb dips" centred on the peaks of the two lines (Fig.2.3-3b), competition is eliminated.

a

$\gamma(\nu)$

$\nu(22)$ $\nu(20)$

ν

b

$\gamma(\nu)$

$\nu(22)$ $\nu(20)$

ν
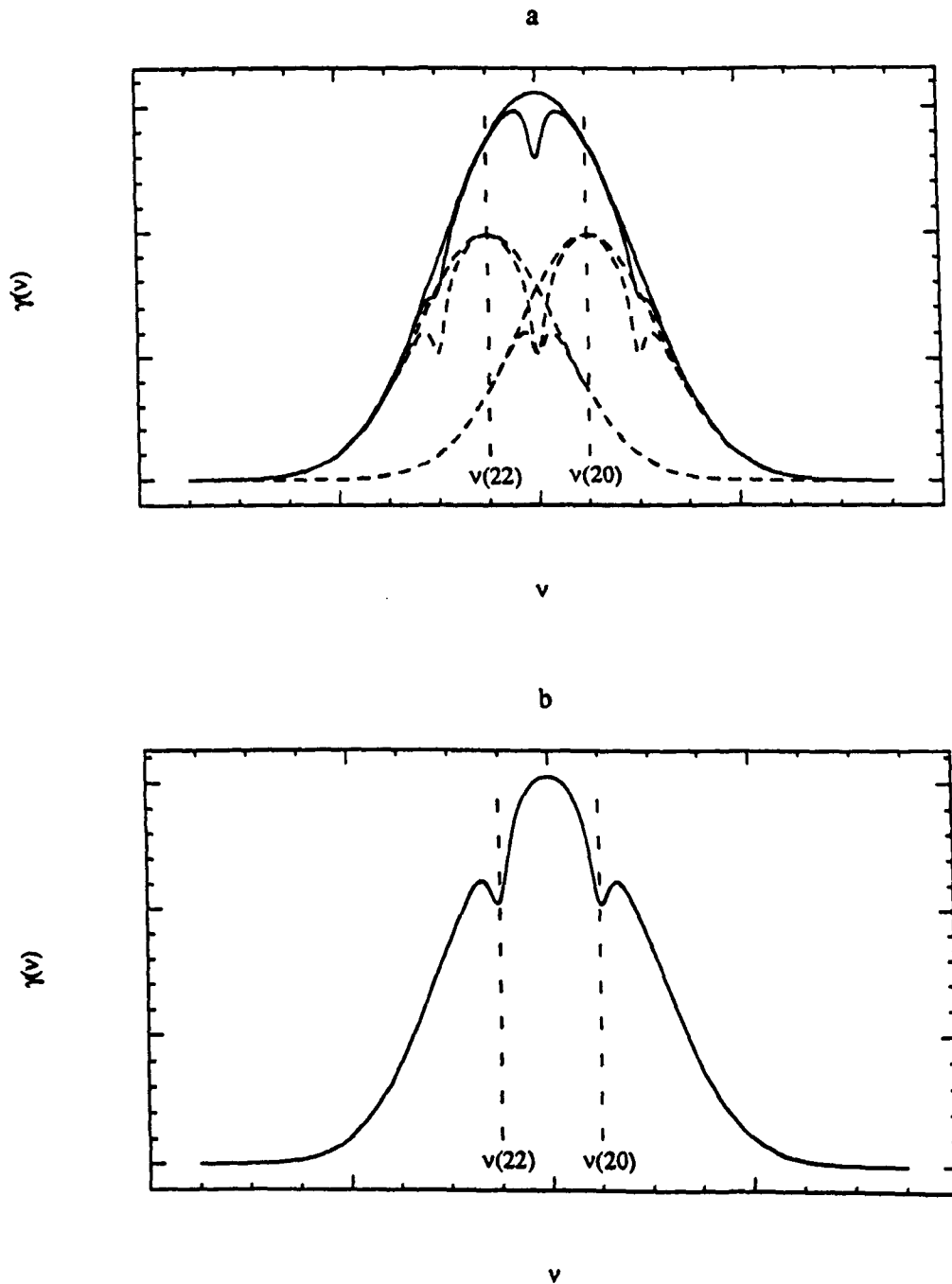
Fig.2.3-3 The combined gain curve for a two-isotope medium:

a) non-competing hole burning; b) effective gain profile.

Mode pulling

Mode pulling arises from the anomalous dispersion obtaining in gain medium, and, true to its name, causes the frequency of the oscillating mode to shift towards the line centre[8]:

$$\nu = \frac{\nu_m}{1 + \frac{D}{L}(n\text{-}1)} \qquad (2.3.1\text{-}4)$$

where ν_m is the frequency of the resonator mode and D the length of the active medium (discharge). The refractive index n is given by[11] (Fig.2.3-4)

$$n = 1 + \frac{cG}{2\pi\nu} F\left(\frac{\nu\text{-}\nu_0}{\Delta\nu_D}\right) \qquad (2.3.1\text{-}5)$$

where G is gain. In the limit of inhomogeneous broadening $(\Delta\nu_L << \Delta\nu_D)$ the function $F(x)$ is the Gaussian dispersion function*:

$$F(x) = \frac{2}{\sqrt{\pi}} e^{-x^2} \int_0^x e^{t^2} dt \qquad (2.3.1\text{-}6)$$

For lines near the centre of the gain curve $(x \leq 0.5)$, $F(x)$ can be approximated by $F(x) \approx x$. The oscillating frequency is then given by

$$(\nu - \nu_0) = (\nu_m - \nu_0)(1 - \delta)$$

$$\delta = \frac{D}{L} \frac{cG}{\pi^{2/3} \Delta\nu_D} \qquad (2.3.1\text{-}7)$$

---

* Otherwise the imaginary part of the complex error function (essentially the complex conjugate of the "plasma dispersion function") $w(z) = \exp(\text{-}z^2)\mathrm{erfc}(\text{-}iz)$ must be used[1,11]:

$$\mathrm{Im}\, w(x\text{+}iy) = \frac{1}{\pi} \int_{\text{-}\infty}^{\infty} \frac{(x\text{-}t)\, e^{\text{-}t^2}\, dt}{(x\text{-}t)^2 + y^2}$$

This is the linear mode pulling effect which shifts frequencies in direct proportion to their distance from the line centre. The result is a uniform reduction of mode spacings:

$$\Delta v / \Delta v_0 = 1 - \delta \qquad (2.3.1\text{-}8)$$

For a low-pressure He-Ne laser $(G \approx 0.1 \text{m}^{-1}, \Delta v_D \approx 1.5 \cdot 10^9)$ the reduction factor is $\delta \approx 0.003$.

Homogeneous broadening (i.e. significant $y = \Delta v_L / \Delta v_D$), on the other hand, stretches the curve in Fig.2.3-4 horizontally and so reduces mode pulling, decreasing the overall effect. For $y = 0.5$ (≈ 4.5Torr), the reduction factor is halved, $\delta \approx 0.0015$.

The scale factor, measuring as it does mode spacing, is similarily reduced by $(1 - \delta)$. Nevertheless, as long as the reduction is constant and uniform, it does not affect the accuracy of the measurement. However, the accuracy is compromised if the two counter-rotating beams experience different gain. The reduction factor, which is linear in gain, is then different for the two beams: the scale factor correction acquires a bias.
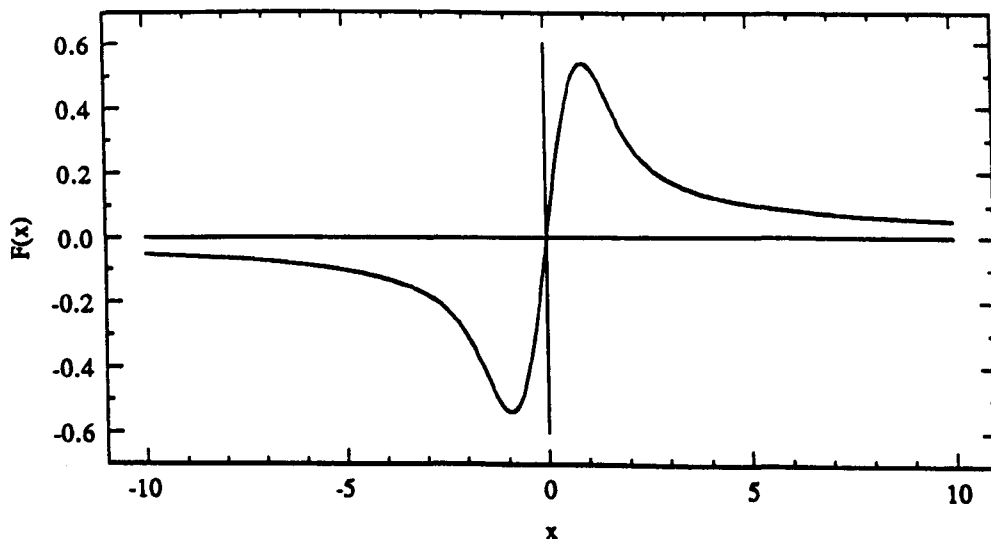
Fig.2.3-4 The anomalous dispersion $F(x) \propto n\text{-}1$ in a gain meduim.

2.3.2 Mode structure in a ring laser

Ring resonator modes differ from those of a linear resonator in two respects[12].
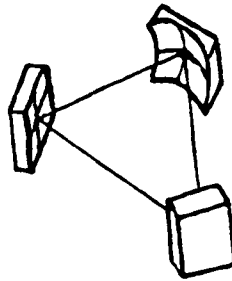
Fig.2.3-5 A three-mirror ring resonator with one curved mirror.*

In the first place, a round trip is completed over one resonator length: therefore $L=m\lambda_m$, and the longitudinal mode spacing is

$$\Delta\nu_{long} = \frac{c}{L} \qquad (2.3.2\text{-}1)$$

In the second place, the angle of incidence at mirrors is far from zero (see Fig.2.3-4). For a three-mirror resonator it is $\pi/6$; in the general case of an N-mirror polygonal resonator it becomes $\pi(N-2)/2N$. As a result, the two orthogonal transverse modes encounter different effective radii:

$$R_- = R\,\frac{\cos\theta}{2} \qquad \text{horizontal}$$
$$R_+ = R\,\frac{1}{2\cos\theta} \qquad \text{vertical} \qquad\qquad (2.3.2\text{-}1)$$

where θ is the angle of incidence, and $+$ and $-$ stand for vertical and horizontal respectively.

---

* I am indebted for this drawing to Mr. Kevin Wells.

For a plane polygonal ring resonator with N mirrors, one of them curved, the resonant frequencies are given by

$$\nu_{qnm} = \frac{c}{2L}\left[2q + \frac{1}{\pi}\left(n + \frac{1}{2}\right)\cos^{-1}\left(1 - \frac{L}{2R_-}\right) + \varepsilon + \frac{1}{\pi}\left(m + \frac{1}{2}\right)\cos^{-1}\left(1 - \frac{L}{2R_+}\right)\right] \quad (2.3.3\text{-}2)$$

$$\varepsilon = 0, \; N \text{ even}; \qquad \varepsilon = \left\{ \begin{array}{ll} 0 & \text{l even} \\ 1 & \text{l odd} \end{array} \right., \; N \text{ odd}$$

The ε term arises from a coordinate reversal in the plane of the ring due to an odd number of mirrors. Apart from this and the factor of 2 multiplying the longitudinal mode number q, Eq.2.3.3-2 differs from that for a linear symmetrical resonator only in the use of different effective radii in the vertical and horizontal planes.

The beam cross-section is affected in similar fashion. The TEM_{00} mode profile becomes elliptic[32]:

at waist,

$$w_{0\pm} = \left(\frac{\lambda}{\pi}\right)^{\frac{1}{2}}\left[\frac{L}{2}\left(R_\pm - \frac{L}{2}\right)\right]^{\frac{1}{4}} \quad (2.3.2\text{-}3)$$

at the curved mirror (the widest point),

$$w_\pm = \left(\frac{\lambda L}{2\pi}\right)^{\frac{1}{2}}\left[\frac{R_\pm^2}{\frac{L}{2}\left(R_\pm - \frac{L}{2}\right)}\right]^{\frac{1}{4}} \quad (2.3.2\text{-}4)$$

In a three-mirror resonator the difference between the axes can be as great as 50%.

The transverse modes likewise have different dimensions*:

$$w \text{ (TEM}_{01}) \approx 1.5 \, w_+ \qquad\qquad (2.3.2\text{-}5)$$

$$w \text{ (TEM}_{10}) \approx 1.5 \, w_-$$

In consequence, the losses they experience are also unequal and may cause one of them to be suppressed.

Effect of Brewster windows

A ring laser resonator may incorporate Brewster windows. These are usually aligned to achieve polarisation either parallel to the axis of rotation (s-mode) or in the plane of the resonator (p-mode)[28,31].

The s-mode is not affected by the non-zero angle of incidence at the mirrors, and is therefore more efficient. For the same reason, calculations are commonly performed assuming s-mode polarisation.

The p-mode is used in gyroscope systems containing magnetic mirrors, as it is necessary for their operation.

---

* The relation between different spot sizes derives from the expression for Gaussian beam modes[32]:

$$E(x,y) = E_0 \frac{w_0}{w} H_n\left(\sqrt{2}\,\frac{x}{w}\right) H_m\left(\sqrt{2}\,\frac{y}{w}\right) \exp\left(-\frac{x^2 + y^2}{w^2}\right)$$

The $H_{n,m}$'s are Hermite polynomials, the first two of which are[1]

$$H_0(\rho) = 1$$

$$H_1(\rho) = 2\rho$$

The field falls to $1/e$ of its maximum value at $\rho = 1$ for H_0 and at $\rho = 1.5$ for H_1.

30

2.3.3 Discharge parameters

In a He-Ne laser the primary excitation of He atoms is effected by a DC glow discharge. The low-pressure discharge presents a negative resistance to the driving voltage source[29]: balance resistance is therefore required to stabilise the circuit.

Gain occurs in the positive column region[29] (Fig.2.3-6): laser gyroscopes are designed so that only the positive column lies in the beam path.
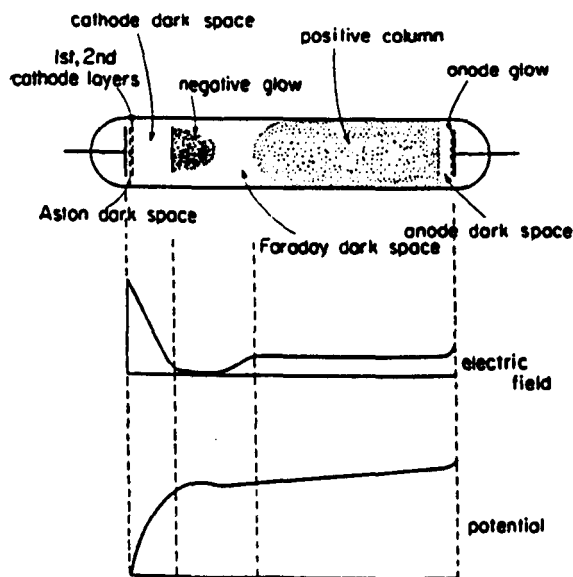
Fig.2.3-6 Spatial distribution of low-pressure DC glow discharge.

As can be seen in Fig.2.3-1(transition diagram), the discharge excites He atoms which then transfer their energy on to Ne atoms through collisions. The density of excited atoms increases with current, enhancing the gain[7]. At higher currents, however, gain starts to decline due to parasitic excitation of lower laser levels. He-Ne lasers typically operate at ~1mA.

Since the lower laser level is depopulated by diffusion to walls, gain

increases with reduced bore diameter[7]. Ideed, the lower bound to the bore diameter is set by the point at which diffraction losses overcome any further growth in gain (gain grows in inverse proportion to diameter, while losses grow as its inverse square).

High pressure accelerates the rate of exciting collisions. On the other hand, it also promotes de-excitation through collisions with walls. The two factors together explain the experimental observation that gain is a function of pressure×diameter[31]. Decreased diameter therefore requires elevated pressure to maintain gain. This consideration places another lower bound on the bore diameter.

The outcome[31] is a typical bore size of 1-5mm. The typical pressure is 1-10Torr, and the gas mixture He:Ne=10:1. The exponential gain has been empirically found to be[26]

$$G \approx 3 \cdot 10^{-4} / d_{bore} \approx 0.1 m^{-1}$$

Fortunately, the operation of a ring laser gyroscope does not require high output power, but only stable non-competing modes.

2.4 MODE LOCK-IN IN RING LASER GYROSCOPES

2.4.1 Mode lock-in and backscattering

Mode lock-in - that is, frequency locking of the two counter-propagating beams - is the most important source of error in the ring laser gyroscope scale factor. Mode lock-in is caused by weak mutual coupling of the two beams; indeed, the effect is similar to the synchronisation of weakly coupled oscillators and is in many respects analogous to the phenomenon observed in coupled- lasers systems[10,27]. In ring lasers, coupling arises through backscattering of the beams into each other's paths: this occurs at the surface of every optical component within the resonator. The direct consequence is a complete loss of sensitivity at low rates of rotation - a "dead" band around zero - as well as large scale factor nonlinearity in the lower part of the sensitive region, as shown in Fig.2.4-4 on p.42 below.

The coupling effect can be explained qualitatively by referring to Fig.2.2-1 on p.7 - a standing wave rotating in an idealised ring resonator. Consider a scatterer within the resonator whose dimensions are small compared with the wavelength[31]: the scattered energy is then a function of the wave position, minimum at a node and maximum at an anti-node. The energy subtracted from each beam will depend therefore on the relative phase of the other beam. It is

33

this mutual phase-dependence which constitutes the physical basis of mode coupling.

The relationship can be demonstrated graphically by using a "phase-vector" diagram[4,31] (Fig.2.4-1 on next page). This shows the electric fields of the two beams as vectors with the relative phase ψ. The "+" vector is taken as a reference; the "-" vector rotates about it at a rate $\dot{\psi}=S\Omega$ which is the gyroscope signal frequency.

Adding the backscattered components in anti-phase (Fig.2.4-1a) changes the phase difference ψ (and thus the output frequency): locking occurs when the opposing effects of scatter and rotation cancel out and the two vectors remain stationary (implying $\dot{\psi}=0$ and zero frequency). By contrast, in-phase scattering (Fig.2.4-1b) clearly does not affect the phase difference ψ and so does not lead to lock-in.

Assuming that the intensities of the counter-propagating beams are equal ($|E+|=|E-|$) and that the backscattering is low ($r<<1$), the relative phase ψ in Fig.2.4-1a is given by

$$\dot{\psi} \approx S\Omega - 2\frac{c}{L}r\sin\psi \qquad (2.4.1-1)$$

where the factor c/L was inserted to preserve the rate-of-change dimensions. It is immediately obvious that for $S\Omega < 2(c/L)r$ - i.e. below "threshold" - Eq.2.4.1-1 has two stationary solutions $\psi=\pi/2$ and $3\pi/2$ indicating locking. Thus the approximate Eq.2.4.1-1 is qualitatively similar to the more rigorous expression to on p.40 below.
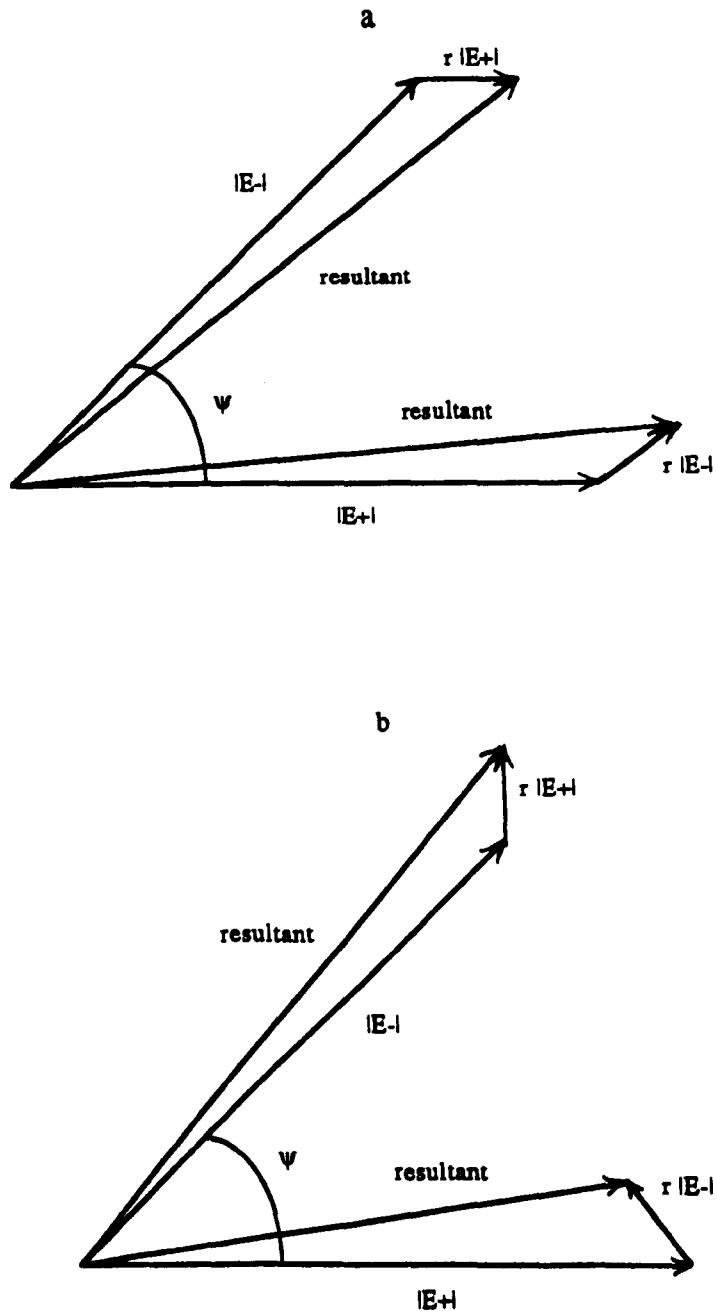
Fig.2.4-1 A phase-vector diagram demonstrating effects of backscattering:

a) anti-phase; b) in-phase.

To derive the lock-in equation, we start with the wave equation for a rotating ring laser (in MKS units)[4,10,18,22,31]:

$$\nabla^2 E + \mu_0 \varepsilon_0 \frac{\partial^2 E}{\partial t^2} + \mu_0 \varepsilon_0 \frac{\partial}{\partial t}\left[\nabla \times (v \times E) + v \times (\nabla \times E)\right] = -\mu_0 \frac{\partial}{\partial t}\left(J + \frac{\partial P}{\partial t}\right) \qquad (2.4.1\text{-}2)$$

where, as in Sec.2.3, v is the velocity of a path element (see Fig.2.2-2 on p.8). The current density J is a convenient way of representing energy losses. For the sake of simplicity we will assume that the resonator lies in the plane perpendicular to the axis of rotation and that the field E is polarised parallel to that axis (the s-mode of Sec.2.3.2). We therefore substitute $\nabla = s(\partial/\partial s)$ and $E=E(s,t)z$ into Eq.2.4.1-2 to obtain

$$\nabla^2 E = -\frac{\partial^2 E}{\partial s^2}\hat{z}$$

$$\nabla \times (v \times E) = -\hat{s} \cdot v \frac{\partial E}{\partial s}\hat{z} \qquad (2.4.1\text{-}3)$$

$$v \times (\nabla \times E) = -\hat{s} \cdot v \frac{\partial E}{\partial s}\hat{z}$$

As a further simplification, $s \cdot v$ is averaged over the entire path:

$$\overline{\hat{s} \cdot v} = \frac{1}{L} \oint v \cdot ds = \frac{1}{L} \oint (\nabla \times v) \cdot dA = \frac{2A\Omega}{L} \qquad (2.4.1\text{-}4)$$

where, as in Ch.2.3, we used Stoke's theorem. In addition, we introduce $J = \sigma E$. These changes lead to Eq.2.4.1-2 being transformed into

$$c^2 \frac{\partial^2 E}{\partial s^2} - \frac{\partial^2 E}{\partial t^2} + \frac{4A\Omega}{L}\frac{\partial^2 E}{\partial s \partial t} - \frac{\sigma}{\varepsilon_0}\frac{\partial E}{\partial t} = -\frac{1}{\varepsilon_0}\frac{\partial^2 P}{\partial t^2} \qquad (2.4.1\text{-}5)$$

We are looking for a solution of the form

$$E(s,t) = \frac{1}{2}\left(E_+ e^{-i\phi_+} + E_- e^{-i\phi_-}\right) + c.c.$$

$$P(s,t) = \frac{1}{2}\left(P_+ e^{-i\phi_+} + P_- e^{-i\phi_-}\right) + c.c.$$

$$(2.4.1\text{-}6)$$

where "+" and "-" refer to the clockwise and counter-clockwise beams, and

$$\phi_\pm = \theta_\pm \pm \frac{\omega_0}{c} s$$

$$\theta_\pm = \omega_\pm t + \varphi_\pm$$

$$\omega_0 = \frac{1}{2}\left(\dot{\theta}_+ + \dot{\theta}_-\right) = \frac{1}{2}\left(\omega_+ + \omega_-\right) = 2\pi m \frac{c}{L}$$

$$(2.4.1\text{-}7)$$

Here $\omega_\pm$ and $\varphi_\pm$ are the frequency and the initial phase of the two beams. Eqs.2.4.1-6 and 2.4.1-7 can now be used to calculate the various terms of Eq.2.4.1-5: we discard derivatives of $P_\pm$ and terms containing $\dot{E}_\pm$, $\ddot{E}_\pm$, $\ddot{\theta}_\pm$ as negligible by comparison with those containing $\dot{\theta}_\pm$ or $\dot{\theta}_\pm^2$ - to arrive at

$$\frac{\partial^2 E}{\partial s^2} = -\frac{\omega^2}{c^2} E$$

$$\frac{\partial E}{\partial t} = \frac{1}{2}\left[-i\dot{\theta}_+ E_+ e^{-i\phi_+} - i\dot{\theta}_- E_- e^{-i\phi_-}\right] + c.c.$$

$$\frac{\partial^2 E}{\partial t^2} = \frac{1}{2}\left[\left(-\dot{\theta}_+^2 E_+ - 2i\dot{\theta}_+ E_+\right) e^{-i\phi_+} + \left(-\dot{\theta}_-^2 E_- - 2i\dot{\theta}_- E_-\right) e^{-i\phi_-}\right] + c.c. \qquad (2.4.1\text{-}8)$$

$$\frac{\partial^2 E}{\partial t \partial s} = \frac{1}{2}\left[-\frac{\omega_0}{c}\dot{\theta}_+ E_+ e^{-i\phi_+} + \frac{\omega_0}{c}\dot{\theta}_- E_- e^{-i\phi_-}\right] + c.c.$$

$$\frac{\partial^2 P}{\partial t^2} = \frac{1}{2}\left[-\dot{\theta}_+^2 P_+ e^{-i\phi_+} - \dot{\theta}_-^2 P_- e^{-i\phi_-}\right] + c.c.$$

This, substituted back into Eq.2.4.1-5, produces - after equating the relevant terms - the two equations for the two beams:

$$-\omega_0^2 E_\pm + \dot{\theta}_\pm^2 E_\pm + 2i\dot{\theta}_\pm \dot{E}_\pm \mp \frac{4A\Omega}{L}\frac{\omega_0}{c}\dot{\theta}_\pm E_\pm + i\frac{\sigma}{\varepsilon_0}\dot{\theta}_\pm E_\pm = \frac{1}{\varepsilon_0}\dot{\theta}_\pm^2 P_\pm \qquad (2.4.1\text{-}9)$$

And hence, with the aid of the following approximations,

$$\omega_0 - \dot{\theta}_{\pm}$$

$$\dot{\theta}_{\pm}^2 \pm \frac{4A\Omega}{L}\frac{\omega_0}{c}\dot{\theta}_{\pm} - \left(\dot{\theta}_{\pm} \pm \frac{2A\Omega}{L}\frac{\omega_0}{c}\right)^2$$

the two sets of self-consistent equations:

$$\dot{E}_{\pm} \pm \frac{\sigma}{2\varepsilon_0}E_{\pm} = \frac{\omega_0}{2\varepsilon_0}\, \text{Im}\, P_{\pm} \qquad (2.4.1\text{-}10)$$

$$\dot{\theta}_{\pm} \pm \frac{2A\Omega}{L}\frac{\omega_0}{c} = \frac{\omega_0}{2\varepsilon_0}\frac{\text{Re}\, P_{\pm}}{E_{\pm}} \qquad (2.4.1\text{-}11)$$

The second of these yields the frequency difference between the two beams:

$$\Delta v = \frac{1}{2\pi}\left(\dot{\theta}_+ - \dot{\theta}_-\right) = \frac{4A\Omega}{\lambda L} + \frac{v_0}{2\varepsilon_0}\left(\frac{\text{Re}\, P_+}{E_+} - \frac{\text{Re}\, P_-}{E_-}\right) \qquad (2.4.1\text{-}12)$$

The first term on the right, $4A\Omega/\lambda L = S\Omega$, is the ideal gyroscope signal frequency encountered repeatedly in Ch.2.2; the second term is the nonlinear perturbation caused by polarisation of the medium. Indeed, the mutual beam coupling referred to at the beginning of this section arises through cross-polarisation. To see this explicitly - and to calculate its value - we must insert into Eq.2.4.1-12 the expression for polarisation (where mode pulling terms have been neglected):

$$P_{\pm} = \varepsilon_0 \chi\, E_{\pm} = \varepsilon_0(\chi' + i\chi'')E_{\pm} \qquad (2.4.1\text{-}13)$$

In the absence of backscattering, the two components of the perturbation term cancel out, $\Delta v = S\Omega$: there is no mode lock-in and the scale factor is a constant. In the presence of backscattering,

$$E_{\pm} \Rightarrow E_{\pm} + r_{\mp} E_{\mp}\, e^{\pm i(\psi + \varepsilon_{\mp})} \qquad (2.4.1\text{-}14)$$

$$\psi = \theta_+ - \theta_-$$

where $r_{\pm}$ and $\varepsilon_{\pm}$ are respectively the backscattering coefficient and angle. In other words, the field which gives rise to the polarisation contains two

38

components: the original wave and the backscattered wave combined in anti-phase. Combining the waves in-phase would give rise to a term in $\exp[-i(\theta_+ + \theta_-)]$ which averages to zero due to its rapid fluctuation: thus once again we see that in-phase scattering does not lead to lock-in.

Inserting Eq.2.4.1-14 into Eq.2.4.1-13 gives the real part of polarisation, $\text{Re}P_{\pm}$, as

$$
\begin{aligned}
\text{Re } P_{\pm} &= \varepsilon_0 \chi \left[E_{\pm} + r_{\mp} E_{\mp} e^{\pm i (\psi + \varepsilon_{\mp})} \right] \\
&= \varepsilon_0 \chi' \left[E_{\pm} + r_{\mp} E_{\mp} \cos (\psi + \varepsilon_{\mp}) \right] \mp \varepsilon_0 \chi'' r_{\mp} E_{\mp} \sin (\psi + \varepsilon_{\mp})
\end{aligned}
\qquad (2.4.1\text{-}15)
$$

The perturbation term in Eq.2.4.1-12 is then

$$
\begin{aligned}
\frac{\text{Re } P_+}{E_+} - \frac{\text{Re } P_-}{E_-} &= \varepsilon_0 \chi' \left[r_- \frac{E_-}{E_+} \cos (\psi + \varepsilon_-) - r_+ \frac{E_+}{E_-} \cos (\psi + \varepsilon_+) \right] \\
&\quad + \varepsilon_0 \chi'' \left[- r_- \frac{E_-}{E_+} \sin (\psi + \varepsilon_-) - r_+ \frac{E_+}{E_-} \sin (\psi + \varepsilon_+) \right]
\end{aligned}
\qquad (2.4.1\text{-}16)
$$

For equal scattering angles, $\varepsilon_+ = \varepsilon_-$, this reduces to

$$
\frac{\text{Re } P_+}{E_+} - \frac{\text{Re } P_-}{E_-} = \varepsilon_0 \chi' \left[r_- \frac{E_-}{E_+} - r_+ \frac{E_+}{E_-} \right] \cos (\psi + \varepsilon) - \varepsilon_0 \chi'' \left[r_- \frac{E_-}{E_+} + r_+ \frac{E_+}{E_-} \right] \sin (\psi + \varepsilon)
$$

$$(2.4.1\text{-}17a)$$

If the intensities and backscattering coefficients are also equal, it is further simplified to

$$
\frac{\text{Re } P_+}{E_+} - \frac{\text{Re } P_-}{E_-} = - 2\varepsilon_0 \chi'' r \sin (\psi + \varepsilon)
\qquad (2.4.1\text{-}17b)
$$

Inserted into the frequency equation Eq.2.4.1-12, this yields

$$
\Delta \nu = \frac{1}{2\pi} \dot{\psi} = \frac{4A}{\lambda L} \Omega - \nu_0 \chi'' r \sin (\psi + \varepsilon)
\qquad (2.4.1\text{-}18)
$$

which can be written more conveniently as

$$\dot{\psi} = S_0\left[\Omega^* - \Omega^*_L \sin(\psi+\varepsilon)\right] = S_0\Omega^*\left[1 - K \sin(\psi+\varepsilon)\right] \qquad (2.4.1-19)$$

with $\qquad S_0 = 4A/\lambda L$, $\qquad \Omega_L = v_0\chi''r/S_0$, $\qquad K = \Omega_L/\Omega$

and $\qquad\qquad \Omega^* = 2\pi\Omega$, $\qquad\qquad \Omega_L^* = 2\pi\Omega_L$

Eq.2.4.1-19 is the lock-in equation, with the lock-in threshold at $\Omega_L = v_0\chi''r$.
Fig.2.4-2 shows time evolution of the function $\dot{\psi}$ for various values of the parameter K.

For rates of rotation above threshold (K<1), the solution of Eq.2.4.1-19 is

$$\tan\left(\frac{\psi+\varepsilon}{2}\right) = K + C \tan\left(\frac{Xt}{2}\right)$$

$$\psi = 2\tan^{-1}\left[K + C \tan\left(\frac{Xt}{2}\right)\right] - \varepsilon \qquad (2.4.1-20)$$

$$C = (1-K^2)^{1/2} , \qquad X = S_0\Omega^*C$$

For high rates of rotation (K<<1, C≈1), Eq.2.4.1-20 reverts to the linear relationship

$$\psi + \varepsilon = S_0\Omega^*t \qquad \text{and} \qquad \dot{\psi} = S_0\Omega^* \qquad (2.4.1-21)$$

For lower rates of rotation, ψ is periodic with period 1/X. The combined beam intensity (the "heterodyne" signal, or fringe patern) fluctuates as $\sin\psi$ (Fig.2.4-3) which has the same period as $\dot{\psi}$. The observed frequency is therefore

$$f = \frac{1}{2\pi}X = S_0\Omega\sqrt{1-K^2} = S_0\left[\Omega^2 - \Omega_L^2\right]^{\frac{1}{2}} \qquad (2.4.1-22)$$

Fig.2.4-3 shows the combined beam intensity versus time for several values of the lock-in parameter K: note both the slowing-down and the distortion of the sinusoidal shape at low rates of rotation. Fig.2.4-4 plots the observed frequency as a function of rotation rate.

a

b
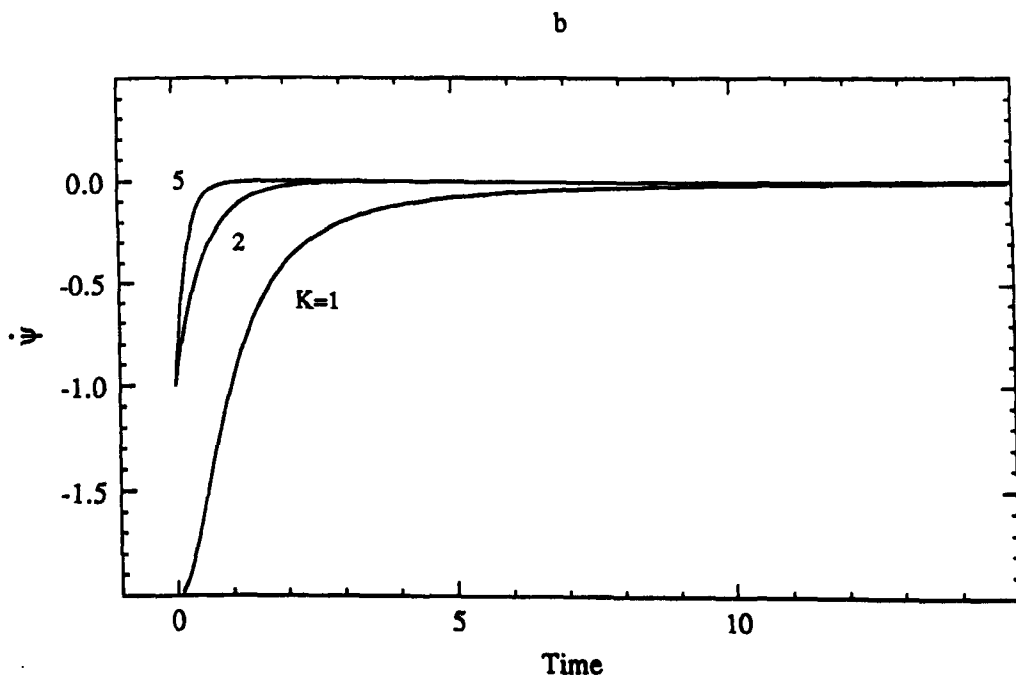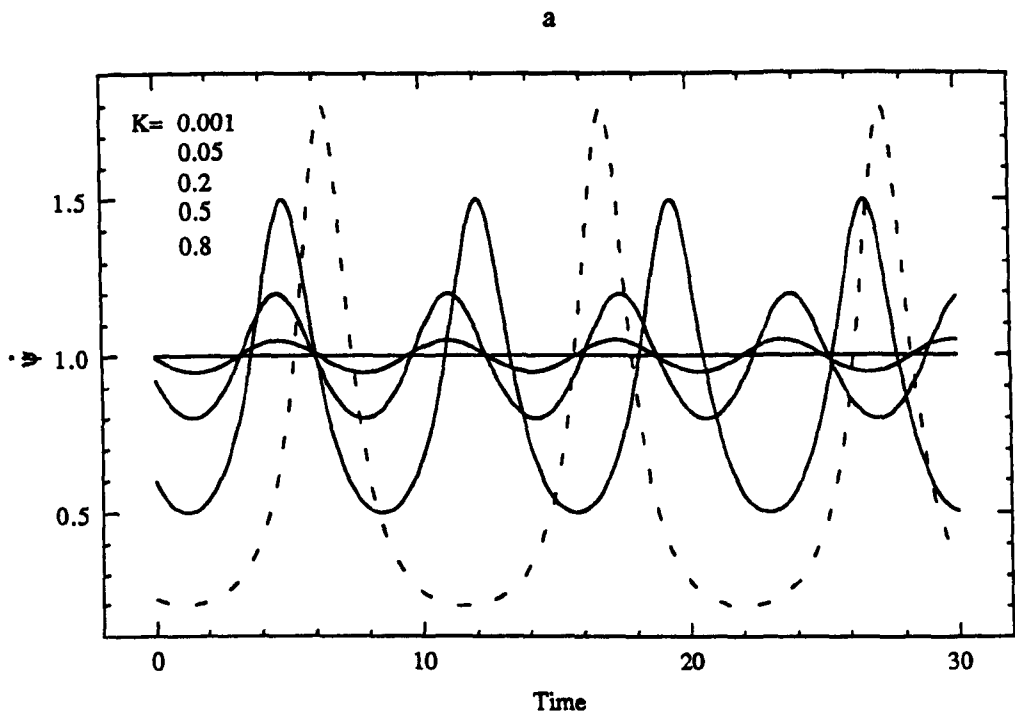
Fig.2.4-2 Time evolution of the function $\dot{\psi}$ for various values of the parameter K:

a) K= 0.001, 0.05, 0.2, 0.5, 0.8 in order of increasing amplitude; b) K= 1, 2, 5.

41

K=0.001

K=0.5

K=0.8
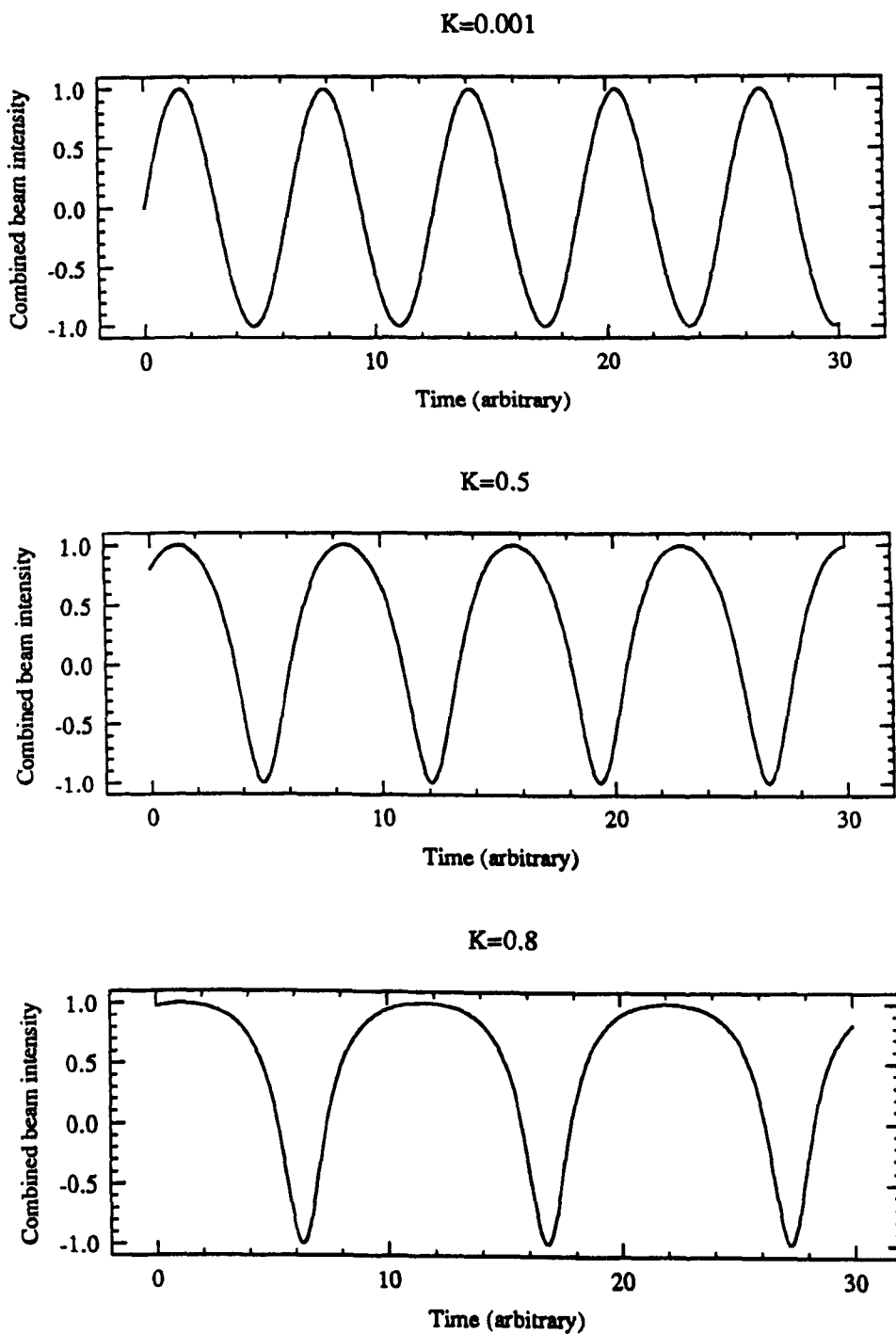
Fig.2.4-3 The combined beam intensity versus time for various values of K.
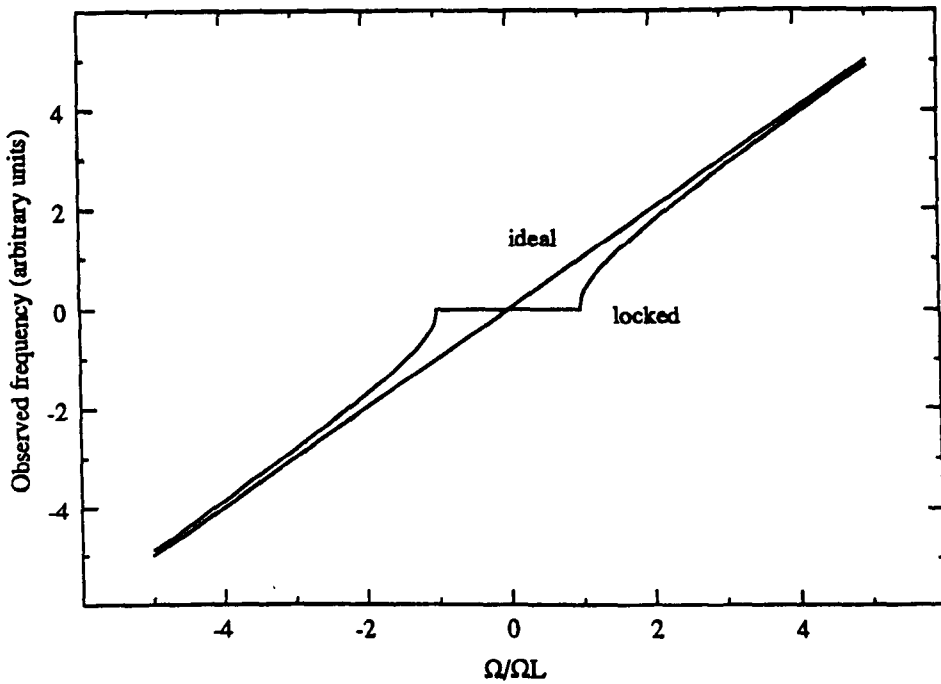
Fig.2.4-4 The observed frequency versus rotation rate.

At threshold $(K+1, C=0)$, ψ becomes a constant:

$$\psi = 2\tan^{-1}1 - \varepsilon = \pi/2 - \varepsilon \quad \text{or} \quad 3\pi/2 - \varepsilon \qquad \text{and} \qquad \dot{\psi} = 0$$

The frequency difference is zero: the gyroscope is locked.

Below threshold $(K>1)$, the solution of the lock-in equation is*

$$\tan\left(\frac{\psi+\varepsilon}{2}\right) = K + C\frac{1+e^{Xt}}{1-e^{Xt}}$$

$$\psi = 2\tan^{-1}\left[K + C\frac{1+e^{Xt}}{1-e^{Xt}}\right] - \varepsilon \qquad (2.4.1\text{-}23)$$

$$C = (K^2-1)^{1/2}$$

---

* This solution can be derived from Eq.2.4.1-20 by expressing $(1-K^2)^{1/2}$ as a complex number.

This solution evolves to a constant on the time scale $1/X$ (see Fig.2.4-2b):

$$\psi \,(t >> 1/X) \;=\; 2\tan^{-1}(K - C) - \varepsilon \;=\; \sin^{-1}\!\left(\frac{1}{K}\right) - \varepsilon \quad * \qquad (2.4.1\text{-}24)$$

The threshold value $(K=1, C=0)$ is again

$$\psi \;=\; 2\tan^{-1}1 - \varepsilon \;=\; \pi/2 - \varepsilon \quad\text{or}\quad 3\pi/2 - \varepsilon$$

At threshold, the solution of Eq.2.4.1-19 is (see Fig.2.4-2b)

$$\tan\!\left(\frac{\psi + \varepsilon}{2}\right) \;=\; \frac{\Omega_L{}^* t - 1}{\Omega_L{}^* t + 1}$$

$$\psi \;=\; 2\tan^{-1}\!\left[\frac{\Omega_L{}^* t - 1}{\Omega_L{}^* t + 1}\right] - \varepsilon \qquad (2.4.1\text{-}25)$$

which again evolves to a constant, although this time linearly rather than exponentially. The asymptotic value is once again

$$\psi \;=\; 2\tan^{-1}1 - \varepsilon \;=\; \pi/2 - \varepsilon \quad\text{or}\quad 3\pi/2 - \varepsilon$$

---

* The last equality is easily derived from the triangle:

$$\beta = \sin^{-1}(1/K)$$

$$\frac{K - (K^2 - 1)^{1/2}}{\sin(\beta/2)} \;=\; \frac{1}{\sin(\pi/2 + \beta/2)} \;=\; \frac{1}{\cos(\beta/2)}$$
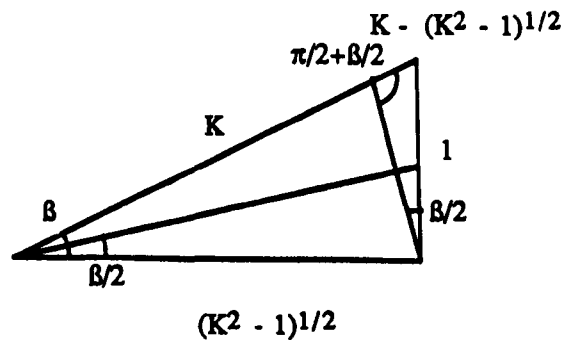
$$\beta/2 = \tan^{-1}\!\left[K - (K^2 - 1)^{1/2}\right]$$

A rough estimate of the lock-in threshold is easily arrived at. First[32],

$$\chi'' \approx \frac{1}{2\pi} \lambda G \qquad (2.4.1\text{-}26)$$

where G is the exponential gain. Therefore,

$$\nu_0 \chi'' \approx \frac{1}{2\pi} cG \qquad (2.4.1\text{-}27)$$

and

$$S_0 \Omega_L \approx \frac{1}{2\pi} cGr \qquad (2.4.1\text{-}28)$$

For a typical He-Ne ring laser operating at $0.6328\mu m$, the gain[26] is of the order of $0.1m^{-1}$, the backscattering at the mirrors[30] of the order of 10^{-4} and the scale factor of the order of 10^5 counts/rad: with the result that

$$S_0 \Omega_L \approx 1kHz$$

The threshold rotation rate is

$$\Omega_L \approx 10^{-2} rad/s \approx 10^3 deg/hr$$

2.4.2 Perturbation theory of mode coupling

We have seen in Sec.2.4.1 that anti-phase scattering gives rise to lock-in, while the in-phase type does not. However, when second-order effects are taken into account, in-phase scattering is nevertheless seen to cause nonlinear errors in the scale factor.

In order to derive this relationship, the self-consistent equations are written in terms of wave intensities, taking into account the small difference in the intensities of the two counter-propagating waves.[31] This yields a system of four coupled differential equations, for $I = I_+ + I_-$, $i = I_+ - I_-$, $\psi = \theta_+ - \theta_-$ and $\zeta = \theta_+ + \theta_-$:

$$\dot{I} = -\alpha I - S_0\Omega^*_{L-}\sin\psi - iS_0\Omega^*_{L+}\sin\psi \qquad (2.4.2\text{-}1)$$

$$\dot{i} = -\beta i - S_0\Omega^*_{L+}\sin\psi - iS_0\Omega^*_{L-}\sin\psi$$

$$\dot{\psi} = S_0\Omega^* - S_0\Omega^*_{L-}\sin\psi + iS_0\Omega^*_{L+}\sin\psi$$

$$\dot{\zeta} = -S_0\Omega^*_{L+}\sin\psi + iS_0\Omega^*_{L-}\sin\psi$$

with

$\alpha = 2 \times$ (unsaturated gain - cavity losses) $= 2 \times$ net unsaturated gain

$\beta = \alpha \times$ (self-saturation - cross-saturation) / (self-saturation + cross-saturation)

and "+" and "-" denoting respectively in-phase and anti-phase

To solve these equations two assumptions are necessary: first, that in-phase scattering is a small perturbation, i.e. $\Omega^*_{L-} \gg i\Omega^*_{L+}$; and secondly, that the system is far from threshold, i.e. the signal is an undistorted sine, $\psi = S_0\Omega^* t$. Given these assumptions, the second equation becomes

$$\dot{i} = -\beta i - iS_0\Omega^*_{L-}\sin(S\Omega^* t) \qquad (2.4.2\text{-}2)$$

the solution of which is

$$i = -\frac{S_0\Omega^*_{L+}}{\sqrt{S_0^2\Omega^{*2} + \beta^2}} \sin\left[S_0\Omega^* t - \tan^{-1}\left(\frac{S_0\Omega^*}{\beta}\right)\right] \qquad (2.4.2\text{-}3)$$

Inserted into the equation for $\dot{\psi}$, this gives

$$\dot{\psi} \cong S_0\Omega^* - S_0\Omega^*_{L-}\sin\psi + \frac{\frac{1}{2}S_0^2\Omega^{*2}_{L+}}{S_0^2\Omega^{*2} + \beta^2}\Omega \qquad (2.4.2\text{-}4)$$

The resulting output frequency is a function with a positive scale factor correction (Fig.2.4-5):

$$f = S_0\left[\Omega^2\left(1 + \frac{1}{2}\frac{S_0^2\Omega^{*2}_{L+}}{S_0^2\Omega^{*2} + \beta^2}\right)^2 - \Omega_L^2\right]^{1/2} \qquad (2.4.2\text{-}5)$$

46

This correction was measured in one particular gyroscope by Aronowitz and Lim[5] and its maximum, depending on the laser power, was found to be between 0.3% and 0.003% of the nominal scale factor.

Nonetheless, in a different system, possessing a large coupling constant, the positive correction may be much larger. It must be stressed, however, that in these circumstances Eq.2.4.2-5 can no longer be expected to hold true, due to the limiting assumptions made in its derivation.

One possible agent of such increased positive correction may be the burning of grating across the mirrors. This can occur whenever a gyroscope is allowed to operate in the locked condition for a prolonged period of time: the stationary standing wave in the resonator may then burn a grating within the nonlinear material of the dielectric mirrors. Depending on whether the grating is refractive of absorbing, it will give rise either to in-phase or anti-phase coupling, which in turn will lead to either increased lock-in threshold or enhanced positive correction - or possibly both.
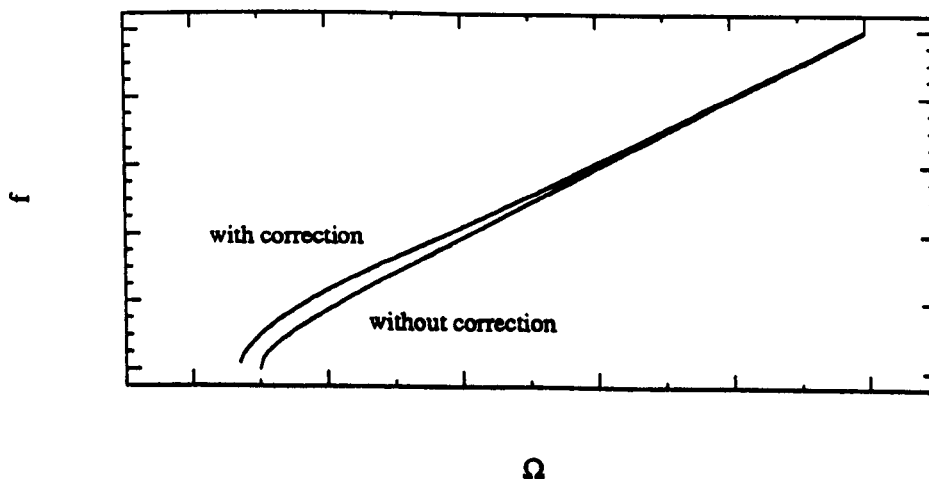

Fig.2.4-5 The output signal frequency with and without the positive correction.

2.4.3 Lock-in reduction methods

Traditionally, all lock-in reduction methods have been based, in one way or another, on biasing the gyroscope so as to shift the output away from the locked region.

The simplest and most obvious way of doing so is to add a constant rotation rate much larger than the nonlinear region; the bias can then be subtracted from the output to obtain the correct reading. This can be achieved, for example, by inserting a Faraday rotator into the resonator: a Faraday rotator causes a non-reciprocal phase shift equal and opposite for the two beams which is equivalent to a frequency shift. The main problem with this approach is the high accuracy and stability required of the bias. Since the rate of rotation to be measured may vary over six orders of magnitude, the bias must be constant and known to 10^{-7}. Also, the bias must exceed the lock-in threshold Ω_L by a factor of at least 10^2 to escape nonlinearity. Moreover, the method places an upper limit on the rate of rotation one may measure, since it shifts the locked region from zero to $-\Omega_{bias}$.

Dither

To avoid these problems, many existing systems use alternating bias[4,9,31]. Indeed, alternating mechanical bias - dithering - has proved to be the most successful scheme to date: accuracies of 10^{-3}deg/hr have been achieved. The method employs a gyroscope mounted on a spring which rotates it sinusoidally back and forth. The lock-in equation in this case is

$$\Delta v = S\Omega - \Omega_L\sin(\psi + \varepsilon) + \Omega_B\sin(\omega_B t) \qquad (2.4.3-1)$$

where Ω_B is the magnitude of the bias and ω_B the dither rate. Eq.2.4.3-1 cannot
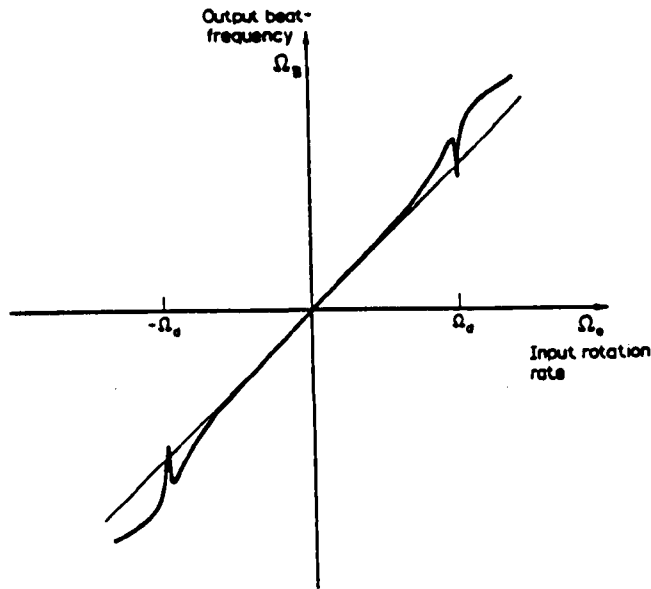
Fig.2.4-6 Numerical solution of the frequency equation for a dithered gyroscope.

be solved analytically: Fig.2.4-6 quotes a numerical solution[31]. In practical devices the sharp spikes are eliminated by introducing random noise into the system; there remains however a slight residual nonlinearity in the vicinity of Ω_B. In addition, the method suffers from loss of information as the system passes through the locked band. Increasing bias reduces the dead-time and also shifts the nonlinearity away from the low rotation region where higher accuracy is usually required. Despite its difficulties, however, the scheme has been most successful and is widely applied commercially.

The DILAG

A variation on the constant bias approach is the DILAG - differential laser gyroscope (see Statz *et al.*[28] for a comprehensive review). This scheme uses both reciprocal and non-reciprocal frequency splitting to create four modes which escape locking due to large effective bias. First, both beams are split into left- and right-circularly polarised modes (reciprocal splitting): this is achieved

49

Fig.2.4-7 Mode structure of differential laser gyroscope.

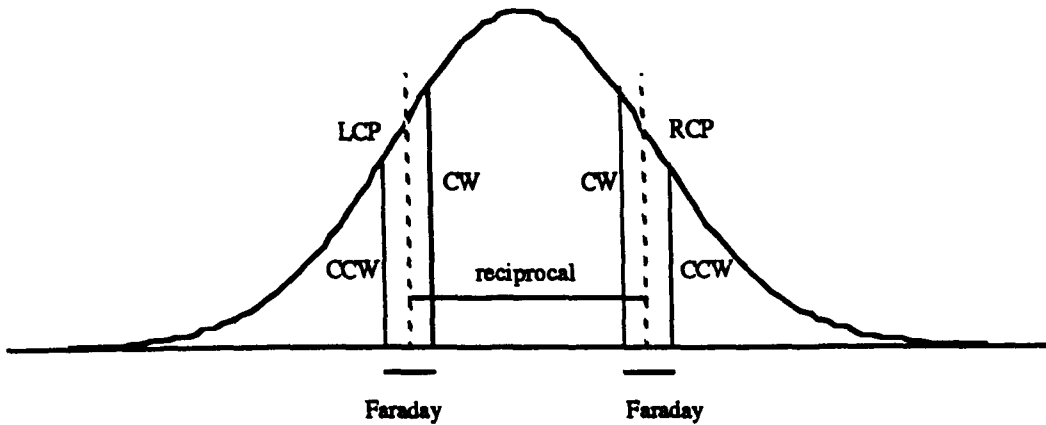either by a birefrigent crystal (e.g. quartz) in the cavity, or by a four-mirror non-planar resonator. Then the two pairs of modes are further separated by introducing non-reciprocal Faraday shift: this can be done either by a magnetic mirror (Faraday effect) or by a magnetic field applied to the laser medium (Zeeman effect - the ZLAG scheme). Fig.2.4-7 shows the resulting mode structure.

The four modes in effect constitute two independent gyroscopes comprised of RCP and LCP modes. The frequency differences in this case are

$$\nu_{CCW}^{RCP} - \nu_{CW}^{RCP} = S\Omega + \Delta\nu_F$$
$$\nu_{CCW}^{LCP} - \nu_{CW}^{LCP} = S\Omega - \Delta\nu_F$$

(2.4.3-2)

The measured beat frequency, observed by combining the two signals, is

$$\Delta\nu = 2S\Omega$$

(2.4.3-3)

This is linear, bias-independent, and free of lock-in due to the wide frequency separation of the modes. The chief drawback of this method is that all four versions of it require elements in the cavity which interfere in various ways with the gain medium and/or beam propagation and thus give rise to scale factor errors. Nonetheless, much work on this system has been reported (e.g. Refs. 17, 28), including a patent application[24].

50

The two-mode gyroscope

A completely different approach was adopted in papers by Sanders et al.[21], Scully et al.[23] and Anderson et al.[2,3] In this scheme, the laser is pumped sufficiently hard for an additional mode to become excited. The two modes may be a longitudinal and a transverse one or two longitudinal ones. In these circumstances - that is, with two modes oscillating simultaneously - the lock-in threshold was observed to diminish considerably, or indeed to disappear altogether. Fig.2.4-8a,b quotes the results.

In order to explain this effect the authors developed a theory of the two-mode ring laser. In this they assumed that the second mode had only a fraction of the intensity of the main one, and therefore could be treated as a perturbation. The resulting lock-in equation was similar in form to the dither equation Eq.2.4.3-1, with the dither frequency equal to the frequency difference of the two modes. The conclusion was that a weak additional mode is equivalent in its effect to a variable bias.

However, in addition to possessing considerable nonlinearity, the calculated beat frequency differed significantly from the observed one (see Fig.2.4-8b). Moreover, the proposed explanation applied only to a second mode weak enough to be regarded as a perturbation, while there were no experimental grounds for assuming this to be the case. For these reasons the theoretical treatment of this phenomenon met with some criticism[9], and the work seems to have been discontinued.

Nevertheless, there can be no doubt that if this method can be substantiated and developed, it will have great advantages over other techniques of biasing, the most obvious of which are its simplicity and the absence of moving parts and additional optical elements. Accordingly, Sec.2.5 will be devoted to a theoretical discussion of this proposal.

a

b
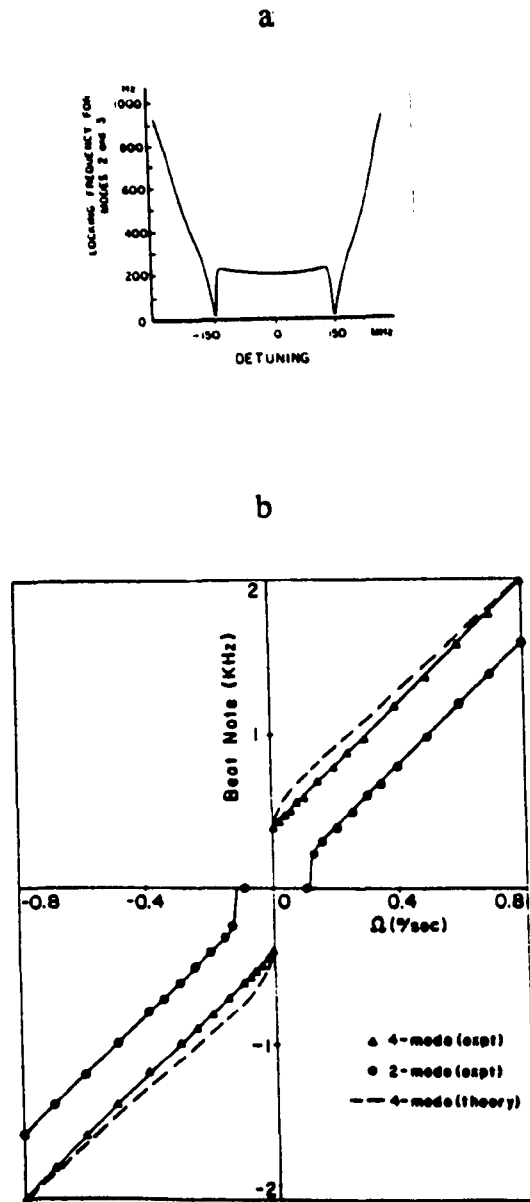
Fig.2.4-8 Lock-in reduction in a two-mode gyroscope: a) Ref.23; b)Ref.3

2.5 THE TWO-MODE RING LASER GYROSCOPE

2.5.1 The lock-in equation for two modes

In this section we wish to derive the lock-in equation for the two-mode ring laser gyroscope proposed in Sec.2.4.2, that is for a ring laser in which two pairs of modes oscillate simultaneously. Fig.2.5-1 shows the mode structure.

Fig.2.5-1 Mode structure of a two-mode ring laser.

We begin with the frequency difference equation Eq.2.4.1-12:

$$\Delta v = S_0 \Omega + \frac{v_0}{2\varepsilon_0} \left(\frac{Re\ P_+}{E_+} - \frac{Re\ P_-}{E_-} \right)$$

As in Sec.2.4.1, we substitute into it the expression for polarisation $P = \varepsilon_0 \chi E$.

However, because two pairs of modes are oscillating, $E_\pm$ is in this case

53

$$E_\pm \Rightarrow E_{1\pm} + r_{1\mp}E_{1\mp} \exp\left[\pm i \left(\psi_1 + \varepsilon_{1\mp}\right)\right] + E_{2\pm}\exp\left[i\psi_2\right] + r_{2\mp}E_{2\mp}\exp\left[i \left(\psi_2 \pm \psi_1 \pm \varepsilon_{2\mp}\right)\right]$$

(2.5.1-1)

where the indices refer to the two pairs of modes, and

$$\psi_1 = \phi_{1+} - \phi_{1-}$$
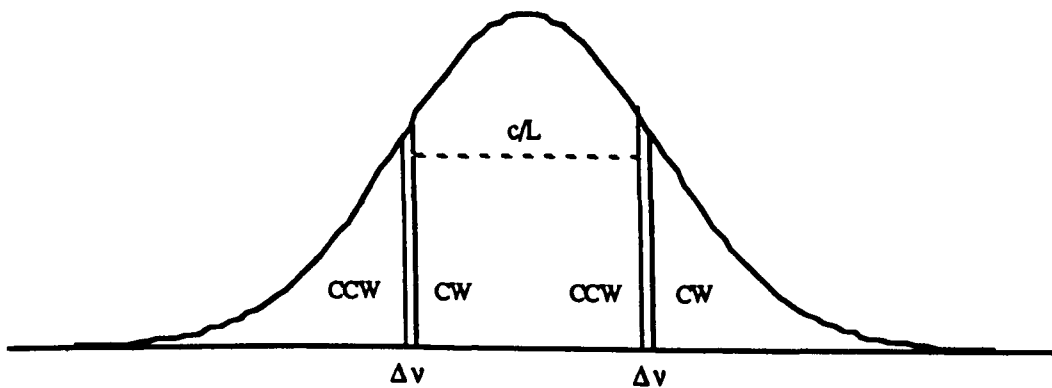
(2.5.1.2)

$$\psi_2 = \phi_{1+} - \phi_{2+} = \phi_{1-} - \phi_{2-}$$

For $\varepsilon_{1\pm}=\varepsilon_{2\pm}$, $E_{1\pm}=E_1$, $E_{2\pm}=E_2$, $r_{1\pm}=r_1$, $r_{2\pm}=r_2$ - not an unreasonable assumption, since in the absence of non-reciprocal losses the intensities of the two modes within each pair are expected to be equal, and scattering angles are in any case intensity-independent - $\mathrm{Re}P_\pm$ becomes

$$\mathrm{Re}\,P_\pm = \varepsilon_0\chi'\left[E_1 + r_1E_1\cos\left(\psi_1+\varepsilon\right) + E_2\cos\psi_2 + r_2E_2\cos\left(\psi_2\pm\psi_1\pm\varepsilon\right)\right]$$
$$- \varepsilon_0\chi''\left[\mp r_1E_1\sin\left(\psi_1+\varepsilon\right) - E_2\sin\psi_2 - r_2E_2\sin\left(\psi_2\pm\psi_1\pm\varepsilon\right)\right]$$

(2.5.1-3)

which simplifies to

$$\frac{\mathrm{Re}\,P_+}{E_+} - \frac{\mathrm{Re}\,P_-}{E_-} = -2\varepsilon_0\left[\chi'r_2\frac{E_2}{E_1}\sin\psi_2 + \chi''r_1 + \chi''r_2\frac{E_2}{E_1}\cos\psi_2\right]\sin\left(\psi_1+\varepsilon\right)$$
(2.5.1-4)

The lock-in equation (compare Eq. 2.4.1-19) is now *

$$2\pi\Delta v = \dot{\psi}_1 = S_0\left\{\Omega^* - \Omega_L^*\sin\left(\psi_1+\varepsilon\right)\left[1 + \frac{r_2E_2}{r_1E_1}\left(\frac{\chi'}{\chi''}\sin\psi_2 + \cos\psi_2\right)\right]\right\}$$

$$\Omega_L = v_0\chi''r_1$$

(2.5.1-5)

This is the lock-in equation for a two-mode ring laser.

---

* A similar equation can be written for the second pair of modes, with ψ_3 replacing ψ_1 and a negative ψ_2.

2.5.2 Discussion of terms

The perturbation term in Eq.2.5.1-5 is a product of two factors: the first, $v_0 \chi'' r_1 \sin(\psi_1 + \varepsilon)$, is similar to that appearing in the two-mode case (Eq.2.4.1-19); the second,

$$\left[1 + \frac{r_2 E_2}{r_1 E_1} \left(\frac{\chi'}{\chi''} \sin \psi_2 + \cos \psi_2 \right) \right]$$

is the contribution of the additional pair of modes (indeed, it reduces to 1 for $r_2 E_2 \ll r_1 E_1$). Let us now examine this term. To begin with, note that

$$\rho = \frac{\chi'}{\chi''} \cong \frac{2(v - v_d)}{\Delta v_D} \qquad (2.5.2-1)$$

This factor for a typical gyroscope can be $0.1 \leq \rho \leq 0.5$.

Secondly, to maximise the effect - and for the sake of simplicity - we assume $r_2 E_2 / r_1 E_1 = 1$.

Finally, we may neglect ε as having no bearing on the character of the solution.

The lock-in equation then becomes

$$\dot{\psi}_1 = S_0 \Omega^* \left\{ 1 - K \sin \psi_1 \left[1 + \left(\rho \sin \psi_2 + \cos \psi_2 \right) \right] \right\} \qquad (2.5.2-2)$$

$$K = \Omega_L / \Omega$$

It must be remembered that while ψ_1 is similar to ψ of Ch.2.4, ψ_2 represents the phase difference between modes belonging to different pairs; therefore the expression in round brackets has the period of $\sim 10^{-8}$s.

The result is a rapid fluctuation of the lock-in term: the effective threshold oscillates between a high and a low value. Since the system requires time of the order 10^{-3}s to become locked (see Sec.2.4.1), which is much longer than the

oscillation period, such threshold fluctuations may suppress locking.

Conversely, it may be argued that on the time scale of ψ_1 the oscillating term averages to zero and therefore can have no influence on the overall solution. However, this interpretation disregards the fact that the fluctuation of the effective lock-in term swings the solution between two qualitatively different regimes (Fig.2.4-2) while necessarily preserving phase continuity at each transition.

Perhaps the situation is best illustrated by a phase-vector diagram (Fig.2.5-2). Here the second pair of modes adds a rapidly whirling component to each of the main vectors. The resultant is now no longer a function of solely the phase difference ψ_1 but also of inter-mode separation ψ_2. Thus the absolute mutual dependence of the two resultant vectors - the source of lock-in - is diminished.
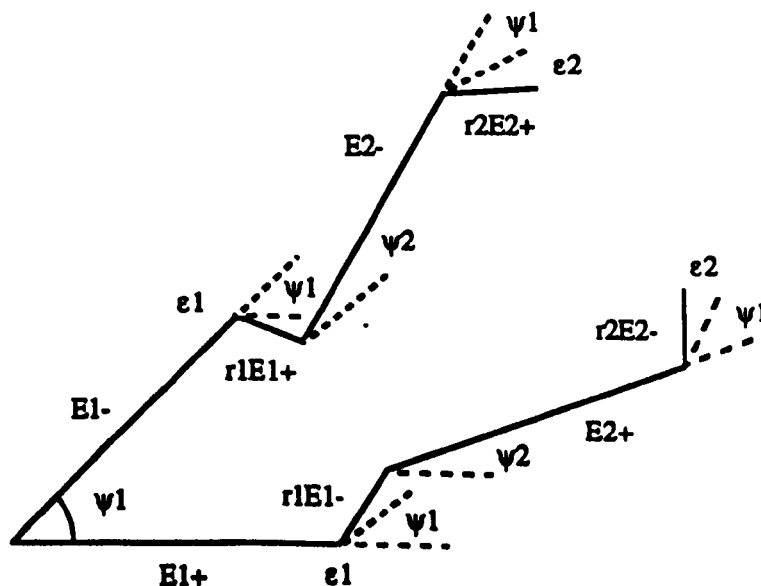

Fig.2.5-2 A phase-vector diagram of the two-mode ring laser.

2.5.3 The solution

Eq.2.5.2-2 cannot be solved analytically due to its strong nonlinearity. However, it is possible to consider the general character of the solution without obtaining it explicitly.

It must be borne in mind that the two-mode lock-in equation Eq.2.5.2-2 is exactly equivalent to the one-mode Eq.2.4.1-19 with the added complication of a rapidly fluctuating threshold; the threshold oscillation is at least five orders of magnitude faster than the variation of the basic function ψ_1. Accordingly, we are interested in a time-averaged solution*.

If a solution exists such that $\dot{\psi}_1$ is periodic then

$$\dot{\psi}_1(t) = \dot{\psi}_1(t+T) \qquad (2.5.3-1)$$

and
$$\psi_1(t) = \psi_1(t+T) - A \qquad (2.5.3-2)$$

for some constant A. The time-averaged solution over N periods is

$$\Psi(t) = \frac{1}{NT} \int_t^{t+NT} \psi_1(u)\, du \qquad (2.5.3-3)$$

It follows from Eqs.2.5.3-2 &3 that**

$$\dot{\Psi}(t) = \frac{A}{T} \qquad (2.5.3-4)$$

and
$$\Psi(t) = B + \frac{A}{T} t \qquad (2.5.3-5)$$

In other words, provided that $A \neq 0$, $\Psi(t)$ is linear in time. Conversely, if $A=0$,

---

*   I am indebted for this solution to Dr. R.A. Bousfield and Dr. J.C. Newby of the Department of Mathematics.

** For proofs of this and and other mathematical statements see Appendix.

then the solution describes a locked gyroscope; since we do not know A we cannot discount this possibility.

Substituting Eq.2.5.3-2 into Eq.2.5.2.-2 gives the conditions that the constants A and T must satisfy:

$\sin \psi_1(t+T) [1 + (\rho \sin \psi_2(t+T) + \cos \psi_2(t+T))] = \sin \psi_1(t) [1 + (\rho \sin \psi_2(t) + \cos \psi_2(t))]$

The equality holds if

$$T = 2m\pi/\Delta v_2 \qquad\qquad (2.5.3\text{-}6)$$

and $\qquad\qquad A = 2n\pi$

where m and n are integers (including zero) and Δv_2 is the frequency difference between the two pairs of modes. Solutions having different n's may intersect, therefore the solution is not unique.

The above derivation does not provide an explicit time-averaged solution of the lock-in equation, nor does it specify how the proportionality coefficient A/T may be related to the system parameters $S_0\Omega$ and Ω_L, nor guarantee that A≠0. In fact, it tells us only that if A≠0 and if one solution can be found which will satisfy Eq.2.5.3-1, then all time-averaged periodic solutions will be linear in time and therefore unlocked.

We wish therefore to find one periodic solution. We can do so by solving Eq.2.5.2-2 numerically using the Runge-Kutta method. Fig.A-1 of Appendix shows two examples above and below threshold: these are periodic. However, the time-averaged solution below threshold is locked, implying that in this case indeed A=0. On the other hand, since the fluctuating threshold causes the physical system to alternate between the two different forms shown in Figs. 2.4-2a (K<1) and 2.4-2b (K>1), a numerical solution cannot really be expected to follow this behaviour.

Chapter 3

EXPERIMENTAL SETUP

3.1 SYSTEM DESCRIPTION

3.1.1 The scale factor

The two ring lasers used in the present experiment both had three-mirror rings, with the mirrors placed at the vertices of an equilateral triangle (this is indeed the most popular configuration). The equilateral shape maximises the area/perimeter ratio and therefore the scale factor.

For such ring lasers, the scale factor is given by

$$S_0 = 4A/\lambda L = (1/\lambda)L/3^{3/2} = 0.304 \cdot 10^6 \cdot L \text{ counts/rad} = 5.31 \cdot 10^3 \cdot L \text{ counts/deg}$$

$$(3.1.1-1)$$

where the resonator perimeter L is in metres and $\lambda \approx 0.6328\mu m$. In terms of frequency,

$$S_0 = 0.304 \cdot L \text{ MHz/(rad/s)} = 5.31 \cdot L \text{ kHz/(deg/s)} = 1.47 \cdot L \text{ Hz/(deg/hr)} \qquad (3.1.1-2)$$

It ought to be remembered, in particular with respect to the modular gyroscope, that a triangular resonator which slightly departs from the equilateral shape, having sides

$$A = (L/3)(1+a)$$
$$B = (L/3)(1+b) \qquad (a+b+c) = 0$$
$$C = (L/3)(1+c)$$

will have a reduced scale factor of

$$S'_0 = S_0[1 + 2(ab+bc+ac)] = S_0[1 + 2(ab-c^2)] \qquad (3.1.1-3)$$

The relative error S'_0/S_0 is proportional to the square of displacement: e.g, for a shift of (10%, -10%, 0) the reduction is 2%.

3.1.2 Mode structure

For a three-mirror equilateral-triangle ring resonator, the mode structure equation Eq.2.3.3-2 resolves into

$$\nu_{qnm} = \frac{c}{2L}\left[2q + \frac{1}{\pi}\left(n + \frac{1}{2}\right)\cos^{-1}\left(1 - \frac{2L}{\sqrt{3}R}\right) + \varepsilon + \frac{1}{\pi}\left(m + \frac{1}{2}\right)\cos^{-1}\left(1 - \frac{\sqrt{3}L}{2R}\right)\right] \quad (3.1.2\text{-}1)$$

The various frequency differences between longitudinal and transverse modes are then as follows:

$$\begin{array}{cccl} \Delta q & \Delta n & \Delta m & \Delta \nu \\ \\ 1 & 0 & 0 & \dfrac{c}{L} \\ \\ 0 & 1 & 0 & \dfrac{c}{2L}\left[1 + \dfrac{1}{\pi}\cos^{-1}\left(1 - \dfrac{2L}{\sqrt{3}R}\right)\right] \\ \\ 0 & 0 & 1 & \dfrac{c}{2L}\left[\dfrac{1}{\pi}\cos^{-1}\left(1 - \dfrac{\sqrt{3}L}{2R}\right)\right] \end{array} \qquad (3.1.2\text{-}2)$$

The beam dimensions (for R and L in metres) are:

at waist $\quad w_{0\pm} = (\lambda/2\pi)^{1/2} R^{1/2} g_{\pm} = 0.317 \, R^{1/2} \, g_{\pm}$ mm

at the curved mirror $\quad w_{\pm} = (\lambda/2\pi)^{1/2} L^{1/2} g_{\pm} = 0.317 \, L^{1/2} \, g_{\pm}$ mm

where $\quad g_{\pm} = [\gamma_{\pm} L/R (1 - \gamma_{\pm} L/R)]^{-1/4}$ and $\gamma_{+} = \sqrt{3}/2$; $\gamma_{-} = 2/\sqrt{3}$

$$(3.1.2\text{-}3)$$

The dimensions of the TEM_{01} and TEM_{10} modes are greater by a factor of ≈ 1.5. Higher modes do not appear as their diffraction losses surpass gain. (The aperture of a He-Ne laser must exceed beam spot size by a factor of at least 3 to support oscillation.)

61

3.1.3 The combining prism

In order to obtain a detectable fringe pattern, the two output beams of the ring laser must be combined together. On leaving the partially transmitting mirror, the beams diverge by 60° and are ~3mm apart. They are brought together and closely aligned by a special double 90° corner prism, the combining prism of the gyroscope, which is shown below.
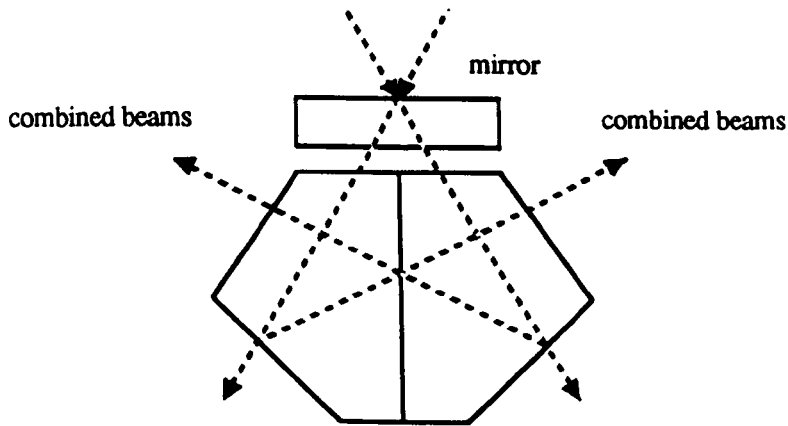

Fig.3.1-1 The gyroscope combining prism.

If alignment is correct the fringes are clearly visible. For equal beam intensities, the fringe pattern is given by[9]

$$I = I_0\left[1 + \cos\left(2\pi\frac{\alpha d}{\lambda} + 2\pi\,\Delta\nu\,t + \varphi\right)\right] \qquad (3.1.3-1)$$

where α is the angular divergence of the beams (zero for perfect alignment), d is measured along the surface of the detector, and φ is a constant phase shift. The fringe spacing is then $d=\lambda/\alpha$: for an output signal to be observed, this must be larger than the sensitive area of the photodetector. In the present experiment, this implies a divergence angle of $\alpha\leq130"$.

The $2\pi\Delta v$ term is responsible for the movement of fringes arising from rotation; the direction of movement depends, through the sign of Δv, on the sense of rotation. A counter may be attached through a suitable circuit to the photodetector, which will count the fringes moving past it, giving a total count of

$$N_{total} = \int_0^T |\Delta v|\, dt \qquad (3.1.3-2)$$

This, in fact, has been done in the present experiment. Two counters can be used in conjunction with a logic circuit to sense the direction of movement, adding up the counts in each direction. The system will then calculate the instantaneous cumulative angle of rotation Θ:

$$N(T) = \int_0^T \Delta v\, dt = \frac{4A}{\lambda L} \int_0^T \dot{\Omega}\, dt = \frac{4A\Theta}{\lambda L} \qquad (3.1.3-3)$$

In order to be able to measure all three angles of rotation simultaneously, commercial gyroscopes incorporate three ring lasers lying in three mutually orthogonal planes.

Although the alignment of the combining prism has to be very precise, in practice it is not at all difficult to achieve.

Finally, some specifications of the photodiode used in the experiment are worth quoting:

Type:	BPX 65
Sensitive area:	$1 mm^2$
Responsivity at 850 nm:	0.55A/W
Cut-off frequency ($R_L = 50\Omega$):	500MHz

3.1.4 The Fabry-Perot spectrum analyser

The mode structure of the ring lasers in the experiment was monitored by a spherical mirror Fabry-Perot optical spectrum analyser. In principle this is similar to the plane-parallel device. The advantages of a confocal configuration include ease of alignment, greatly reduced diffraction losses, and completely degenerate transverse modes.

A spherical mirror Fabry-Perot interferometer[15] consists of two identical partially transmitting mirrors separated by a distance nearly equal to their common radius (see Fig.3.1-2): it is, in effect, a confocal resonator.

An entering beam undergoes multiple reflections within the resonator. If its frequency matches that of one of the resonant modes, then, due to constructive interference, the transmission of the resonator peaks sharply. To use the interferometer as a spectrum analyser, the mirror separation is varied (e.g, by a PZT crystal). The device then scans through a range of frequencies, while a photodetector measures the intensity of the transmitted beam. Suitable electronics allow to correlate the observed peaks with the mirror separation, and thus to calculate their frequency differences (the measurement is always relative).
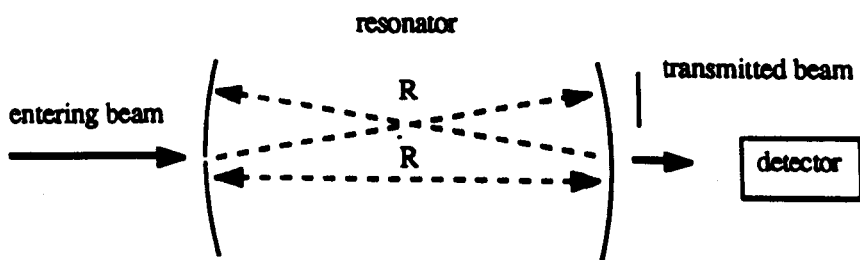
Fig.3.1-2 A spherical mirror Fabry-Perot interferometer.

Fabry-Perot spectrum analysers are characterised by several main parameters: (R and r are respectively mirror curvature and reflectivity)

finesse	$F = \pi r/(1-r^2)$	(3.1.4-1)
free spectral range	$FSR = c/4R$	
spectral resolving power	$SPR = 4RF/\lambda$	
minimum resolvable frequency difference	$\Delta v_{min} = FSR/F$	

Of these, FSR determines the range of resolvable frequencies, and Δv_{min} the resolution of the device. The relationship between the two derives from the fact that finesse is a measure of resonator linewidth.

The spectrum analyser used in the present experiment was a TecOptics SA-2M model, having a finesse of 175 and a FSR of 2GHz. The resolution was therefore 11.4MHz. The accuracy was determined by the accuracy of reading an oscilloscope screen, and was roughly 1%.

The spectrum analyser was calibrated by measuring the longitudinal mode spacing of a known He-Ne laser (Melles Griot 05-LHR-321: 570MHz).
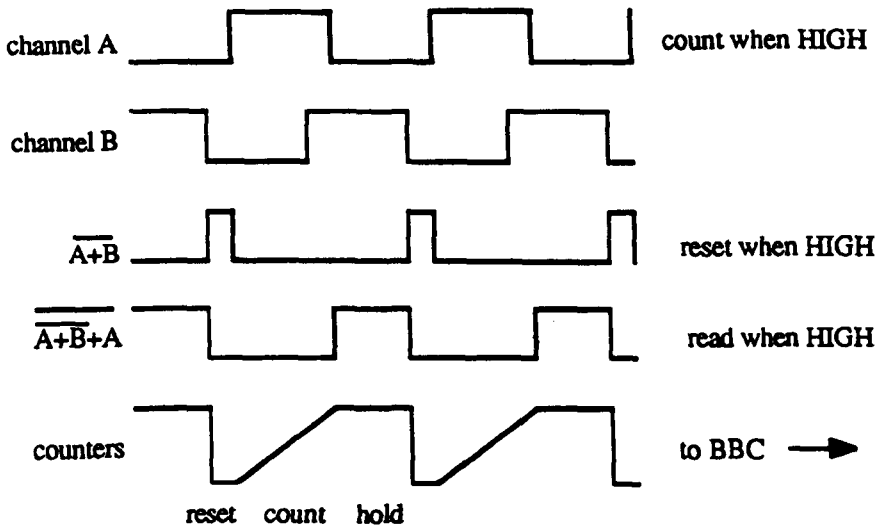
3.1.5 The readout

The gyroscope scale factor as a function of rotation rate was read by a logic circuit operating as follows (Fig.3.1-3). A two-channel shaft encoder (Hewlett-Packard HEDS 5000-A06) was attached to the rate table, each channel producing 500 pulses per revolution. The phase shift between the channels was set during the installation of the encoder, and thereafter remained constant. A counter counted pulses arriving from a crystal oscillator during the HIGH half-cycle of one of the two channel pulse trains (see Fig.3.1-3): the count was thus inversely proportional to the rate of rotation. Another counter registered the peaks of the photodiode output during the same interval. The system was therefore directly reading instantaneous fringes (photodiode peaks) per unit angle, in other words, scale factor versus rotation rate.

The data were logged by a BBC microcomputer. The output of the counters was fed into the 8-bit input/output socket through two transparent latches which were read consecutively. One of the digital outputs was used to control the latches, the other seven being available for data inputs: maximum resolution was therefore 7 bits. The READ trigger was registered by the analogue input of the computer. A BASIC program read in the data and recorded it in ASCII format.
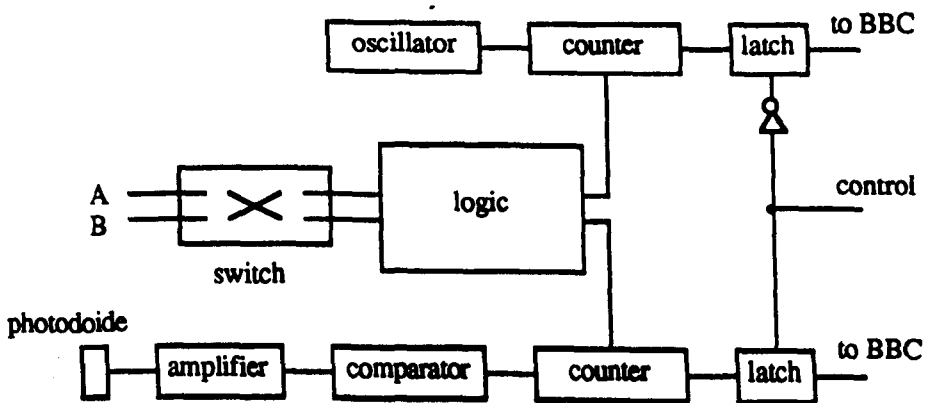
The readout time was set by the counting interval, and could be as short as 0.05s; the dead time equalled three reading periods. The crystal oscillator was set to run at 300Hz: the measurable rotation rate was thus between 0.015rad/s $\approx 3 \cdot 10^3$deg/hr and 0.2rad/s $\approx 4 \cdot 10^4$deg/hr. The accuracy was between ~1% (low rate) and ~5% (high rate). The photodiode frequency was reduced by a factor of 16 (by a series of 4 D-flip-flops) in order to accomodate the count within 7 bits. The S-factor accuracy was therefore $2 \cdot 10^{-9}$counts/rad or ~2%.

The data were stored on floppy discs. Initially they were displayed on the BBC using ICHART™ software. Later they were transferred onto an Apple Macintosh for final editing, curve fitting and plotting.

channel A ⎍⎍⎍ count when HIGH

channel B ⎍⎍⎍

$\overline{A+B}$ ⎍⎍⎍ reset when HIGH

$\overline{\overline{A+B}+A}$ ⎍⎍⎍ read when HIGH

counters ⎍⎍⎍ to BBC →

reset   count   hold

a

oscillator — counter — latch — to BBC

A
B — switch — logic — control

photodoide — amplifier — comparator — counter — latch — to BBC

b

Fig.3.1-3 The readout circuit: a) a timing diagram; b) a block diagram.

Note: Since the roles played by the two channels in the circuit were different, on reversing the sense of rotation the connections had to be interchanged - hence the switch in Fig.3.1-3b.

67

3.1.6 The H.V. power supply

A schematic drawing of the H.V. circuit is shown in Fig.3.1-4. In order to circumvent Langmuir flow (see Sec.2.2.5), both lasers used in the experiment had a double-arm discharge, with two anodes and a common cathode. Two identical H.V. power supplies were used to power the anodes independently. These were the Brandenburg ALPHA II series, model 2507R, featuring remote voltage control and current monitor. Maximum voltage and current were respectively 5kV and 5mA.

The ballast resistance was 1MΩ for both arms. In addition, a 100kΩ resistor was attached directly to each anode, placed there because in its absence the discharge went into rapid on-off oscillation. A possible explanation may be that the resistor acted to damp the inductive-capacitive resonance circuit created by the HT coaxial cable.
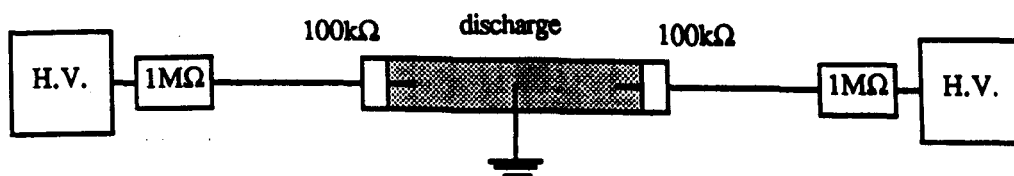

Fig.3.1-4 A schematic drawing of the H.V. circuit.

3.1.7 The rate table

The rate table used in the experiment was designed by Dr. Hobson and made in the departmental workshop. From the point of view of construction, this was the most difficult part to carry out. Fig.3.1-5 shows a schematic view.

The 0.5m diameter rate table turned on bearings with very little friction, causing no noise in the gyroscope. This aspect of it was entirely successful.

Regrettably, however, it proved impossible to drive the table at a constant rate. Both a DC motor and a step motor were tried, together with several types of drive, with roughly similar results. The motors caused fluctuations in speed of ~10% or more, and also superposed additional vibration-induced frequencies on the gyroscope output.

Eventually, the problem was "solved" by turning the table by hand while using a fast electronic readout (see Sec.3.1.5 above). Unfortunately, very near threshold the rate of rotation could not be maintained steadily enough to capture the just-above-threshold values.
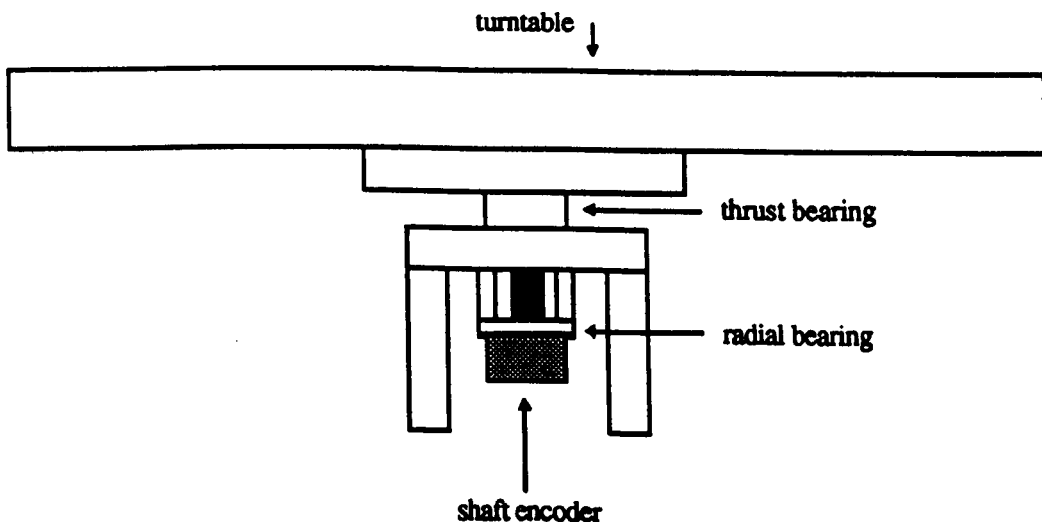
Fig.3.1-5 A schematic view of the rate table.

3.2 THE RING LASERS
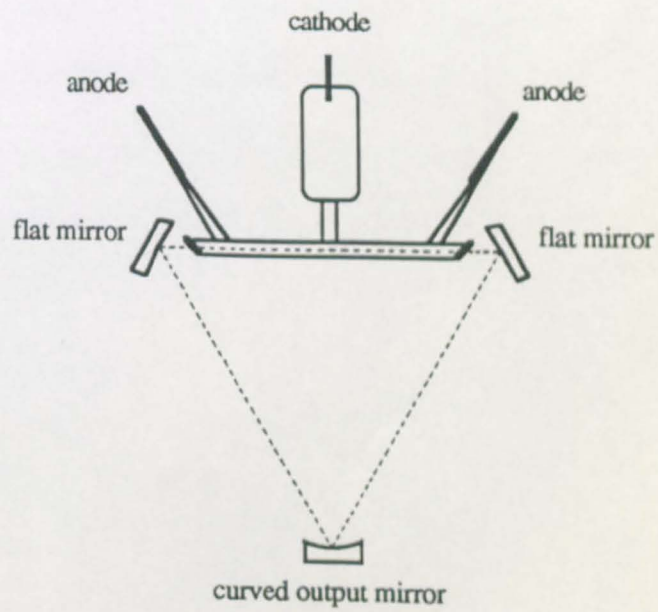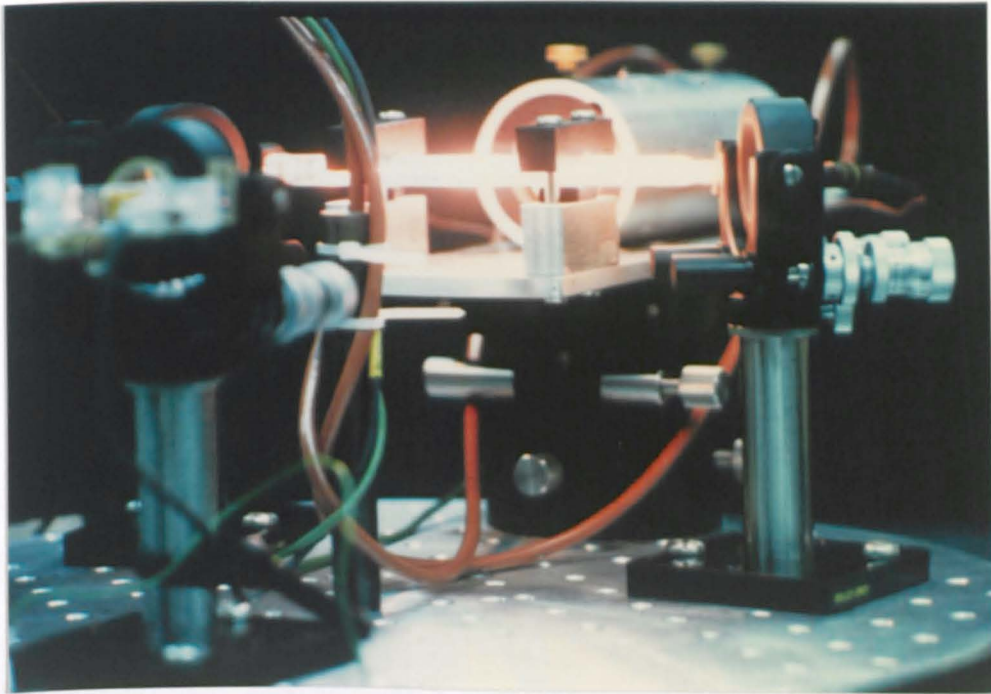
3.2.1 The modular ring laser

Fig.3.2-1 The modular ring laser gyroscope.

The ring laser used in the earlier experiments was a modular one, constructed from a discharge tube and three mirrors (see Fig.3.2-1 on the previous page) and aligned using a technique similar to that of Ref.12.

The discharge tube, donated by Paul Cook, had the following parameters:

overall length	127mm along centreline
discharge length	2x45mm
bore diameter	1.1mm
pressure	3Torr
gas mixture	He:Ne=10:1
	He: 99.92% He^3
	$Ne^{20}:Ne^{22}=9:1$
Brewster windows	perpendicular to the plane of the tube

The voltage-current characteristic is plotted in Fig.3.2-2. The normal operating voltage was 3.5kV. A current balancing circuit, run off the H.V. current monitors, kept the two currents equal to within $0.2\mu A$.

Fig.3.2-3 shows the output power as a function of supply voltage. The power meter consisted of a photodiode and an op-amp, and was uncalibrated: the measurement was thus relative rather than absolute.
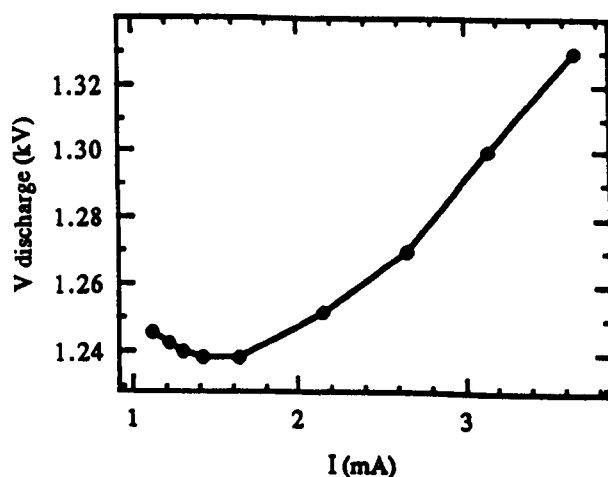

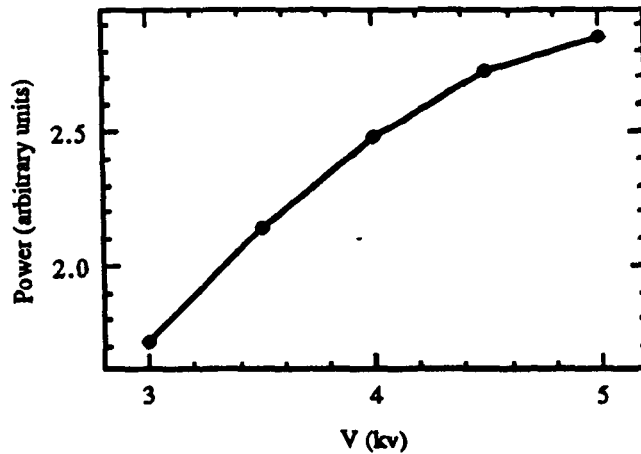Fig.3.2-2 Discharge voltage versus current.

Fig.3.2-3 Power output of the modular ring laser versus supply voltage.

The mirrors, on loan from British Aerospace, were some of their special gyroscope low-backscatter mirrors[30]. The backscatter coefficient is estimated to be 10^{-4}. The resonator parameters were:

resonator length	53 ± 1cm
curved mirror radius .	70cm
longitudinal mode separation	calculated: 565 ± 10MHz
	measured: 555 ± 5MHz

The spot size of the TEM_{10} mode would have been 0.6mm: the bore diameter was therefore too narrow to support transverse modes.

The difficulty of mounting the discharge tube vertically meant that the gyroscope operated in the less efficient p-mode (see Sec.2.3.2).

The ideal S-factor was $(0.161\pm0.003)\cdot10^6$ counts/rad.
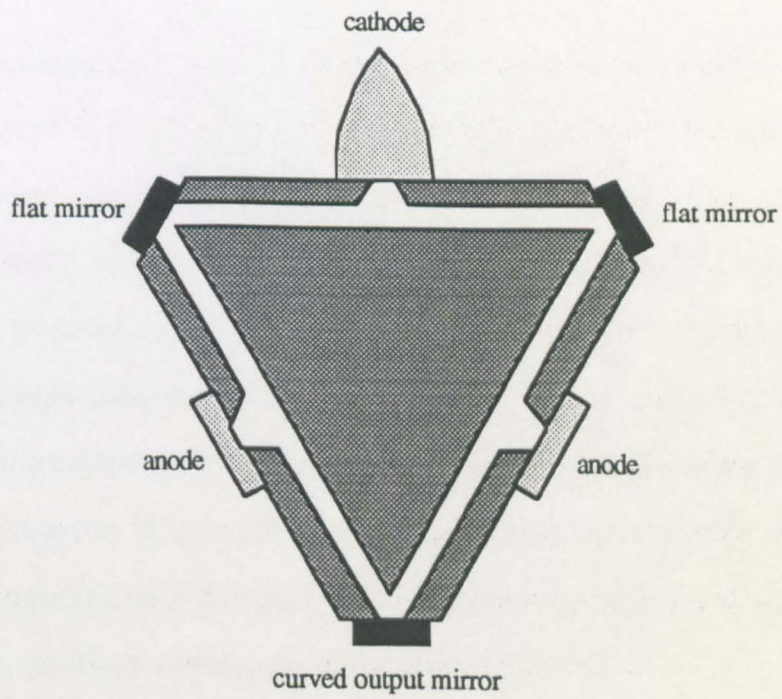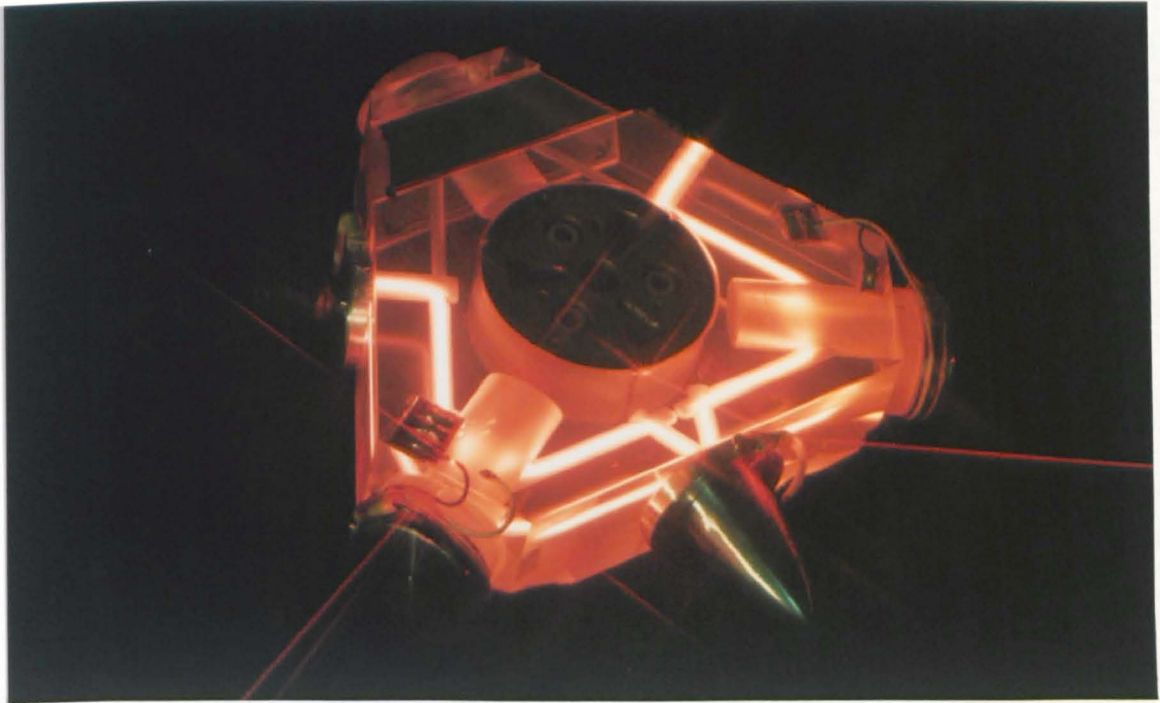
3.2.2 The solid-block ring laser

Fig.3.2-4 The solid-block ring laser gyroscope.

In later experiments, a solid-block ring laser was used. The ring laser was made of Zerodur, a crystalline material with the thermal expansion coefficient of $\sim 10^{-7} deg^{-1}$, so as to minimise pathlength variation due to changes in temperature. It was in fact a British Aerospace gyroscope, on loan. The laser parameters were as follows:

resonator length	43cm
discharge length	2x1/3 of the above
bore diameter	3mm
curved mirror radius	3m
pressure	4.5Torr
gas mixture	He:Ne=15:1
	$Ne^{20}:Ne^{22}=1:1$
gain/loss	1.5
round-trip loss	0.2%

Since the gas within the laser formed a closed loop, there were two possible paths for either of the currents to follow. As a result, when switched on the discharge almost invariably established itself along one of the anode-anode-cathode paths, adopting one branch in clear preference to the other. To cope with this problem, remote voltage control was installed which turned on both H.V. voltages simultaneously. Even then, it always took several attempts to achieve the correct anode-cathode-anode discharge. The outputs of the power supplies being in effect connected together interfered with the working of the current monitors: in consequence, it was impossible either to obtain a current reading or to check whether the currents were balanced.

Fig.3.2-5 shows the output power as a function of supply voltage (again uncalibrated). The normal operating voltage was 3kV.
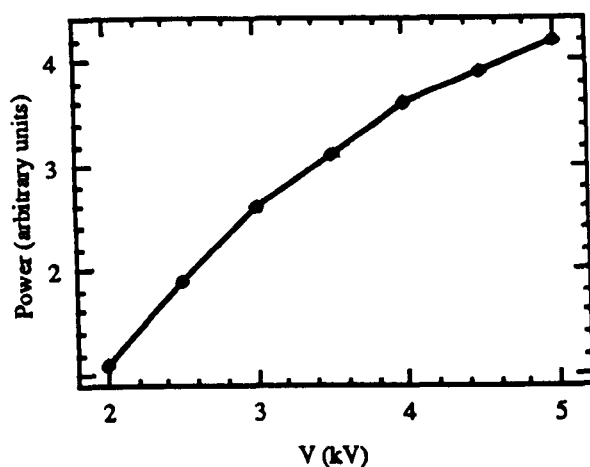
74

Fig.3.2-5 Power output of the solid-block gyroscope versus supply voltage.

The resonator mode spacings were:

	calculated	measured
longitudinal	698 MHz	695 ± 7 MHz
transverse 10	414MHz	415 ± 4 MHz
transverse 01	56MHz	55 ± 1 MHz

One of the mirrors was mounted on a PZT crystal: this was used for pathlength control and mode selection. The TEM_{01} mode was very weak, indeed under normal operating conditions it was below threshold. The other modes could be obtained in various combinations discussed in the following chapter. Mode stability was very good: with no feedback control circuit, mode intensity ratios remained constant to within 10% for ~1/2hr.

The ideal S-factor was $0.131 \cdot 10^6$counts/rad.

Chapter 4

EXPERIMENTAL RESULTS

4.1 RESULTS: MODULAR GYROSCOPE

4.1.1 Scale factor of the modular ring laser

In measuring the scale factor of the modular gyroscope two problems were encountered.

First, the modular ring laser was by its very nature prone to vibration. This led to considerable scattering of the points, since hand-driven motion made some vibration inevitable. At high rotation rates the vibration frequency was below that of the signal, and so less detrimental to accuracy. At low rates, however, the two frequencies were comparable leading to significant smearing of the data curve.

A much more serious problem was presented by the back reflection from the Fabry-Perot spectrum analyser, which was fed into the resonator causing fluctuations in the output intensity. These occurred at the scanning frequency and had twice the amplitude of the gyroscope heterodyne signal. Blocking off the reflection reduced interference but did not eliminate it entirely. As a result, it was impossible to monitor the modes while simultaneously collecting the data.

Indeed, the problem extended even further. The discharge tube of the modular gyroscope was filled with the natural abundance mixture of $Ne^{20}:Ne^{22}=9:1$ instead of the proper equal-isotope recipe. The ring laser was therefore subject to mode competition. Enhancing one of the counter-propagating beams by adding to it a small part of the spectrum analyser back reflection could well result in the other beam being extinguished. Indeed, this

would explain the abovementioned intensity fluctuations as well as the fact that they were not observed in the solid-block gyroscope. The flickering of the beam would not be visible, occuring as it must at the scanning frequency of ~200Hz.

Only a single mode was observed by the spectrum analyser. It was sufficiently stable, roughly maintaining its position over a period of ~10min and responding as expected to pathlength variation by a PZT-mounted mirror: pathlength stabilisation was unnecessary. Nevertheless, two simultaneous modes were exceedingly difficult to obtain for more than ~1s at a time.

Figs.4.1-1 & 4.1-2 show the output frequency of the modular gyroscope as a function of rotation rate. Clockwise and counter-clockwise data - 500 points each - being similar in every respect, are plotted together on the same graph (compare the solid-block gyroscope in Ch.4.2 below). The error is the digitising error of ± 1 column/row. Fig.4.1-1 was taken immediately after the laser was switched on, Fig.4.1-2 6 hours later: the laser was left running throughout and remained stationary for most of that time.

The speed was varied randomly - although great efforts were made to keep the variation smooth - the points therefore were not acquired in any particular order.

Varying the pathlength made no difference to the shape of the data curves.

The solid line is the best fit to the function (Eq.2.4.1-22)

$$f = S_0 (\Omega^2 - \Omega_L^2)^{1/2}$$

The fit was performed in the following manner: f^2 was plotted against Ω^2 to obtain the linear relationship $f^2 = S_0^2 \Omega^2 - S_0^2 \Omega_L^2$; a least-squares fit to a first-degree polynomial then gave S_0^2 (the slope) and $S_0^2 \Omega_L^2$ (the intercept). Figure captions list the values of S_0 and Ω_L, along with the value of χ^2.
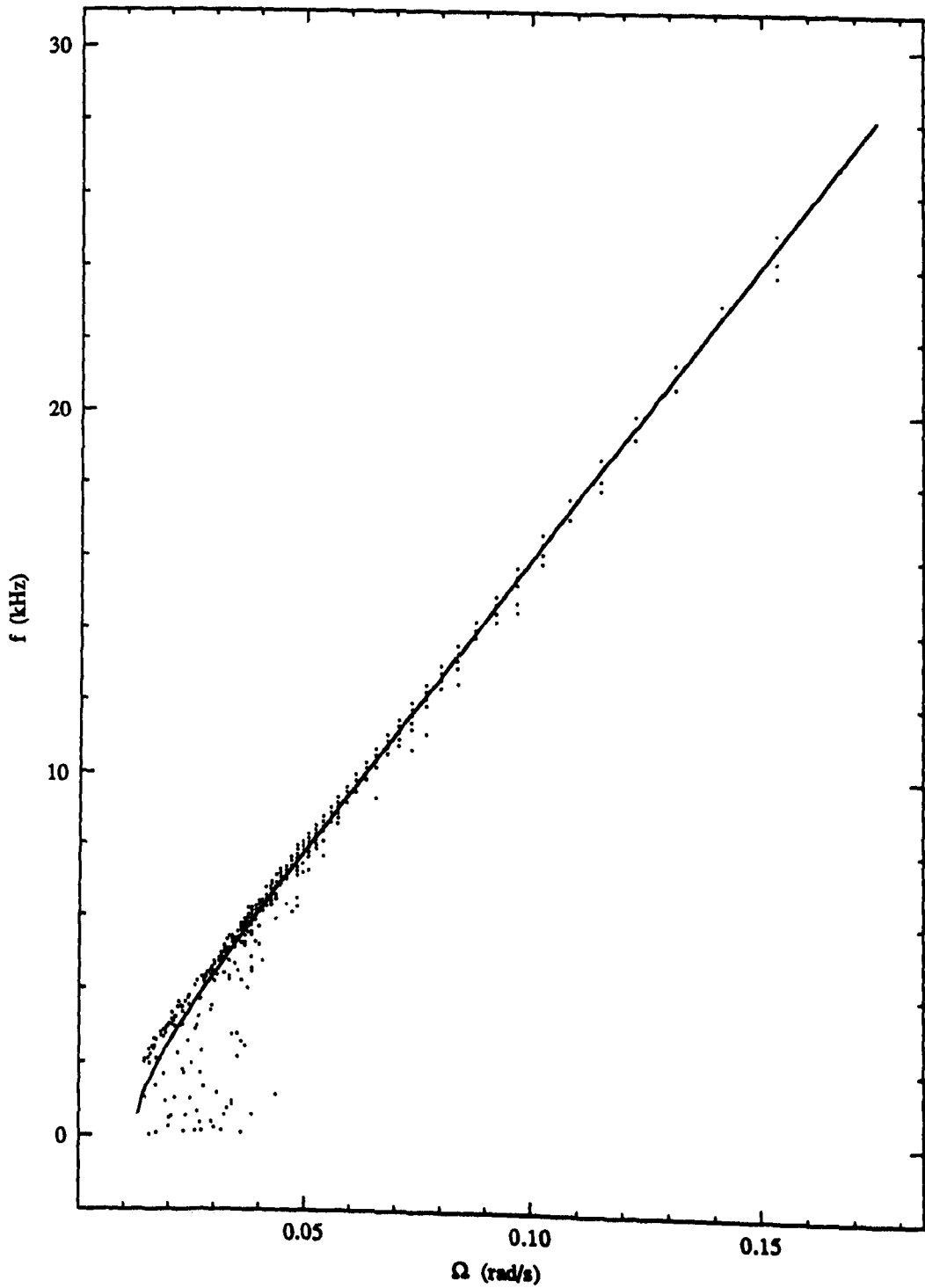
Fig.4.1-1 Scale factor versus rotation rate: 1/2 hr after switch- on.

$S_0 = (0.16110 \pm 0.00003) \cdot 10^6 \text{counts/rad},\ \Omega_L = 0.01247 \pm 0.00005 \text{rad/s},\ \chi^2 = 4.1 \cdot 10^4.$
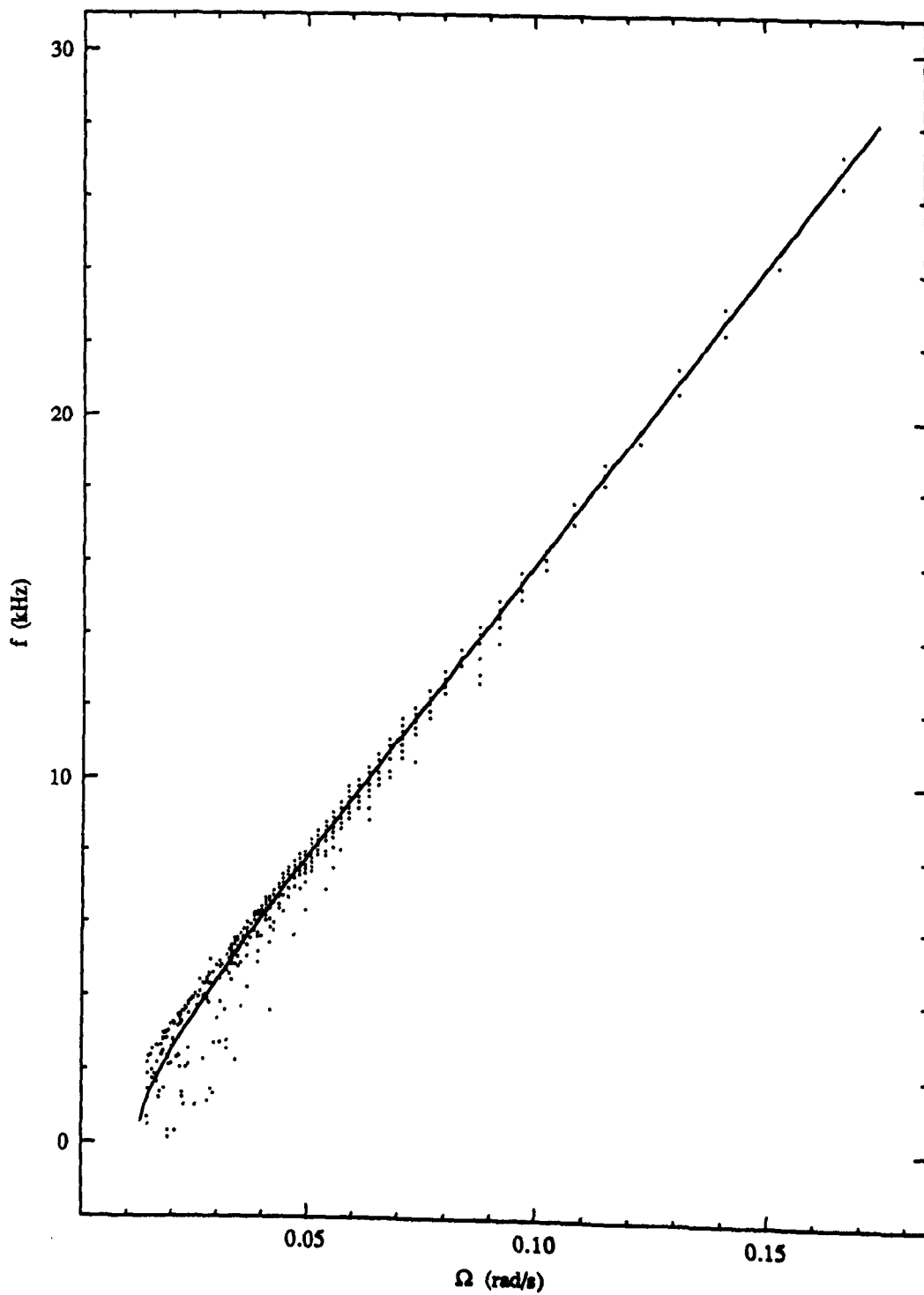
Fig.4.1-2 Scale factor versus rotation rate: 6 hr after switch- on.

$S_0 = (0.16092 \pm 0.00003) \cdot 10^6$counts/rad; $\Omega_L = 0.01250 \pm 0.00005$rad/s, $\chi^2 = 3.6 \cdot 10^4$.

4.1.2 Discussion

It is evident that both Figs.4.1-1 & 4.1-2 demonstrate an excellent fit to the frequency equation Eq.2.4.1-22.

The measured value of $S_0 - 0.161 \cdot 10^6 \text{counts/rad}$ - agrees with that calculated in Sec.3.2.1 from purely geometrical considerations - $(0.161 \pm 0.003) \cdot 10^6 \text{counts/rad}$. The lock-in threshold, $S_0\Omega_L \approx 2\text{kHz}$, is roughly as estimated in Sec.2.4.1 (1kHz).

In sum, these results provide a check on the instrumentation and demonstrate that the data acquired and analysed by this method are indeed reliable.

4.2 RESULTS: SOLID-BLOCK GYROSCOPE

4.2.1 Scale factor of the solid-block ring laser

The figures on the following pages show the solid-block gyroscope data for different combinations of oscillating modes, obtained by scanning the gain curve with a PZT-mounted mirror.

The figures are representative of a series of measurements, some of which were taken soon after switching on of the laser, and others several hours later, with the laser kept running throughout and left stationary for the great part of that time.

The figures are laid out in a fashion similar to that of Ch.4.1. In this instance, however, the data for clockwise and counter-clockwise rotation, where substantially different, are plotted separately: figure headings give the sense of rotation. The error is once more the digitising error of ±1 column/row.

Unlike Ch.4.1, the solid line here denotes the best fit to the null-shifted frequency function

$$f = S_0 \, [(\Omega + \Omega_N)^2 - \Omega_L^2]^{1/2}$$

To achieve a fit, f^2 was plotted against Ω giving the square relationship

$$f^2 = (S_0^2)\Omega^2 + (2S_0^2\Omega_N)\Omega + [S_0^2(\Omega_N^2 - \Omega_L^2)]$$

which was then fitted by least-squares to a second-degree polynomial. (See Sec.4.2.3 for a brief discussion of alternative fitting schemes.) Figure captions

82

give the values of S_0, Ω_L, Ω_N and χ^2 *.

The insets show the relative mode intensity (L and T stand for "longitudinal" and "transverse"). Unfortunately, due to the resonator geometry, it was not possible to obtain two longitudinal modes without a transverse one intervening between them; nor to have two equal intensity modes without a third one appearing as well.

---

* The "χ^2" value is not the true statistical χ^2, but rather a measure of the quality of the fit estimated from the sum of the squares of the distances between each individual point and the fitted curve, i.e.

$$\chi^2 = \Sigma (y_{data} - y_{fit})^2$$

CW

Fig.4.2-1 Scale factor versus rotation rate:

single mode; 1/2 hr after switch-on, CW;

$S_0 = (0.120 \pm 0.001) \cdot 10^6$counts/rad, $\Omega_L = 0.043 \pm 0.001$rad/s, $\Omega_N = 0.035 \pm 0.001$rad/s, $\chi^2 = 2 \cdot 10^4$.
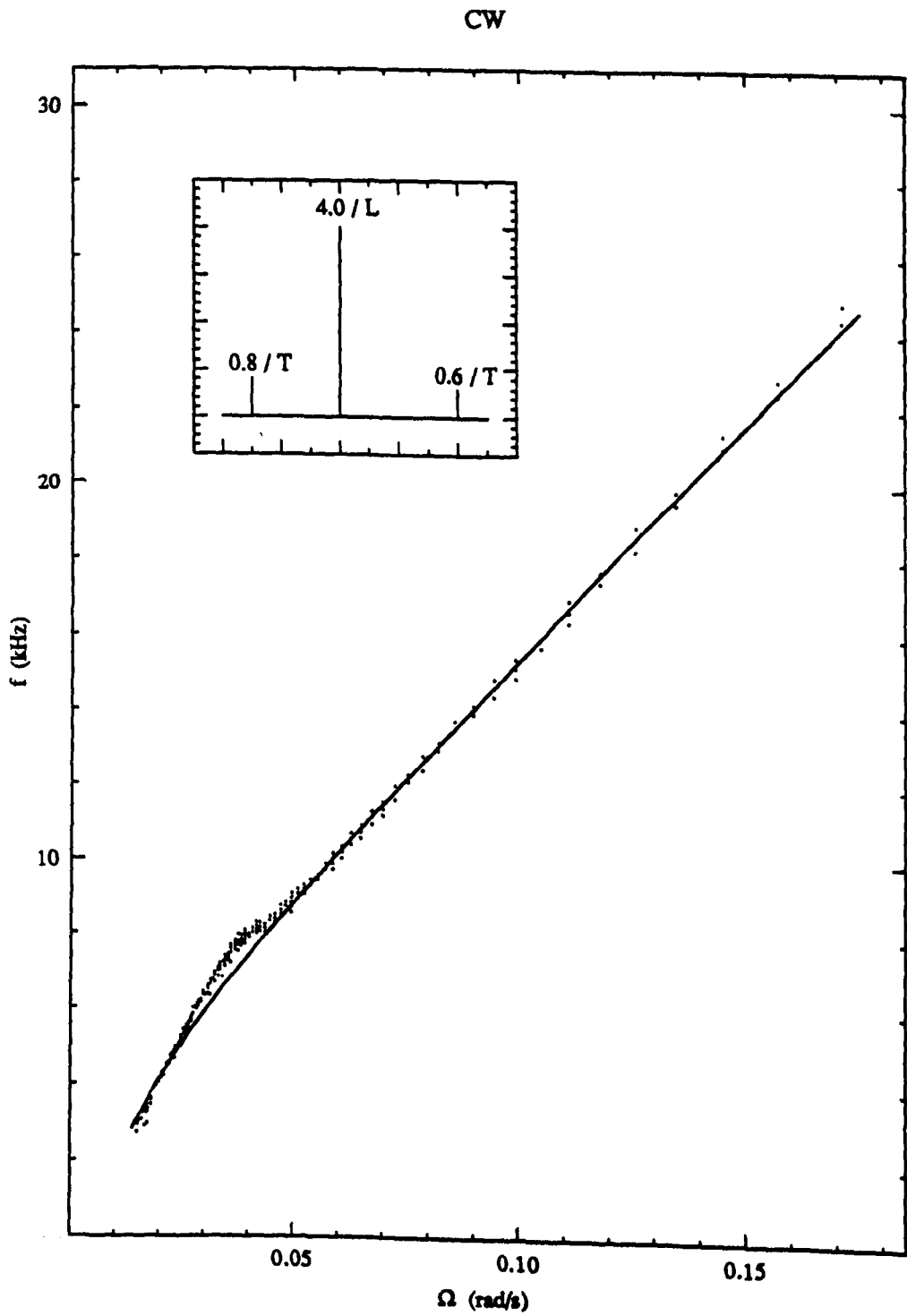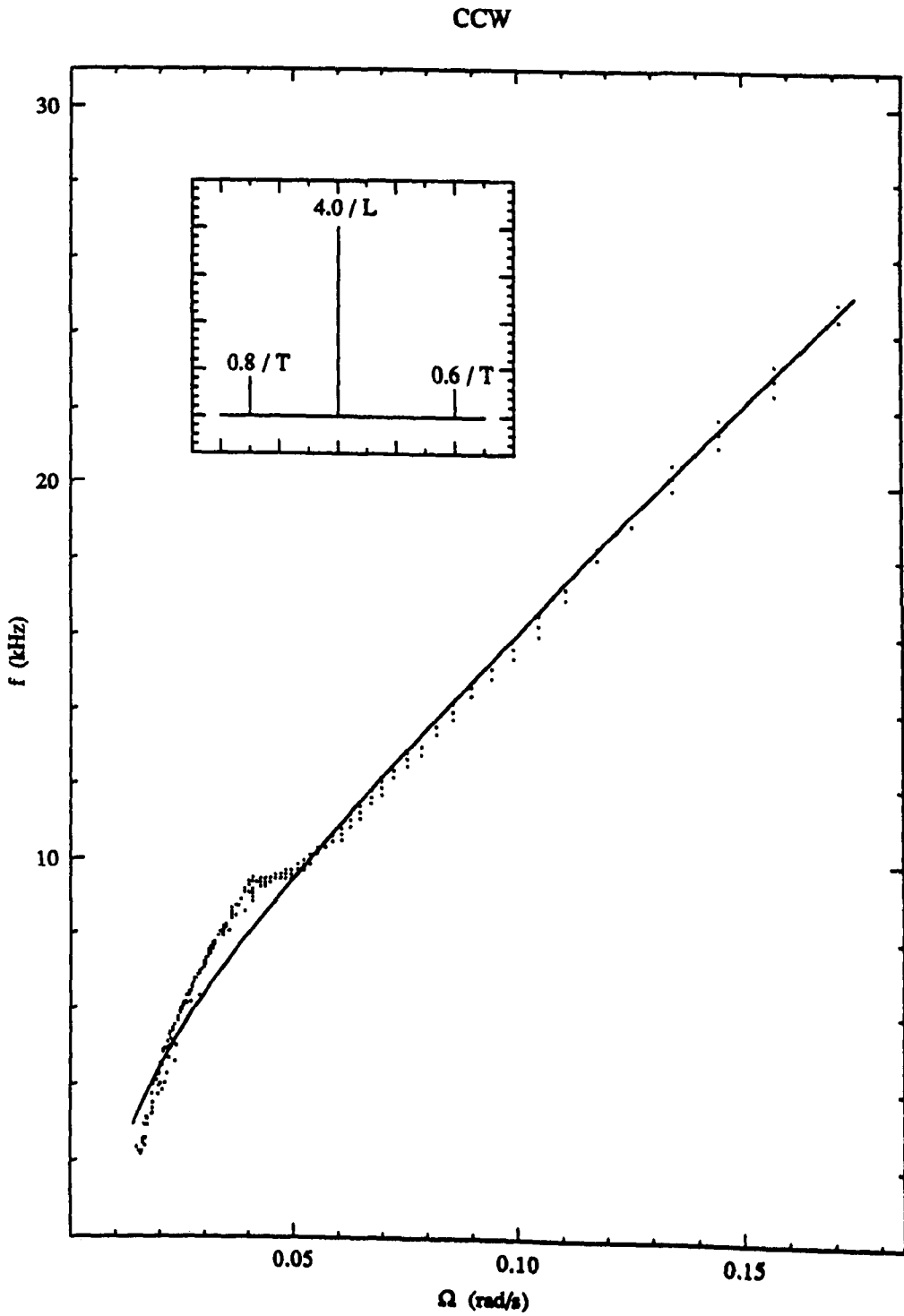
CCW

Fig.4.2-2 Scale factor versus rotation rate:

single mode; 1/2 hr after switch-on, CCW;

$S_0 = (0.113 \pm 0.001) \cdot 10^6$counts/rad, $\Omega_L = 0.065 \pm 0.001$rad/s, $\Omega_N = 0.056 \pm 0.001$rad/s, $\chi^2 = 6 \cdot 10^4$.
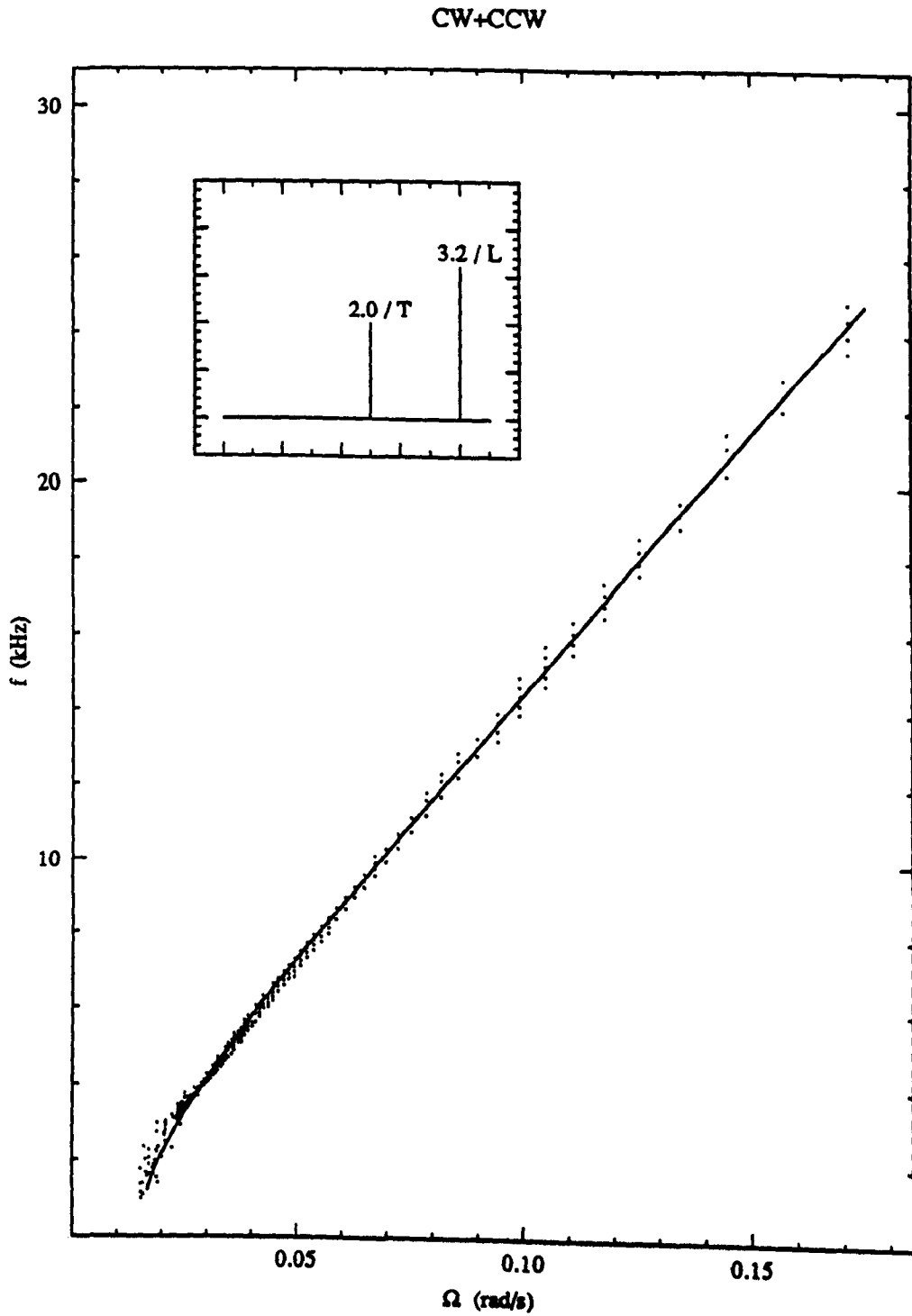
CW+CCW

Fig.4.2-3 Scale factor versus rotation rate:

two modes; 1/2 hr after switch-on, CW+CCW;

$S_0 = (0.134 \pm 0.001) \cdot 10^6$ counts/rad, $\Omega_L = 0.023 \pm 0.001$ rad/s, $\Omega_N = 0.008 \pm 0.001$ rad/s, $\chi^2 = 3 \cdot 10^4$.

CW

Fig.4.2-4 Scale factor versus rotation rate:

two unequal modes, CW;

$S_0 = (0.124 \pm 0.001) \cdot 10^6 \text{counts/rad}, \ \Omega_L = 0.031 \pm 0.001 \text{rad/s}, \ \Omega_N = 0.024 \pm 0.001 \text{rad/s}, \ \chi^2 = 3 \cdot 10^4.$

CCW

Fig.4.2-5 Scale factor versus rotation rate:

two unequal modes, CCW;

$S_0 = (0.121\pm0.001)\cdot10^6$ counts/rad, $\Omega_L = 0.033\pm0.001$ rad/s, $\Omega_N = 0.029\pm0.001$ rad/s, $\chi^2 = 6\cdot10^4$.
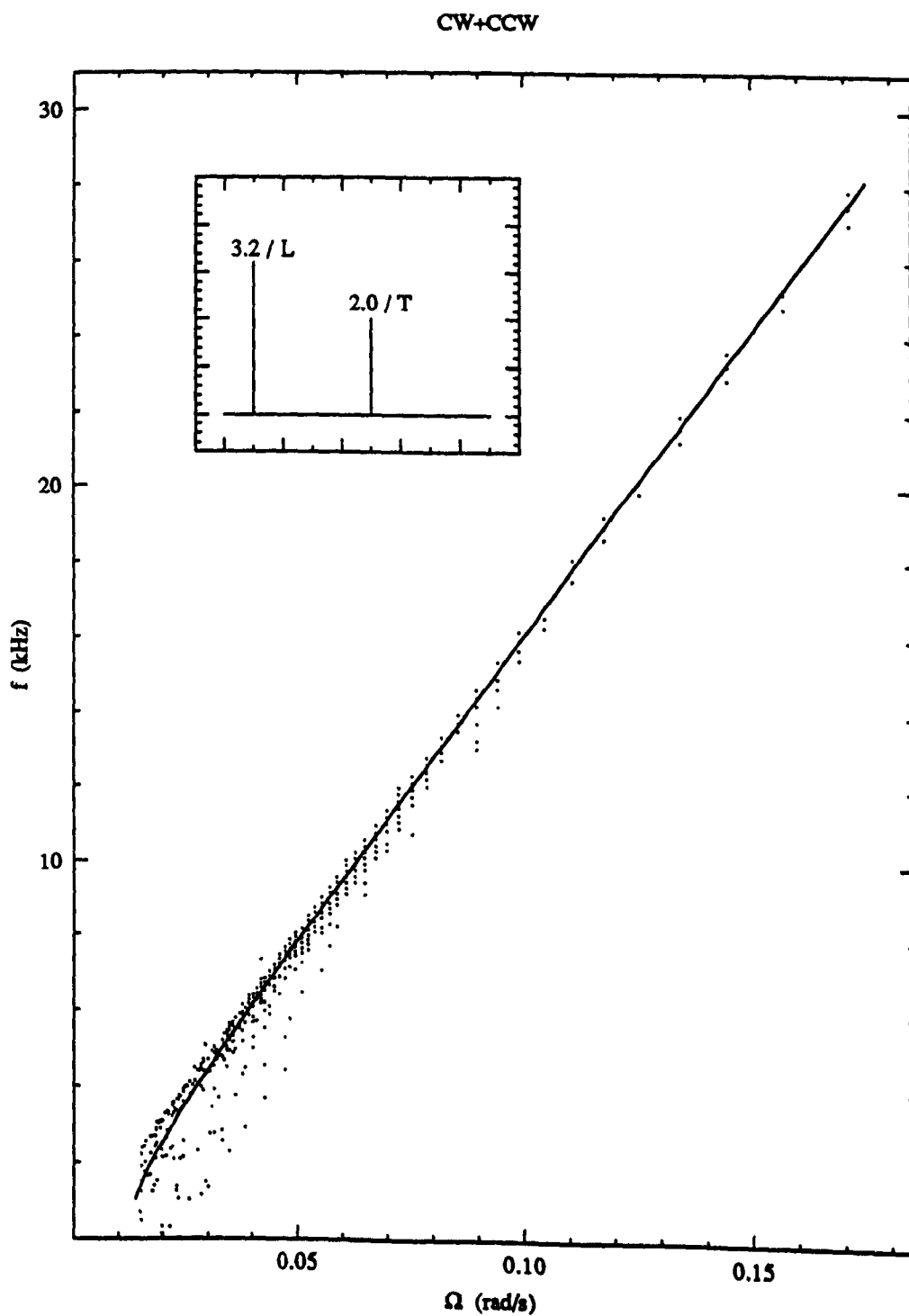
CW+CCW

Fig.4.2-6 Scale factor versus rotation rate:

two (other) modes, CW+CCW;

$S_0=(0.161\pm0.001)\cdot10^6$counts/rad, $\Omega_L=0.012\pm0.001$rad/s, $\Omega_N=0.000\pm0.001$rad/s, $\chi^2=4\cdot10^4$.

CW
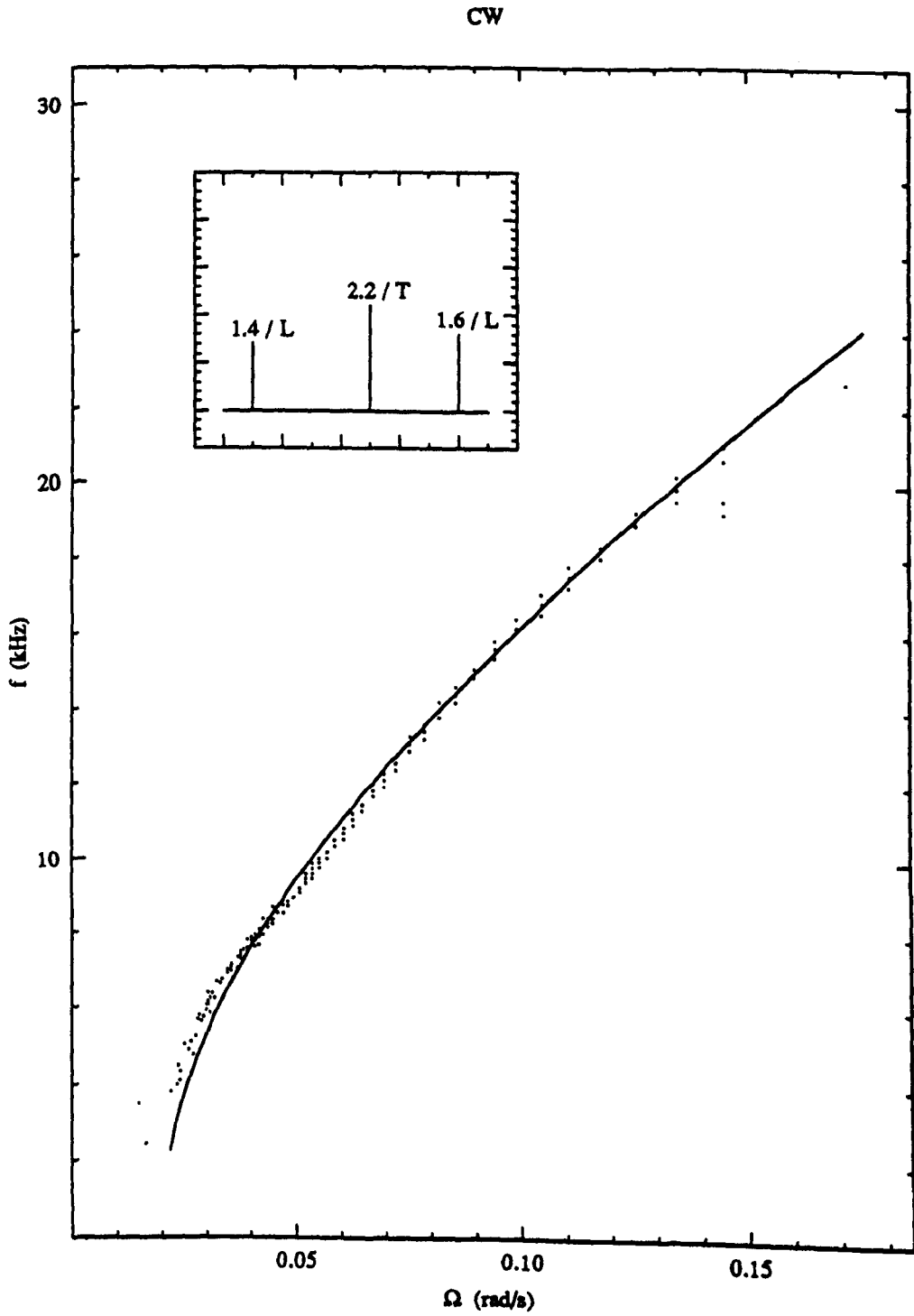
Fig.4.2-7 Scale factor versus rotation rate:

three modes, CW;

$S_0=(0.080\pm0.001)\cdot10^6$counts/rad, $\Omega_L=0.215\pm0.001$rad/s, $\Omega_N=0.195\pm0.001$rad/s, $\chi^2=3\cdot10^4$.

CCW
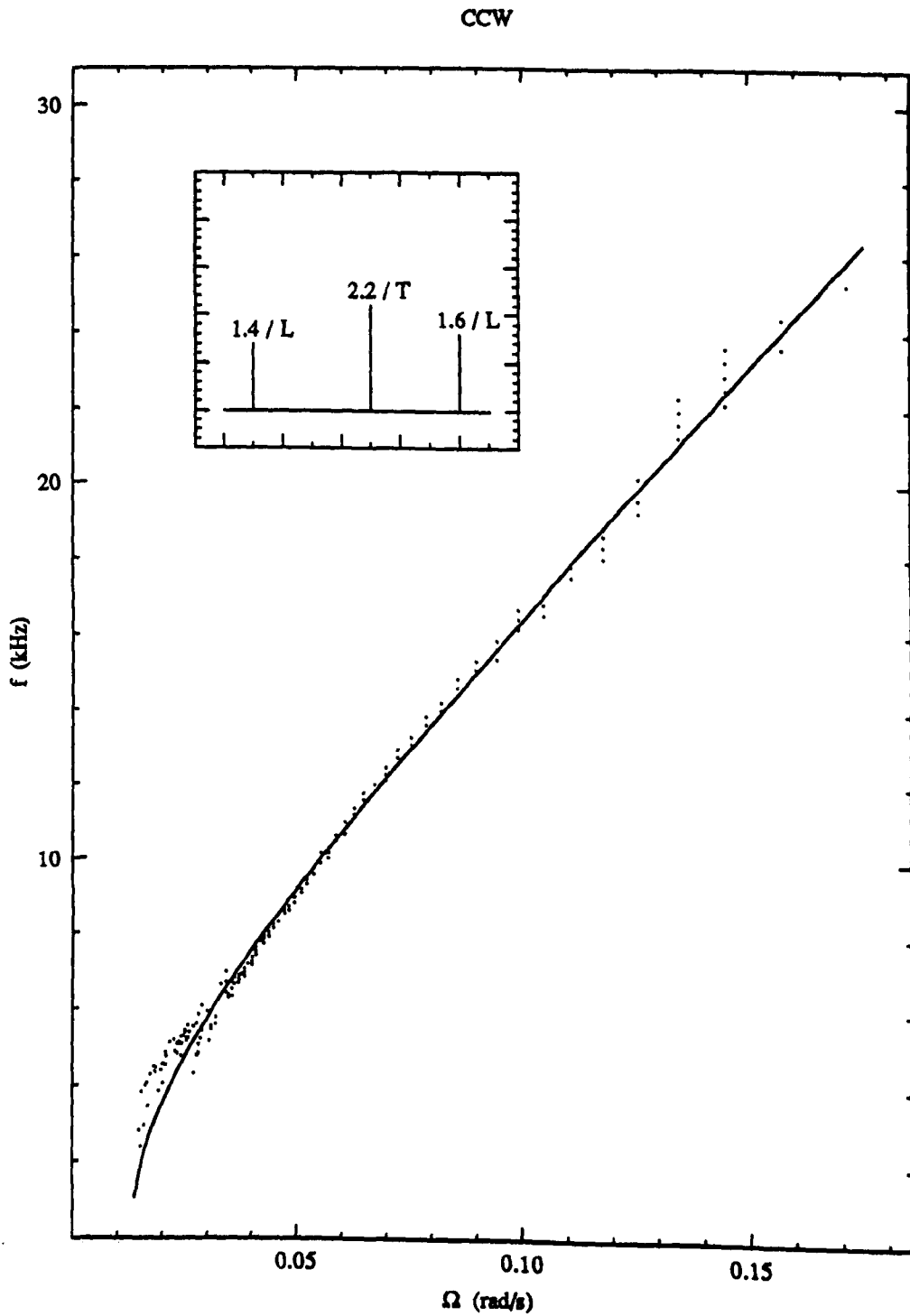
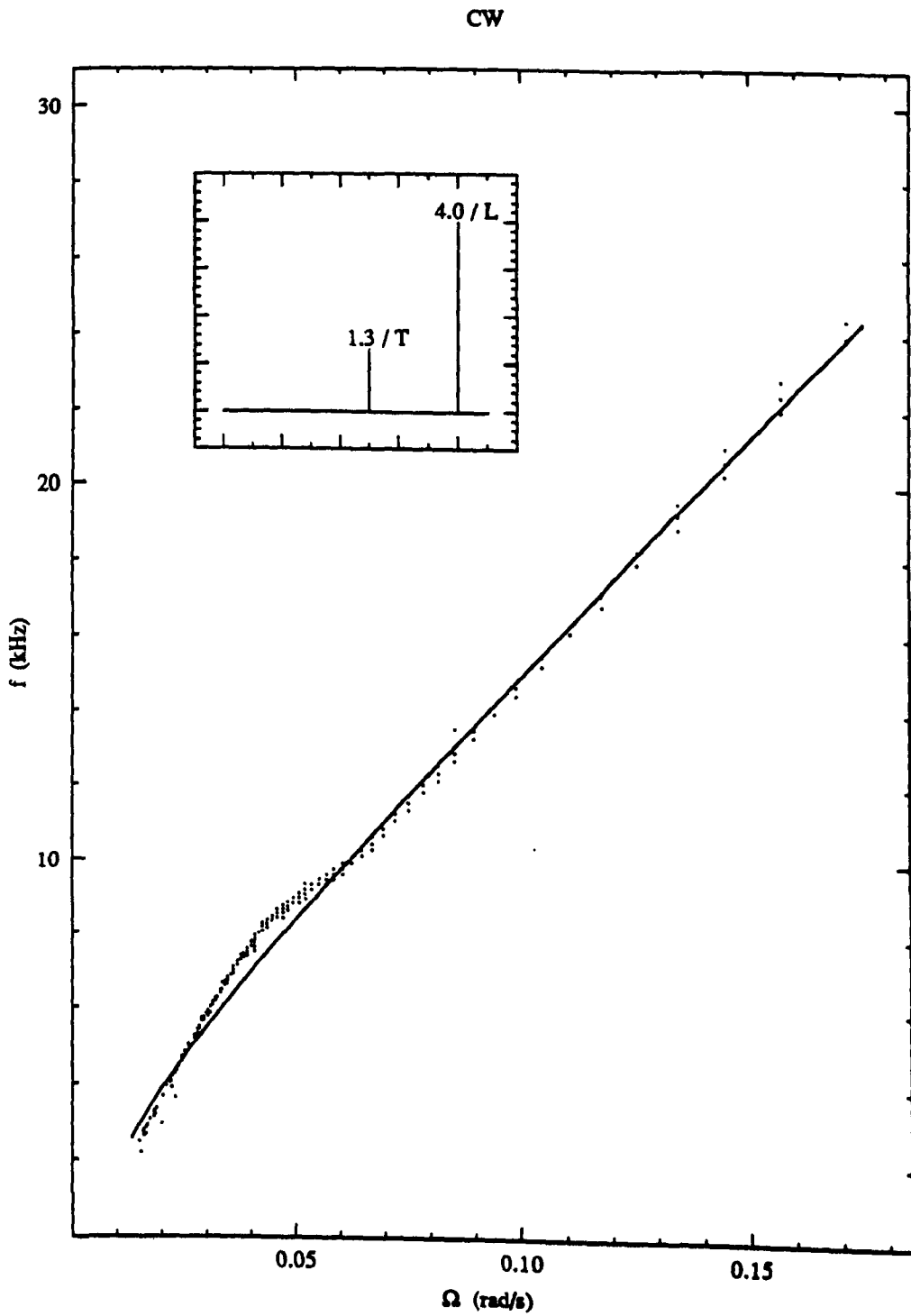

Fig.4.2-8 Scale factor versus rotation rate:

three modes, CCW;

$S_0 = (0.127 \pm 0.001) \cdot 10^6$counts/rad, $\Omega_L = 0.039 \pm 0.001$rad/s, $\Omega_N = 0.052 \pm 0.001$rad/s, $\chi^2 = 5 \cdot 10^4$.

CW+CCW

Fig.4.2-9 Scale factor versus rotation rate:

two modes; 6 hr after switch-on, CW+CCW;

$S_0 = (0.135 \pm 0.001) \cdot 10^6$ counts/rad, $\Omega_L = 0.022 \pm 0.001$ rad/s, $\Omega_N = 0.009 \pm 0.001$ rad/s, $\chi^2 = 2 \cdot 10^4$.

CW

Fig.4.2-10 Scale factor versus rotation rate:

single mode; 6 hr after switch-on, CW;

$S_0 = (0.124 \pm 0.001) \cdot 10^6 \text{counts/rad}$, $\Omega_L = 0.034 \pm 0.001 \text{rad/s}$, $\Omega_N = 0.029 \pm 0.001 \text{rad/s}$, $\chi^2 = 2 \cdot 10^4$.
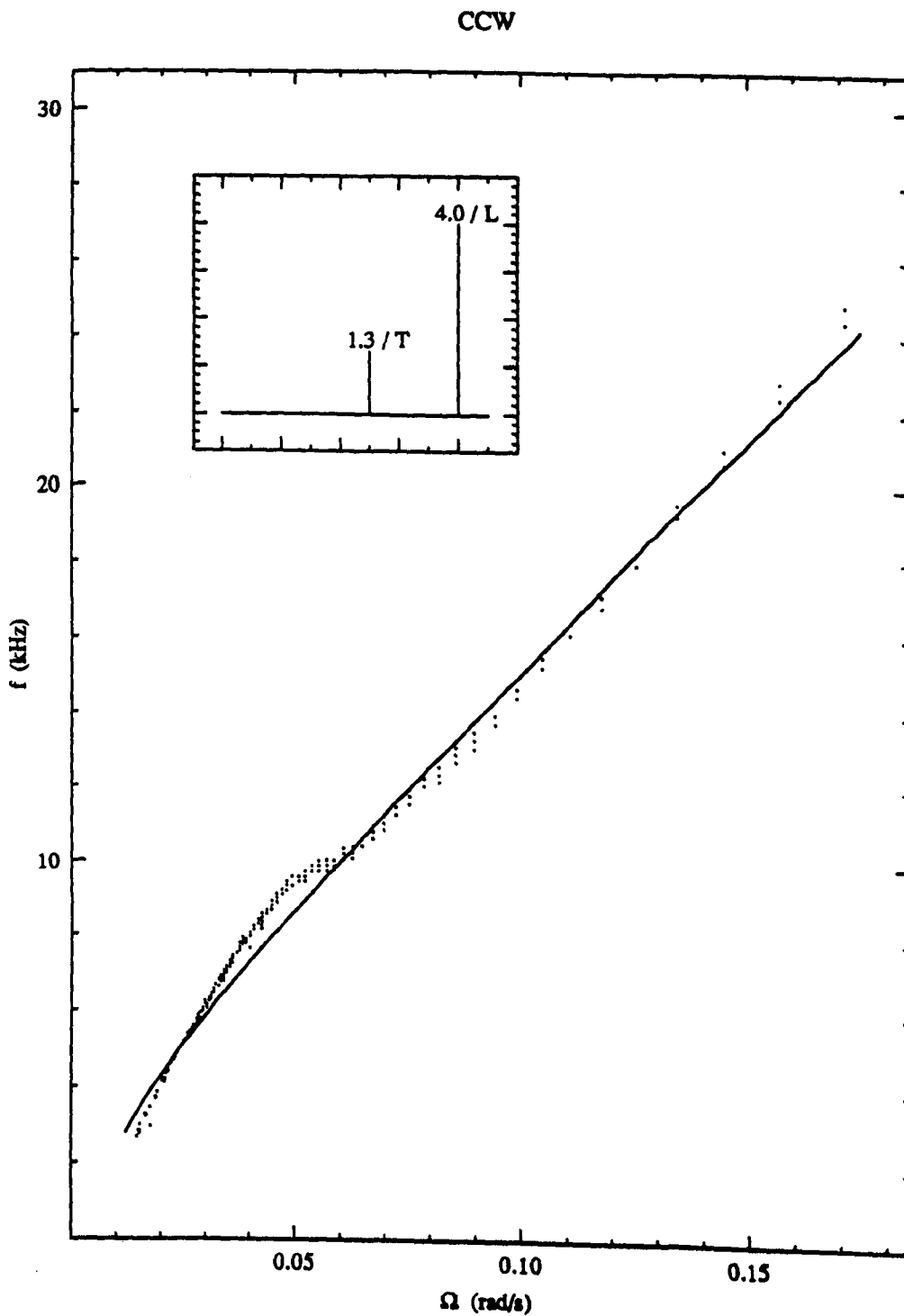
Fig.4.2-11 Scale factor versus rotation rate:
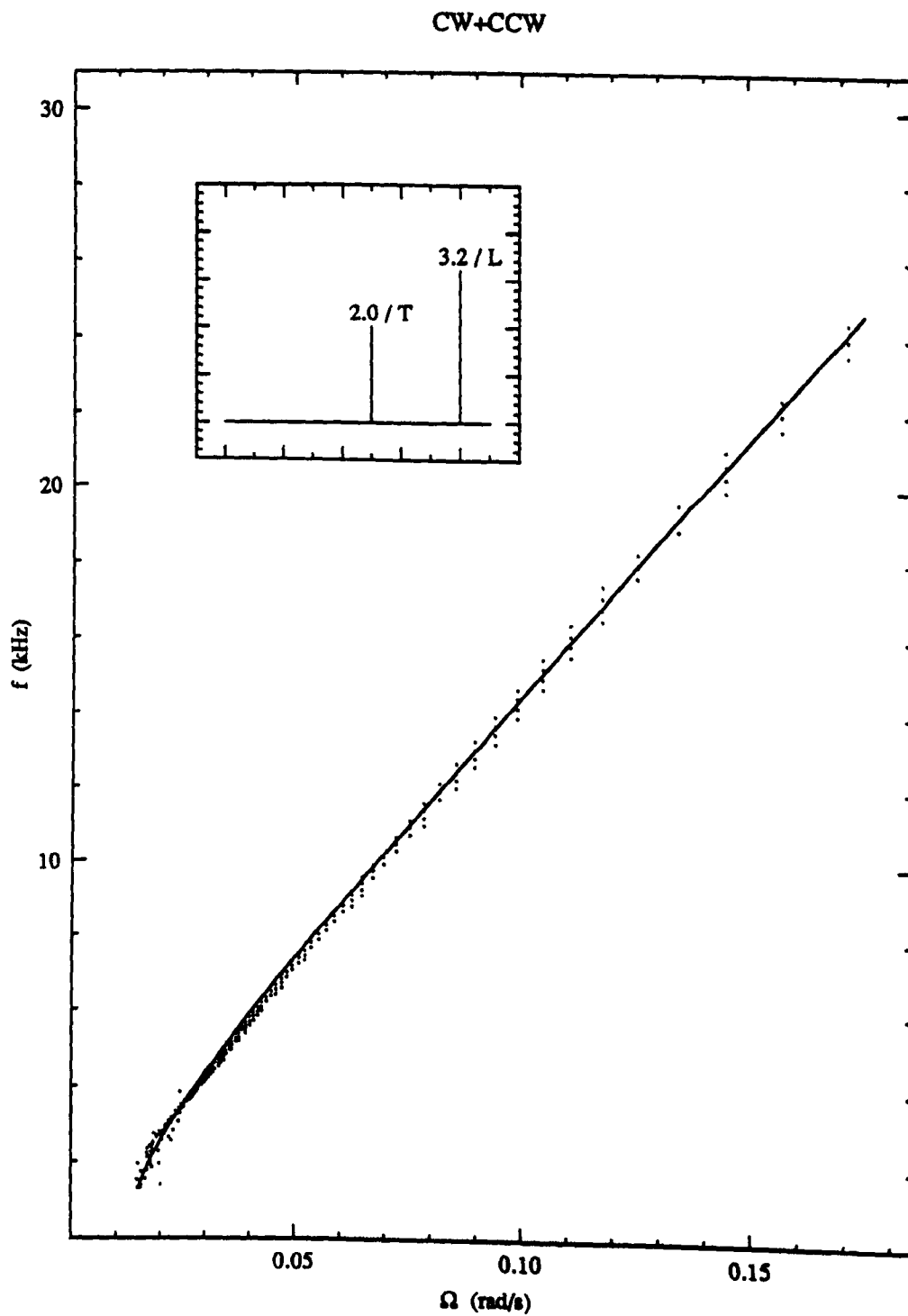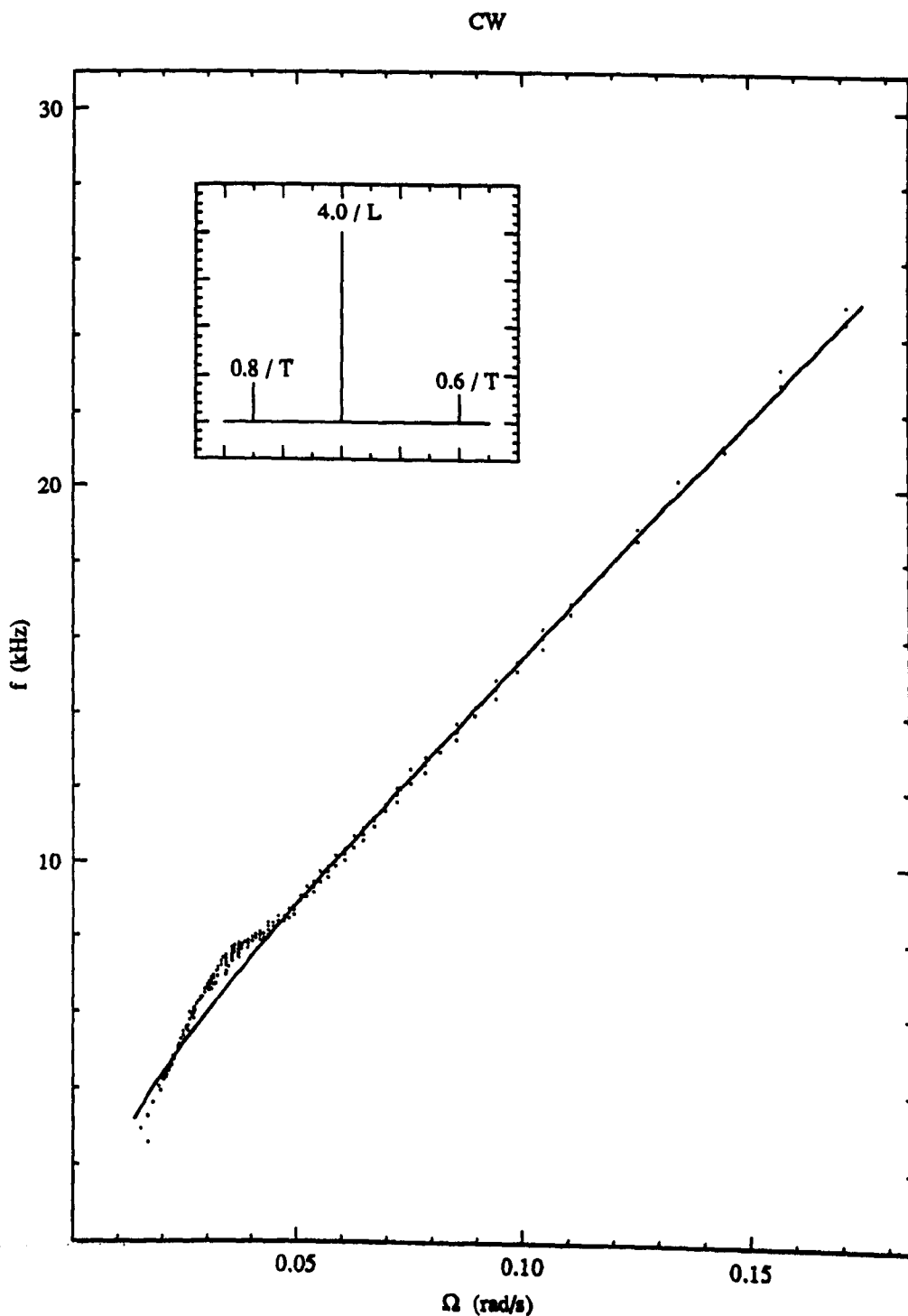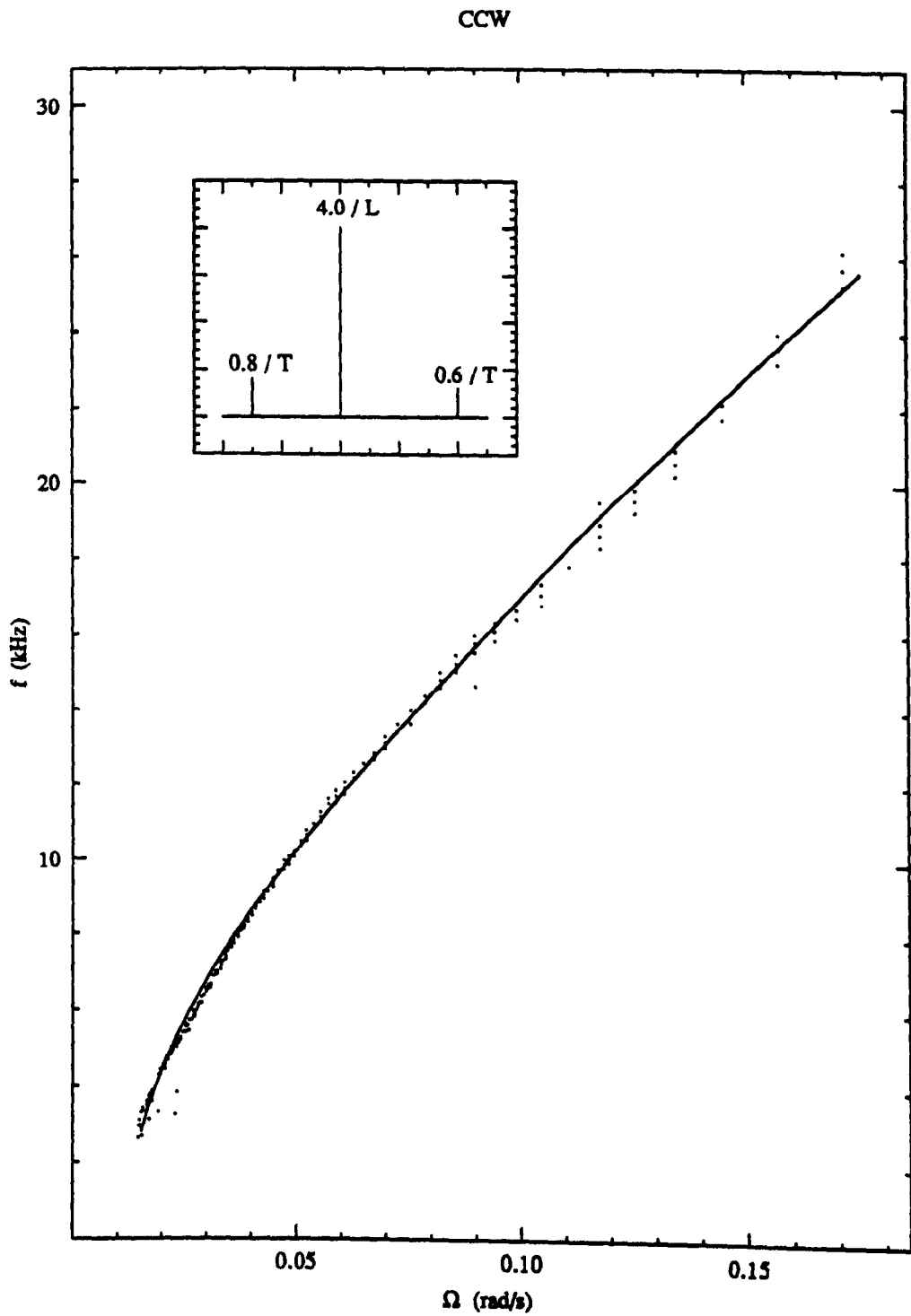
single mode; 6 hr after switch-on, CCW;

$S_0 = (0.101 \pm 0.001) \cdot 10^6$counts/rad, $\Omega_L = 0.116 \pm 0.001$rad/s, $\Omega_N = 0.104 \pm 0.001$rad/s, $\chi^2 = 5 \cdot 10^4$.

4.2.2 Discussion

The most striking feature of some of the data sets is the odd bulge towards the low end which clearly cannot be explained in terms of either the conventional theory or positive scale factor correction (both produce smooth curves). The worst affected are the single mode data sets, while those of two nearly equal modes suffer hardly any distortion at all. It seems clear that the presence of two modes inhibits the effect.

The second observation is that the nearly linear upper regions of the data exhibit a wide variety of slopes, the highest being those of the two-mode sets. In fact, the slope appears to correlate inversely with the size of the bulge, indicating that the two effects are connected.

Appropriately enough, the most noteworthy feature of the numerical fits is the variation in the derived values of the scale factor, the null-shift and the lock-in threshold. These are summarised in the table on p.97, including additional data not shown in the figures.

A brief look at the table above reveals two features:

1. The scale factor is everywhere at variance with the calculated geometrical value of $0.131 \cdot 10^6$ counts/rad; moreover, it is different for each configuration, and can lie either above or below the expected value.

2. The null-shift is everywhere positive, implying a non-reciprocal mechanism.

These, at first sight, lead one to suspect the correctness of the curve fitting procedure, especially when considered in conjunction with the deviant bulge in the majority of the graphs. In particular, one wonders whether the positive-scale-factor-correction function

$$f = S_0 \sqrt{\Omega^2 \left(1 + \frac{A}{\Omega^2 + B}\right)^2 - \Omega_L^2}$$

might not prove a better fit. However, upon trial, one finds that with this function no decent fit at all is possible (see next Sec.4.2.3).

Let us return therefore to the values as given in the table. They unquestionably possess a kind of regularity:

1. The scale factor increases from the single mode case, through the two widely unequal modes, to the two comparable modes;

2. The null-shift and lock-in threshold both decrease;

3. Also the disparity between the CW and CCW data decreases and disappears;

4. Moreover, the bulge in the data flattens out and disappears as well.

Note also the following:

1. The single mode data looks very different 6 hours after switch-on, while the two-mode set remains unchanged. This suggests that the presence of two modes somehow counteracts the time-dependent effects which force down the scale factor and generate the null-shift.

2. The variation within each set is least for the two-mode configuration. This indicates that the two-mode gyroscope is in some sense more stable.

3. Interestingly, the values for the pair of modes in Set 9 are somewhat different from those in Sets 7 & 8. This may be the consequence of their greater frequency separation (~400MHz as opposed to ~300MHz); perhaps indirectly, as their intensities tend to be more unequal and the configuration is less stable.

4. By comparison, the three mode data set is the odd one out, inconsistent with the rest, and also showing the greatest disparity between the CW and the CCW directions and the greatest variation within the set. Furthermore, when observing the gyroscope output on an oscilloscope, it was seen that its amplitude was reduced by a factor of ~2 and that the signal was severely and irregularly distorted.

Data set	Mode configuration	Representative figure	Rotation sense	S_0 (x10^6 counts/rad) ±0.001	Ω_N (rad/s) ±0.001	Ω_L (rad/s) ±0.001
1	single mode 1/2 hr after switch-on	4.2-1	CW	0.120	0.035	0.043
				0.121	0.032	0.041
				0.120	0.036	0.042
				0.119	0.038	0.045
2		4.2-2	CCW	0.113	0.056	0.065
				0.115	0.050	0.062
			.	0.112	0.060	0.067
				0.110	0.064	0.069
3	single mode 6 hr after switch-on	4.2-10	CW	0.124	0.029	0.034
				0.124	0.031	0.033
				0.122	0.033	0.035
				0.123	0.032	0.034
4		4.2-11	CCW	0.101	0.104	0.116
				0.099	0.110	0.119
				0.096	0.114	0.128
				0.098	0.111	0.118
5	two unequal modes	4.2-4	CW	0.124	0.024	0.031
				0.123	0.026	0.032
				0.122	0.027	0.034
6		4.2-5	CCW	0.120	0.030	0.033
				0.119	0.033	0.036
				0.117	0.035	0.038
7	two modes 1/2 hr after switch-on	4.2-3	CW+ CCW	0.134	0.008	0.023
				0.134	0.009	0.023
				0.135	0.008	0.023
				0.135	0.008	0.022
				0.135	0.009	0.022
8	two modes 6 hr after switch-on	4.2-9	CW+ CCW	0.135	0.009	0.022
				0.134	0.009	0.023
				0.134	0.008	0.023
				0.134	0.008	0.022
				0.135	0.009	0.022
9	two (other) modes	4.2-6	CW+ CCW	0.161	0.000	0.012
				0.161	0.001	0.012
				0.160	0.000	0.013
10	three modes	4.2-7	CW	0.080	0.195	0.215
				0.096	0.162	0.187
11		4.2-8	CCW	0.127	0.039	0.052
				0.148	0.014	0.031

.

4.2.3 Alternative fitting schemes

Fig.4.2-12 demonstrates two alternative curve fitting procedures. The data are taken from Fig.4.2-2. The two solid lines are the ideal gyroscope signal $f=S_0\Omega$ and the fit appearing in Fig.4.2-2.

The dashed line is a linear fit to the high Ω ($\Omega>0.07$rad/s) tail of the data. The obtained values of the scale factor and the null-shift are $S_0=0.126\cdot10^6$counts/rad and $\Omega_N=0.025$rad/s. Note that the scale factor is once again well below the expected value and the null-shift is significant.
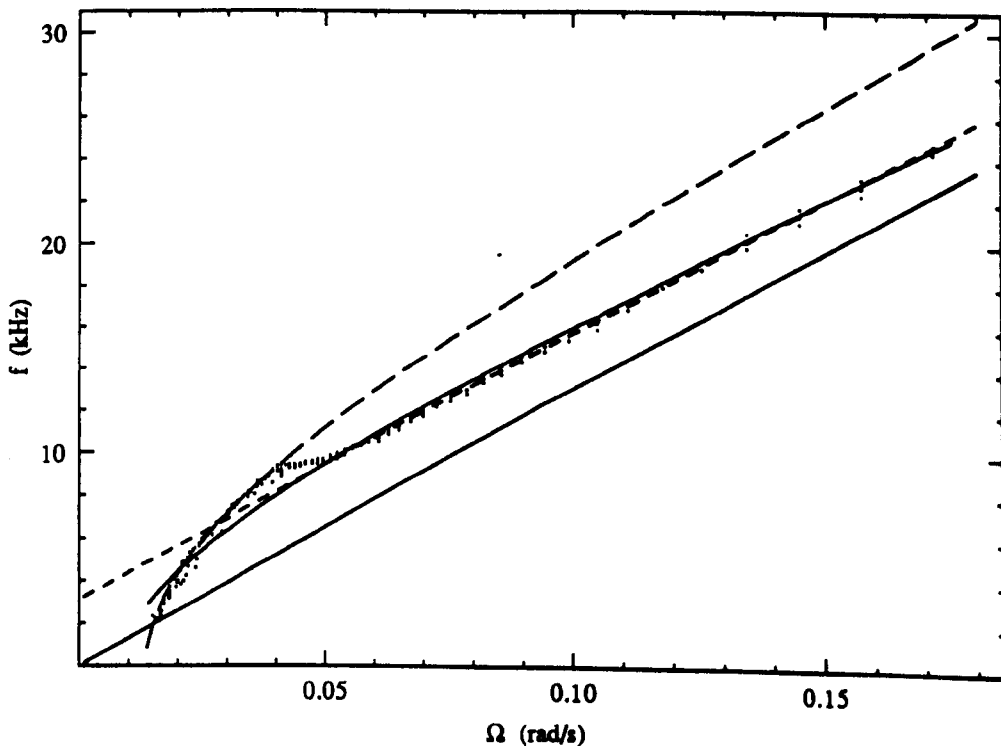

Fig.4.2-12 Alternative fitting schemes (data from Fig.4.2-2):

solid lines: $f = S_0\Omega = 131\ \Omega$ kHz and $f = 113\ [(\Omega+0.056)^2 - 0.065^2]^{1/2}$ kHz;

dashed line: $f = 126\ (\Omega+0.025)$ kHz;

broken line: $f = 131\ [(\Omega+0.068)^2 - 0.0812]^{1/2}$ kHz.

The broken line is a fit to the low end of the data ($\Omega < 0.05$ rad/s). The scale factor here was assumed to have the expected value of $S_0 = 0.131 \cdot 10^6$ counts/rad. The obtained values of the lock-in threshold and the null-shift were $\Omega_L = 0.081$ rad/s and $\Omega_N = 0.068$ rad/s.

The conclusions to be drawn from these fits are twofold. First, the data do not extend to rotation rates high enough to achieve the ideal linear form of the gyroscope signal. Second, whatever phenomenon is causing the exaggerated curvature of the data at low rotation rates, it cannot be extrapolated to higher regions using the conventional formula, and the parameters derived from it are not valid to describe the rest of the data.

Fig.4.2-13 shows the fit to the positive scale factor corrected function

$$f = S_0 \sqrt{ \Omega^2 \left(1 + \frac{A}{\Omega^2 + B} \right)^2 - \Omega_L^2 }$$

This was performed in the following manner. Consider at first only the high tail of the data ($\Omega \gg \Omega_L$): the approximate function is then

$$f \cong S_0 \Omega \left(1 + \frac{A}{\Omega^2 + B} \right)$$

Given a known S_0, A and B can be determined by plotting $(f/S\Omega - 1)^{-1}$ against Ω^2 and fitting to a first-degree polynomial (Fig.4.2-13a). Following that, Ω_L can be determined by calculating the average of

$$\Omega^2 \left(1 + \frac{A}{\Omega^2 + B} \right)^2 - \frac{f^2}{S_0^2}$$

It turns out that for the correct value of S_0 no values of constants A, B and Ω_L can be found which will achieve a good fit between the positive scale factor corrected function and the data (Fig.4.2-13b).

a

b

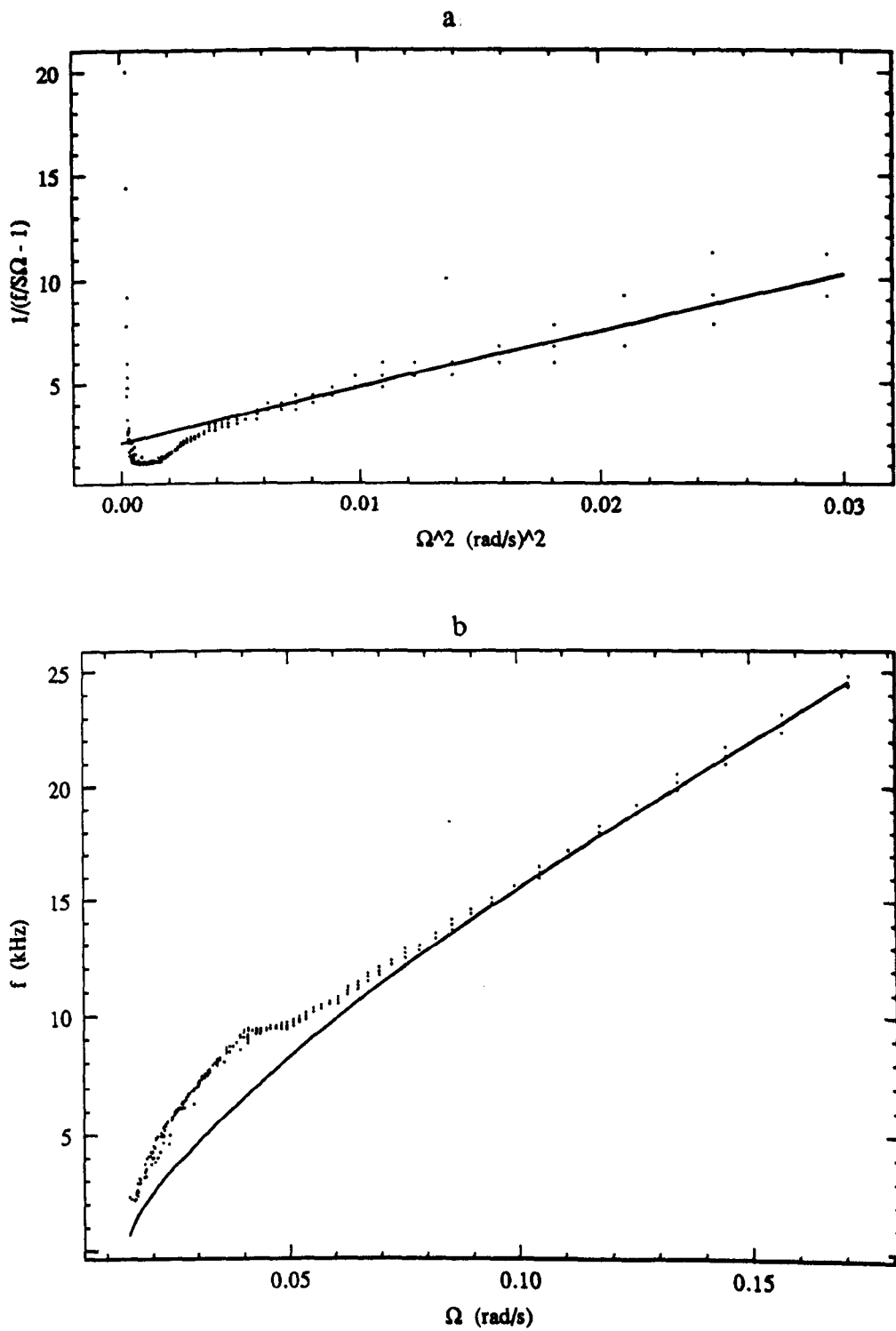Fig.4.2-13 Data in Fig.4.2-2 fitted to the positive-scale-factor corrected function:

a) intermediate step; b) final fit:

$S_0=0.131\cdot 10^6$counts/rad, A=0.004s^{-2}, B=0.009s^{-2}, Ω_L=0.02rad/s.

100

Nevertheless, it is possible to achieve a good fit to the data by carrying out an unconstrained fit, i.e. by treating S_0 as a free parameter (and also optionally making use of null shift): Fig.4.2-14 shows the result. Note three points regarding the fit. First, unlike the standard function, the fit is non-unique: that is to say, widely different sets of parameters result in remarkably similar functions, all fitting the data equally well. Adding null-shift to the equation will give rise to many more possible combinations and an even wider range of parameter values. Second, the scale factor is still far below the expected value: the discrepancy remains. Third, none of the fits quite follow the bulge in the low end of the data, failing to account for this odd feature.

Thus the goodness of the fit reflects the obvious fact that a function possessing an additional rapidly decreasing term governed by two free parameters will fit the data better that a function lacking such term. The use of the positive scale factor corrected function demonstrably fails to provide an explanation for the wrong scale factor or the bulge in the data - as it would had Fig.4.2-13b proved a good fit. Nor is it surprising, since it is not to be expected that such large effects be fully accounted for by means of an intrinsically perturbational theory.
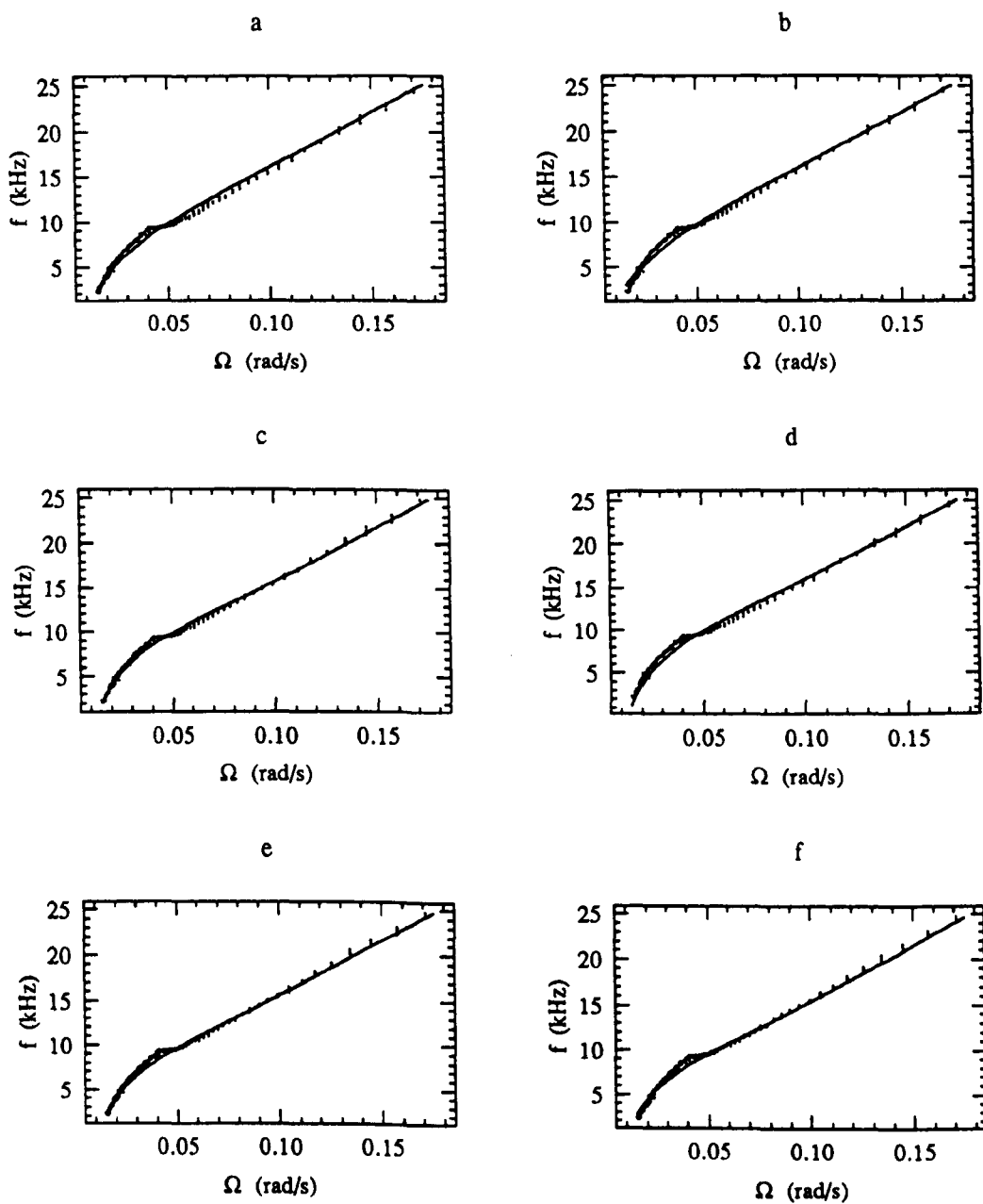
Fig.4.2-14 Data in Fig.4.2-2 fitted to the positive-scale-factor corrected function:

a) S_0=0.110·10^6counts/rad, Ω_L=0.010rad/s A=0.0105s^{-2}, B=0.0120s^{-2}, χ^2=1.0·10^4;

b) S_0=0.110·10^6counts/rad, Ω_L=0.010rad/s A=0.0120s^{-2}, B=0.0150s^{-2}, χ^2=1.1·10^4;

c) S_0=0.115·10^6counts/rad, Ω_L=0.015rad/s A=0.0075s^{-2}, B=0.0080s^{-2}, χ^2=0.8·10^4;

d) S_0=0.115·10^6counts/rad, Ω_L=0.015rad/s A=0.0085s^{-2}, B=0.0100s^{-2}, χ^2=0.9·10^4;

e) S_0=0.120·10^6counts/rad, Ω_L=0.020rad/s A=0.0055s^{-2}, B=0.0060s^{-2}, χ^2=1.1·10^4;

f) S_0=0.120·10^6counts/rad, Ω_L=0.020rad/s A=0.0070s^{-2}, B=0.0090s^{-2}, χ^2=1.2·10^4;

4.2.4 Conclusions

Having considered all these, one can draw several conclusions - with varying degrees of certainty.

1. The scale factor variation must be due to the effects of in-phase scattering[31] and/or extreme grating burning across the mirrors[31].

2. The same, in main, can be said with regard to the null-shift. However, it must also be mentioned here that Anderson *et al.*[3] observed a non-reciprocal null-shift in a two-mode gyroscope (see Fig.2.4-7b). It is possible, therefore, that a similar mechanism offsets the null-shift in the present case.

3. The lock-in threshold appears to decrease in proportion to the intensity ratio of the two modes. Superficially, this agrees with the predictions of the two-mode theory in Ch.2.5. Nonetheless, in view of the extreme distortion of the scale factor and the null-shift, it is impossible to say whether this is a genuine effect, or an artifact of interpretation, or perhaps another result of the same process which gives rise to the other irregularities.

4. The presence of two modes eliminates the positive scale factor correction. It probably achieves this through preventing formation of a standing wave in the resonator, thus precluding the burning of grating across the mirrors.

To conclude: if the experimental data cannot, with any certainty, be said to support the lock-in reduction theory, they do not contradict it either. On the other hand, they do provide a firm evidence that the presence of two modes significantly affects the operation of a ring laser gyroscope.

Chapter 5

CONCLUSIONS

5. CONCLUSION

It has been the aim of this work to investigate the possibility of lock-in reduction in a two-mode ring laser gyroscope.

For this purpose, a new two-mode lock-in theory was developed which extended the single-mode theory to the two-mode case by employing techniques used in the analysis of two coupled lasers. The theory makes no use of small-signal approximation and is valid for all values of intensity ratio. The result was a function having a rapidly oscillating component superimposed on the one-mode form, the amplitude of oscillation being proportional to the intensity ratio of the two modes.

The two-mode equation was found to have no analytic solution; a numerical solution indicated that the time-averaged behaviour of the two-mode function may be similar in all respects to the one-mode case. However, solutions of the two-mode equation were shown to be non-unique: analysis indicates that in certain special circumstances some of them may lead to threshold reduction. If the reduction takes place, it will be in proportion to the intensity ratio of the two modes, possibly eliminating lock-in when the modes are equal. The theory does not provide means for determining whether these special circumstances obtain in practice. All considered, therefore, no conclusion can be drawn from this version of two-mode theory as to the efficacy of two-mode operation in reducing the lock-in threshold.

A ring laser gyroscope testing set-up was developed in order to verify the conjecture experimentally. The set-up consisted of a rate table, a digital circuit linked to a computer to record gyroscope signal versus rotation rate, and a Fabry-Perot spectrum analyser coupled with a piezoelectric mirror to control

and monitor the mode structure. Unfortunately, the motion of the rate table at low speed was uneven, while the limited digitisation resolution caused large errors at high speed. These factors together set the boundaries of the useful experimental range of rotation rates.

Two ring laser gyroscopes were used. First, a modular ring laser was built. Running single-mode, it performed as expected theoretically, yielding the correct scale factor and the expected order of magnitude of the lock-in threshold. However, the discharge tube had been filled with the natural mixture He:Ne^{20}/Ne^{22} instead of the proper gyroscope half-and-half mix. This, together with the inherent mechanical instability of a modular laser, prevented it running on two modes.

The second gyroscope was a BAe solid-block model. It possessed stable modes easily adjustable with a piezo-mirror. However, the control over the mode structure was poor, precluding the possibility of obtaining two equal modes without having a third one appear as well. Unhappily, it also had presumably defective mirrors which gave rise to extreme Hermitian scattering and grating burning.

The results were thus equivocal. The presence of a second mode clearly influenced the operation of the ring laser, the effect being most noticeable for modes of similar intensities. However, the general behaviour of the system was so irregular, so many parameters appeared to be affected, that it was impossible to tell whether the difference was due to reduction in lock-in threshold or to some other processes. Furthermore, the perturbative theory of positive scale factor correction failed to achieve a good fit to the data for realistic values of scale factor and null-shift, thus showing itself unsuitable for treating such severe effects. The most important deviations from the expected behaviour - the scale factor errors - were the apparently incorrect scale factor and the large

non-reciprocal null-shift; another was the odd bulge of positive scale factor correction at low rotation rates. All these errors were greatly reduced in the presence of two modes. On balance, one may conclude that although the data cannot be said to demonstrate threshold reduction, it does not exclude it either, indeed there are hints that it may be taking place.

The three-mode operation showed no clear trend; no attempt was made to provide a theoretical description of it.

Altogether the most salient experimental result was that the presence of two modes greatly reduces, or perhaps in some circumstances even eliminates, the effects which give rise to various forms of positive scale factor correction. One possible explanation may be that the rapid oscillation prevents or counteracts the formation of a grating across the mirrors.

In conclusion, both the theory developed in Ch.2.5 and the experiments described in Ch.4.2 hint at the possibility of lock-in reduction by means of two-mode operation. Since the system has the advantages of having a simple resonator and lacking moving parts, it may well deserve further investigation.

Further work

With regard to theory, it would be of great interest to try to obtain a time-averaged numerical solution of the lock-in equation and to investigate its dependence on the various parameters of the system. In addition, an attempt may be made to extend the theory to three modes.

As far as experimental work is concerned, for a thorough investigation of all aspects of two-mode gyroscope operation a semi-modular ring laser appears to be necessary. This would on the one hand possess a rigid structure not susceptible to vibration; while on the other having adjustable mirrors, and perhaps apertures as well, to allow full mode selection and control. Needless to

say, the experiments would require a commercial rate table.

Among questions to be answered are: What is the difference, if any, between the effect of a longitudinal-longitudinal pair and a longitudinal-transverse pair? Does a TEM_{m00}-TEM_{m10} pair behave differently from a TEM_{m00}-$TEM_{(m+1)10}$ pair? What is the margin of error on the two-mode intensity ratio which yet preserves acceptably low threshold? How can a given mode configuration be stabilised without the recourse to a continuous spectrum analyser monitoring?

APPENDIX

1. Proof of Eq.2.5.3-2

Let $\psi(t)$ be differentiable everywhere.

Define $F(t) = \psi(t+T) - \psi(t)$: $F(t)$ is differentiable

Then $\dot{F}(t) = \dot{\psi}(t+T) - \dot{\psi}(t)$

If $\dot{\psi}(t+T) = \dot{\psi}(t)$

then $\dot{F}(t) = 0 \quad => \quad F(t) = \text{constant} = A$

Then $\psi(t) = \psi(t+T) - A$

2. Proof of Eq.2.5.3-4

Assume $\psi(t+T) = \psi(t) + A$

then $\psi(t+NT) - \psi(t) = NA$

Let

$$\Psi(t) = \frac{1}{NT} \int_{t}^{t+NT} \psi(u)\, du$$

for any integer N

Then

$$\dot{\Psi}(t) = \frac{\Psi(t+h) - \Psi(t)}{h} = \frac{1}{hNT}\left[\int_{t+h}^{t+h+NT}\psi(u)\, du - \int_{t}^{t+NT}\psi(u)\, du\right]$$

$$= \frac{1}{hNT}\left[-\int_{t}^{t+h}\psi(u)\, du + \int_{t+NT}^{t+h+NT}\psi(u)\, du\right]$$

Let $v = u - NT$

then

$$\dot{\Psi}(t) = \frac{1}{hNT} \left[-\int_t^{t+h} \psi(u)\, du + \int_t^{t+h} \psi(v+NT)\, dv \right]$$

$$= \frac{1}{hNT} \left[\int_t^{t+h} \left(\psi(u+NT) - \psi(u) \right) du \right]$$

$$= \frac{1}{hNT} \left[\int_t^{t+h} NA\, du \right]$$

$$= \frac{1}{hT} \left[Au \right]_t^{t+h} = \frac{Ah}{hT} = \frac{A}{T}$$

Thus

$$\dot{\Psi}(t) = \frac{A}{T}$$

$$\Rightarrow \qquad \Psi(t) = \text{constant} + \frac{A}{T}$$

3. Time average over a period of arbitrary length T*

Assume $\psi(t+T) = \psi(t) + A$

Then   (letting $v = u - T$)

$$\Psi(t+T) = \frac{1}{T^*} \int_{t+T}^{t+T+T^*} \psi(u)\, du = \frac{1}{T^*} \int_t^{t+T^*} \psi(v+T)\, dv$$

$$= \frac{1}{T^*} \int_t^{t+T^*} \left(\psi(v) + A \right) dv = \frac{1}{T^*} \int_t^{t+T^*} \psi(v)\, dv + A$$

$$= \Psi(t) + A$$

Also $\dot{\Psi}(t+T) = \dot{\Psi}(t)$

$$\Rightarrow \qquad \dot{\Psi}(t) \text{ is periodic with period } T$$

4. Non-uniqueness

It is possible that for a given m two solutions having different n's may pass through the same point.

For example, consider solutions $\psi_1(t)$ and $\psi_2(t)$.

Let
$$\psi_1(t) = \psi_1(t+2m\pi/\Delta v_2) - 2n_1\pi$$

and
$$\psi_2(t) = \psi_2(t+2m\pi/\Delta v_2) - 2n_2\pi$$

where
$$n_1 \neq n_2$$

Let both $\psi_1(t)$ and $\psi_2(t)$ have initial condition $\psi_1(0) = \psi_2(0) = \psi_0$.

Then
$$\psi_1(0) = \psi_0 = \psi_1(2m\pi/\Delta v_2) - 2n_1\pi$$

and
$$\psi_2(0) = \psi_0 = \psi_2(2m\pi/\Delta v_2) - 2n_2\pi$$

Subtracting gives
$$\psi_1(2m\pi/\Delta v_2) - \psi_1(2m\pi/\Delta v_2) = 2\pi(n_1 - n_2) \neq 0$$

Hence $\psi_1(t)$ and $\psi_2(t)$ both pass through $(0,\psi_0)$ but differ at $t=2m\pi/\Delta v_2$: they are therefore distinct functions.

Consequently a solution with given initial condition is not unique.

5. Numerical solution

The numerical solutions shown in Fig.A-1 were obtained using the Runge-Kutta method. Apart from the superimposed rapid fluctuation, all solutions calculated in this way are identical to the analytical ones for the one-mode case. However, due to the fluctuation, they remain periodic for all values of K.
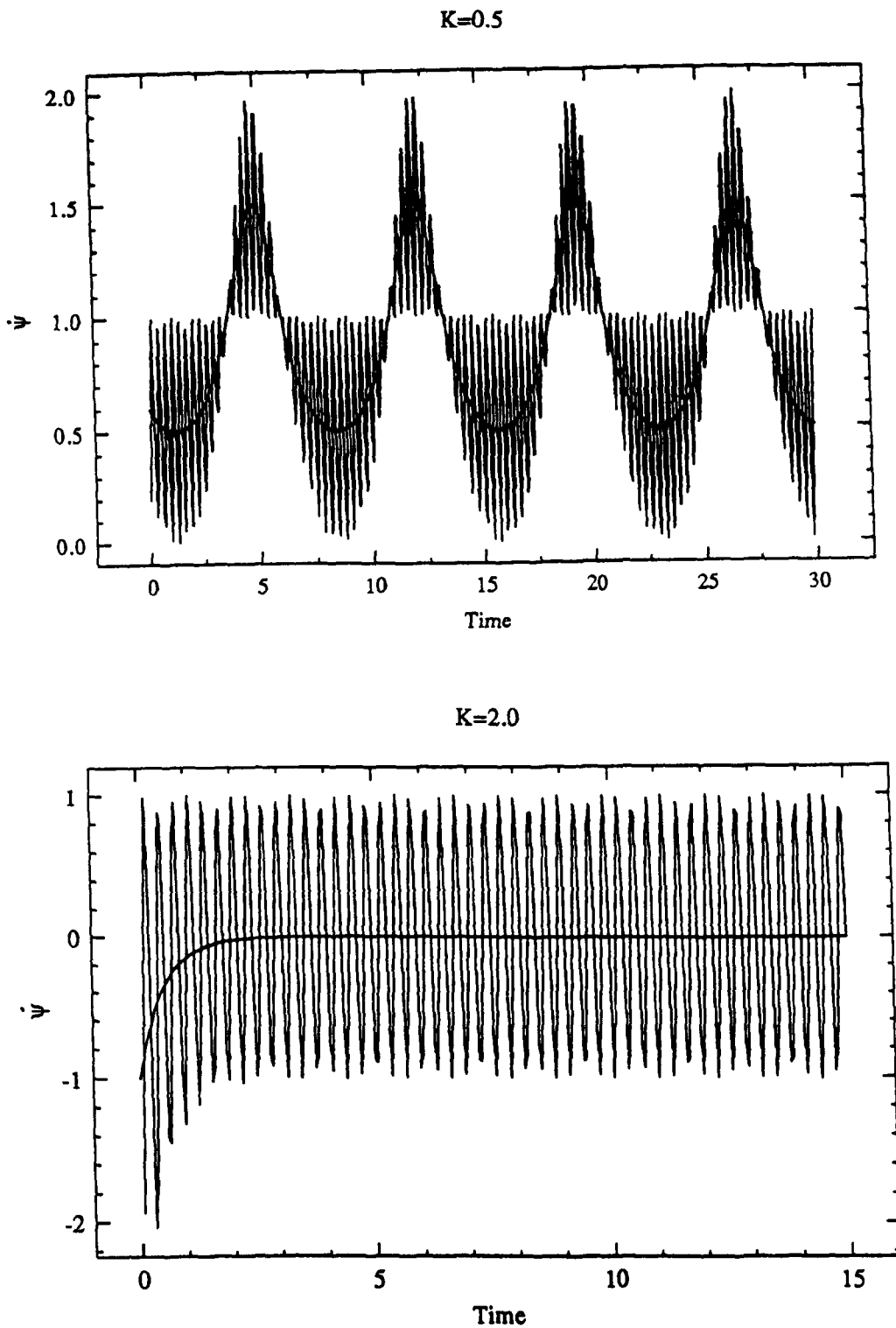
K=0.5

K=2.0

Fig.A-1 Numerical solutions of the two-mode lock-in equation:

$\Delta v_2 = 20$ (for better clarity in printing), $\rho = 0.1$;

the smooth line denotes the one-mode solution.

REFERENCES

1. M. Abramowitz and I.A. Stegun, eds., *Handbook of Mathematical Functions*, Dover Publications, New York, 1985

2. D.A. Anderson, W.W. Chow, V.E. Sanders and M.O. Scully, "Novel multioscillator approach to the problem of locking in two-mode ring-laser gyros", *Appl. Opt.*, **18**, 941 (1979)

3. D.A. Anderson, W.W. Chow, M.O. Scully and V.E. Sanders, "Optically biased laser gyro", *Opt. Lett.*, **5**, 413 (1980)

4. F. Aronowitz, "The Laser Gyro", in *Laser Applications*, M. Ross, ed., Academic Press, New York, 1971

5. F. Aronowitz and W.L. Lim, "Positive scale factor correction in the laser gyro", *IEEE J. Quantum Electron.*, **QE-13**, 338 (1977)

6. F. Aronowitz and W.L. Lim, "Dispersion and gas flow effects in the ring laser gyro", *SPIE*, **157**, 7 (1978)

7. W.R. Bennet, Jr., *The Physics of Gas Lasers*, Gordon &Breach, New York, 1977

8. L. Casperson and A. Yariv, "Longitudinal modes in a high-gain laser", *Appl. Phys. Lett.*, **17**, 259 (1970)

9. W.W. Chow, J. Gea-Bancloche and L.M. Pedrotti, "The ring laser gyro", *Rev. Mod. Phys.*, **57**, 61 (1985)

10. W.W. Chow, "A composite-resonator mode description of coupled lasers", *IEEE J. Quantum Electron.*, **QE-22**, 1174 (1986)

11. D.H. Close, "Strong-field saturation effects in laser media", *Phys. Rev.*, **153**, 360 (1967)

12. S.A. Collins, Jr., "Analysis of optical resonators involving focusing elements", *Appl. Opt.*, **3**, 1263 (1964)

13. Z.-H. Fang and H. Thienpont, "An alignment technique for a ring laser cavity", *Opt. and Laser Technol.*, p.269, Oct. 1984

14. H.A. Haus, H. Statz and I.W. Smith, "Frequency locking of modes in a ring laser", *IEEE J. Quantum Electron.*, **QE-21**, 78 (1985)

15. M. Hercher, "The spherical mirror Fabry-Perot interferometer", *Appl. Opt.*, **7**, 951 (1968)

16. S.F. Jacobs and R. Zanoni, "Laser ring gyro of arbitrary shape and rotation axis", *Am. J. Phys.*, **50**, 659 (1982)

17. C. Knipe, D.A. Andrews and T.A. King, "Mode interactions in four-frequency degeneracy-lifted ring lasers", *J. Mod. Opt.*, **35**, 441 (1988)

18. L.N. Menegozzi and W.E. Lamb, Jr., "Theory of a ring laser", *Phys. Rev. A* , **8**, 2103 (1973)

19. T.J. Podgorski and F. Aronowitz, "Langmuir flow effects in the laser gyro", *IEEE J. Quantum Electron.*, QE-4, 11 (1968)

20. E.J. Post, "Sagnac effect", *Rev. Mod. Phys.*, **39**, 475 (1967)

21. V.E. Sanders, D.A. Anderson and M.O. Scully, "A four-mode solution to the locking problem in two-mode ring laser gyros", *SPIE* , **157**, 30 (1978)

22. M. Sargent III, M.O. Scully and W.E, Lamb, Jr., *Laser Physics*, Addison-Wesley, Reading, Mass., 1974

23. M.O. Scully, V.E. Sanders and M. Sargent III, "Novel multioscillator approach to the problem of locking in two-mode ring-laser gyros", *Opt. Lett.*, 3, 43 (1978)

24. I.W. Smith and T.A. Dorschner, US patent application No.4 548 501, 7 Jan. 1986

25. P.W. Smith, "Linewidth and saturation parameters for the 6328-Å transition in a He-Ne laser", *J. Appl. Phys.*, **37**, 2089 (1966)

26. P.W. Smith, "On the optimum geometry of a 6328Å laser oscillator", *IEEE J. Quantum Electron.*, QE-2, 77 (1966)

27. M.B. Spencer and W.E. Lamb, Jr., "Theory of two coupled lasers", *Phys. Rev. A* , **5**, 893 (1972)

28. H. Statz, T.A. Dorschner, M. Holtz and I.W. Smith, "The multioscillator ring laser gyroscope" in *Laser Handbook*, M.L. Stitch and M. Bass, eds., Elsevier Science, 1985

29. J. Thewlis, ed., *Encyclopaedic Dictionary of Physics*, Pergamon Press, 1961, pp. 437-438

30. N.L. Thomas, "Low-scatter, low-loss mirrors for laser gyros", *SPIE*, **157**, 41 (1978)

31. J.R. Wilkinson, "Ring lasers", *Prog. Quant. Electr.*, **11**, 1 (1987)

32. A. Yariv, *Quantum Electronics*, 3rd ed., Wiley, 1989